Sorption-based Thermal Energy Storage:

Material Development and Effects of Operating Conditions

By: Curtis Strong

Thesis submitted to the Department of Chemical and Biological Engineering in partial fulfillment of the requirements for the degree of M.A.Sc. in Chemical Engineering

Department of Chemical and Biological Engineering

University of Ottawa

April 2021

Abstract

The adverse effects of climate change, the steady depletion of fossil fuels, and the industrialization of developing countries have resulted in an increased supply and demand of renewable thermal energy. Renewable thermal energy sources like solar thermal energy produce fewer local emissions but have a temporally inconsistent power output. The consumer space heating and domestic hot water demands also vary as a function of time. This creates a mismatch between thermal energy supply and demand. Energy storage is one method of solving this problem. However, conventional methods, like hot water storage, are voluminous and can only store heat for short periods of time. Therefore, compact long-term energy storage technologies, like sorption-based energy storage systems, require research and development. The current work aims to identify and develop suitable materials for sorption-based energy storage systems and to determine the effects of operating conditions on the performance of thermal energy storage systems.

A material screening study was performed, which identified MCM-41, SAPO-34, and silica gel, which are all silica-based materials, as suitable materials for sorption-based energy storage. The effects of key operating variables for a silica gel/water-vapour adsorption-based energy storage system were quantified and optimized. The optimized system energy storage density value was nearly double that of unoptimized systems. The effects of salt impregnation were investigated by impregnating different hosts with $MgSO_4$ salt and varying the concentration of the salt in the host material. All composites were stable after three hydration/dehydration cycle. A silica gel/$MgSO_4$ hybrid containing 33 wt% $MgSO_4$ was found to have the highest energy storage density of all of the $MgSO_4$-based composites. Finally, $CaCl_2$, a promising hygroscopic for thermal energy storage was stabilized via impregnation into silica gel and encapsulation in methylcellulose. A novel synthesis technique involving the simultaneous impregnation of silica gel with $CaCl_2$ and encapsulation in methylcellulose produced a stable encapsulated salt-in-matrix composite with a high energy storage performance.

Sommaire

Les effets négatifs du changement climatique, l'épuisement des combustibles fossiles et l'industrialisation des pays en développement ont créé une plus grande offre et demande d'énergie thermique renouvelable. Les sources d'énergie thermique renouvelable comme l'énergie solaire thermique produisent moins d'émissions locales, mais ont une production d'énergie irrégulière par rapport au temps. Les demandes de chauffage varient également en fonction du temps. Cela crée une discrétion entre l'offre et la demande d'énergie thermique renouvelable. Le stockage de l'énergie est une méthode qui peut résoudre ce problème. Malheureusement, les méthodes conventionnelles sont volumineuses et ne peuvent stocker l'énergie thermique que pendant de courtes périodes. Alors, les technologies de stockage d'énergie compactes et long terme, comme les systèmes de stockage d'énergie par sorption, nécessitent de recherche et de développement. Cette thèse vise à identifier et à développer des matériaux appropriés pour les systèmes de stockage d'énergie par sorption et à optimiser les effets des conditions de fonctionnement.

La première étude de cette thèse a identifié le MCM-41, le SAPO-34 et le gel de silice comme des matériaux appropriés pour le stockage de l'énergie par sorption. Les effets des conditions de fonctionnement d'un système de stockage d'énergie ont été quantifiés et optimisés. La valeur de la densité de stockage d'énergie du système optimisé était presque le double des systèmes non optimisés. Les effets de l'imprégnation du $MgSO_4$ ont été étudiés en imprégnant différentes matrices avec du $MgSO_4$. De plus, la concentration du sel dans la matrice a été variée. Toutes les composites étaient stables après trois cycles d'hydratation/déshydratation. Un hybride gel de silice/$MgSO_4$ contenant 33 % en poids de $MgSO_4$ avait la densité de stockage d'énergie le plus haut. Enfin, le $CaCl_2$, un bon matériel de stockage de l'énergie thermique, a été stabilisé par imprégnation dans du gel de silice et encapsulation dans de la méthylcellulose. Une nouvelle technique de synthèse où on fait l'imprégnation simultanée de gel de silice avec du $CaCl_2$ et l'encapsulation dans de la methylcellulose a été développé. La produit de cette synthèse était une composite stable avec une haute performance.

Statement of Contribution of Collaborators

I hereby certify that I am the author of this thesis. The experimental work, the data analysis and the writing of articles was completed under the supervision of Dr. F. Handan Tezel at the University of Ottawa.

Chapter 2 was completed and written entirely by me, with editorial comments from Dr. F. Handan Tezel and Dr. Ye Carrier. Dr. Ye Carrier also performed a small portion of the energy storage experiments.

Chapter 3 was completed and written entirely by me, with editorial comments from Dr. F. Handan Tezel and Dr. Ye Carrier. Chapter 3 was prepared for submission as an article to the Applied Energy Journal.

Chapter 4 was completed in collaboration with Dr. Suboohi Shervani, a post-doctoral researcher in Dr. F Handan Tezel's research group. I performed the energy storage experiments and analysis while Dr. Shervani synthesized and characterized the materials. She is the lead author on this chapter, but I wrote the energy storage results and methodology sections and provided significant revisions and feedback for the other sections of the chapter.

Chapter 5 was completed in collaboration with Dr. Shervani. I performed the energy storage experiments and analysis while Dr. Shervani synthesized and characterized the materials. I am the lead author for this chapter but Dr. Shervani wrote the material preparation section and a portion of the conclusions. Both Dr. Shervani and Dr. Tezel provided editorial comments on the rest of the manuscript.

Appendix A is an article submitted to the Adsorption Journal. The first author of this work is Dr. Ye Carrier, who completed the manuscript. My contributions to this work included performing experiments, data analysis, equipment and methodology modifications, and providing comments and revisions for the manuscript. I am second author for this paper and therefore it is provided in Appendix A.

Acknowledgements

I would like to thank my supervisor Dr. F. Handan Tezel for her guidance, support and assistance throughout my graduate studies.

I would like to thank Dr. Ye Carrier for her help training me as well as for her contributions to the project and thermal energy storage system design and construction.

I would like to thank Dr. Suboohi Shervani for her material science expertise and contributions to the project.

I would like to thank Dominique Lefevre for continuing our group's energy storage experiments during my tenure in Austria and for her contributions to the article in Appendix A.

I would like to thank the rest of Dr. F. Handan Tezel's research group for their help, support and advise. I would also like to thank them for being accommodating and flexible with lab-time scheduling during the COVID-19 pandemic-related lockdown.

I would like to thank the shop staff of the Chemical and Biological Engineering Department at the University of Ottawa, Franco Ziroldo, Gérard Nina, and James McDermid for their help in building and maintaining my laboratory systems.

I would like to thank Fahad Chowdhury and Najmeh Ahledel for providing advice and equipment regarding the drop testing and pelletization, respectively.

I would like to thank my colleagues at AEE INTEC for the opportunity to collaborate with them and learn from their expertise.

I would like to thank the NSERC Energy Storage Network members and the Natural Resources Canada thermochemical energy storage team for their input on the project.

I would like to thank the NSERC Energy Storage Network, Natural Resources Canada, and the University of Ottawa for the funding they provided which allowed me to conduct this research work.

I would like to thank my friends and family for their support and encouragement.

Finally, I would like to thank my colleagues and my acquaintances for all of the conversations I have had with them over the past couple of years that have directly and indirectly led to research ideas and solutions.

Table of Contents

List of Figures

List of Tables

Chapter 1 – Introduction

1.1 Abbreviations

EDX	Energy dispersive x-ray
MCM	Mobil composition of matter
SAPO	Silico-alumino-phosphate
SEM	Scanning electron microscopy
TCES	Thermochemical energy storage
TES	Thermal energy storage

1.2 General Background

Thermal energy makes up roughly 83% of the consumer energy demand in Canada [1]. Simultaneously, renewable energy is in increasing global supply and demand, including renewable thermal energy, like solar thermal power [2]. Although renewable energy sources offer numerous advantages like reduction in carbon emissions and fossil fuel independence, many renewables exhibit an inconsistent energy output. This means that some renewable power supply can vary hourly, daily, or seasonally. Unfortunately, these fluctuations in power output do not match up temporally with the variations in consumer demand. This creates a mismatch between supply and demand and results in energy companies oversizing equipment, wasting heat, and using fossil fuels to supply heat during times of peak demand. One way to resolve this mismatch would be to store excess energy during times of high renewable power output and to release this energy in times of high consumer demand.

Electrical energy is often stored using technology like lithium-ion batteries, but since the conversion of thermal energy to electrical energy is inefficient, thermal energy is not typically stored using these technologies. The conventional methods of thermal energy storage (TES) involve heating up some medium (e.g. rock, water, etc.) and storing the energy as sensible heat. This method is simple but requires large volume to store useful amounts of energy and experiences significant heat losses over time during storage. Latent heat energy storage has also been implemented commercially [3]. It typically involves freezing and melting molten salts and experiences less heat losses and greater energy density than sensible heat storage methods [4]. However, latent heat still experiences heat losses over time and many

proposed materials are toxic. A promising alternative to these two methods is thermochemical energy storage (TCES).

1.3 Thermochemical Energy Storage

Energy can be stored as thermochemical heat. TCES involves a chemical or physical process like water vapour adsorption/desorption or salt hydration/dehydration. For the example of water vapour adsorption, heat is stored by applying heat to an adsorbent and causing the water-vapour to desorb from the surface of the adsorbent. The stored thermal energy can then be released by allowing water vapour to adsorb onto the surface of the adsorbent. TCES exhibits high energy storage densities and it can also theoretically store thermal energy indefinitely, making it suitable for both short-term and long-term storage applications. Furthermore, many of the proposed materials for this process are non-toxic [5].

Despite its advantages, TCES technology is still underdeveloped. One main bottleneck for its development is lack of suitable materials. Materials for TCES applications should have high water-vapour adsorption capacity, have high heat of adsorption/hydration heat, have good cyclic stability, be easy to regenerate, be non-toxic, be non-corrosive, be inexpensive, be pelletized or granular, and be commercially available. A second obstacle inhibiting development of this technology is lack of information about the effects of energy storage system operating variables for different materials at different scales. It is known that variables like regeneration temperature, adsorption humidity, and flow rate have an impact on the energy storage performance of TCES systems, but the data currently reported in literature is insufficient.

1.4 Thesis Objectives

The goal of this thesis is to contribute to the overall knowledge and understanding of the TCES performance of various materials and the effects of operating conditions of TCES systems. In order to achieve this goal, the current work has set the following objectives:

- Perform an adsorbent material screening study by pelletizing various materials and testing their durability and energy storage performances.
- Optimize a water-vapour/silica gel-based lab-scale energy storage system by quantifying the effects of regeneration temperature, adsorption inlet humidity, flow rate, particle size, and thermal insulation.
- Synthesize and test new $MgSO_4$-based composite materials and then quantify the effects of $MgSO_4$ concentration on energy storage performance for $MgSO_4$ composites.
- Stabilize $CaCl_2$ and silica gel/$CaCl_2$ composites by encapsulation with methylcellulose and examine the stability and energy storage performance of the resulting composites.
- Examine and quantify the effects of operating conditions when using SAPO-34 as the active adsorbent for a lab-scale thermal energy storage system.

1.5 Thesis Structure

Chapter 2 of this thesis is a screening study where 5 adsorbents are investigated. Titanium silicate molecular sieve, flax shive briquettes, MCM-41, SAPO-34, and silica gel are pelletized, and then their mechanical durability and energy storage performance are assessed and compared. The mechanical durability was assessed via a standard drop test and the energy storage performance was assessed using a lab-scale energy storage apparatus.

Chapter 3 of this work is an article entitled “Optimization of operating conditions for an open bulk-scale silica gel/water vapour adsorption energy storage system” which was submitted to the Applied Energy Journal in February 2021. This article investigates the effects of key operating parameters (regeneration temperature, adsorption inlet humidity, flow rate, particle size, and thermal insulation) on the performance of a lab-scale silica gel/water adsorption energy storage system. After quantifying the effects of these operating conditions, the system variables were optimized to maximize the energy storage performance.

Chapter 4 involves the synthesis of four salt-in-matrix composites using $MgSO_4$ as the impregnate. The best performing material, silica gel impregnated with $MgSO_4$, was synthesized with various different concentrations of $MgSO_4$. The $MgSO_4$/SG composites were characterized via SEM and EDX, and their energy storage performance was analyzed using a lab-scale energy storage apparatus. The effects of salt quantity were investigated, and the amount of salt added to the silica gel matrix was optimized.

Chapter 5 presents the synthesis and energy storage performance of three $CaCl_2$-based composite materials: silica gel impregnated with $CaCl_2$, $CaCl_2$ encapsulated by methylcellulose, and $CaCl_2$-impregnated silica gel that has also been encapsulated with methylcellulose. The material energy storage performance and cyclic stability was tested using a lab-scale energy storage apparatus.

Chapter 6 provides a summary of the key findings and conclusions from the other chapters. It also provides recommendations for future studies.

Appendix A contains an article titled “Study of energy density of adsorption-based thermal energy storage system under different operating conditions for SAPO-34” which was submitted to Adsorption in December 2020. In this work a pelletized SAPO-34 sample is tested at the lab scale using a variety of different operating conditions to determine its energy storage performance under various conditions.

1.6 References

[1] Natural Resources Canada, “Energy Efficiency Trends in Canada 1990 to 2013,” 2019. ISSN: 1926-8254

[2] IEA, “Renewables 2019,” 2019.

[3] H. Sanderson, “Battery life: the race to find a storage solution for a green energy future,” *Financial Times*, 2020. [Online]. Available: https://www.ft.com/content/7c07e492-41eb-4488-bc34-77b9d806ed5c.

[4] D. Lefebvre and F. H. Tezel, “A review of energy storage technologies with a focus on adsorption thermal energy storage processes for heating applications,” *Renew. Sustain. Energy Rev.*, vol. 67, pp. 116–125, 2017.

[5] L. Scapino, H. A. Zondag, J. Van Bael, J. Diriken, and C. C. M. Rindt, “Sorption heat storage for long-term low-temperature applications: A review on the advancements at material and prototype scale,” *Appl. Energy*, vol. 190, pp. 920–948, 2017.

Chapter 2 – Adsorbent pelletization and screening for water-vapour adsorption-based thermal energy storage

Curtis Strong, University of Ottawa

Ye Carrier, University of Ottawa

F. Handan Tezel, University of Ottawa

Abstract

Thermochemical energy storage is a promising alternative to conventional thermal energy storage methods; however, new materials need to be developed, pelletized and tested. The current study investigates the use of various adsorbents for water-vapour adsorption-based thermochemical energy storage. The tested adsorbents included a titanium silicate molecular sieve (Ti-Si), flax shive briquettes, MCM-41, SAPO-34, and silica gel. The energy storage density and thermal power of each material was determined by testing them in a lab-scale adsorption thermal energy storage system. All materials were either received as pellets or they were pelletized to minimize the system pressure drop and improve ease of handling. The performance of each adsorbent was evaluated under different regeneration temperatures and relative humidity levels in the feed stream. The mechanical durability of the materials was analysed using a standard drop test. The hydrothermal stability was assessed by performing multiple adsorption and desorption cycles on the same material under the same conditions and observing any changes in behaviour or performance. Silica gel, SAPO-34, and MCM-41 showed energy densities above 150 kWh/m^3 and less than a 5% decrease in energy storage density after 20 adsorption and desorption cycles. All materials except for the flax shive briquettes retained more than 85% of their initial mass after the standard drop test.

Keywords: Adsorption, thermal energy storage, energy density, water vapour adsorption, materials, pelletization

2.1 Nomenclature

$C_{p,air}$	Specific heat capacity of air (kWh/g·°C)
ESD	Energy storage density (kWh/m^3)
$\dot{m}_{air}$	Mass flow rate of air (g/s)
m_{final}	Mass after dropping the particle (g)
$m_{initial}$	Mass before dropping the particle (g)
p/p_0	Relative pressure; partial pressure divided by the saturation pressure (/)
$Q_{adsorption}$	Energy released during adsorption (kWh)
q	Mass of adsorbate adsorbed (g/g)
$q_{adsorption}$	Mass of adsorbate adsorbed at saturation at the end of the adsorption (kg)
$q_{desorption}$	Mass of adsorbate adsorbed after fully regenerating (kg)
RH	Relative humidity (%)
t	Duration of the adsorption experiment (s)
T_{in}	Temperature at the inlet of the column (°C)
T_{out}	Temperature at the outlet of the column (°C)
V	Volume of the adsorption column (m^3)
$\%\ mass\ retained$	Percentage of the initial mass retained after dropping the particle (%)

Greek Letters

$\Delta H_{ads}(q)$	Heat of adsorption as a function of amount adsorbed (kWh/kg)
ΔT	Difference between the inlet and outlet of the column (°C)

2.2 Abbreviations

BET	Brunauer–Emmett–Teller
ESD	Energy storage density
MCM	Mobil Composition of Matter

MFC	Mass flow controller
PEG	Poly(ethylene glycol)
PVA	Poly(vinyl alcohol)
RH	Relative humidity
SAPO	Silico-alumino-phosphate
SLPM	Standard litres per minute
TCES	Thermochemical energy storage
TES	Thermal energy storage
Ti-Si	Titanium silicate molecular sieve

2.3 Introduction

2.3.1 Motivation

In Canada, thermal energy accounts for more than 60% of commercial and institutional end-use energy and more than 80% of residential end-use energy [1]. Renewable thermal and electrical energy sources are increasing simultaneously, in both supply and demand, consistently and significantly increasing their market share in developed countries [2].

Renewable energy sources offer numerous advantages like reduced local emissions and greater sustainability, but the energy output of renewable energy sources is temporally inconsistent. For example, solar panels have a greater energy output during summer months than in winter months in the northern hemisphere, due to elevated solar irradiation levels in the summer months. This issue is exacerbated by the fact that the energy demand is also inconsistent. For example, in Canada, there is a greater demand for space heating in the winter months than in the summer months. One way to resolve this mismatch would be to store excess energy produced by renewable energy sources and then release it when it is needed.

Thermal energy can either be converted to another type of energy like electricity and be stored or be stored directly as thermal energy. Since converting heat to electricity is costly and inefficient, thermal energy storage (TES) techniques are of interest. Conventional TES techniques involve storing energy as sensible heat using a hot water tank or some other medium that can be heated and have its temperature

maintained. This technique is simple and inexpensive, but experiences significant heat losses and requires large volumes to store useful amounts of energy (≈ 50 kWh/m^3) [3]. This makes conventional methods unsuitable for many buildings and for long term heat storage.

Thermochemical energy storage (TCES) stores energy using a reversible physical or chemical process like water-vapour adsorption. These techniques are suitable for long term storage, are much more compact than conventional methods, and often do not require the use of any toxic chemicals [4].

Despite the advantages of TCES, this technology is not yet commercialized. One of the main reasons for this is the lack of suitable materials to make this technology technically and economically feasible. Therefore, material development is necessary and of great interest. Furthermore, the developed materials should be pellets, briquettes, or granules to reduce pressure drops through flow systems within an adsorption column and increase ease of handling. Finally, the materials should be mechanically durable and hydrothermally stable so that they do not break down during use or in handling. In this study, the energy storage performance, mechanical durability, and hydrothermal stability of five materials have been analyzed and compared.

2.3.2 Selected Materials for Study

In this study titanium silicate molecular sieve (Ti-Si), flax shives, MCM-41, SAPO-34, and silica gel were tested. Apart from Ti-Si, all of these materials have been studied for TCES or other water-vapour adsorption applications [5–12].

Ti-Si is a synthetic aluminosilicate zeolite typically used as an adsorbent and catalyst. It was selected since it is hydrophobic and hydrothermally stable [13], so it was hypothesized that it could be regenerated at low temperatures and would be able to withstand multiple water vapour adsorption cycles.

Flax shives are heterogenous materials that are a bi-product of flax processing. It was selected for this study since it is an inexpensive material with a high-water uptake capacity (0.05-0.9 g/g) [14]. This is favourable since the working water vapour adsorption capacity ($q_{adsorption} - q_{desorption}$) increases the energy storage density (eq. 2.1). Also, adsorbent costs are estimated to be one of the major contributors to adsorption-based energy storage system prices, and therefore the affordability of flax shives is a big advantage [4, 15, 16].

$$ESD = \frac{\left(\int_{q_{desorption}}^{q_{adsorption}} \Delta H_{ads}(q)dq\right)}{V} \tag{2.1}$$

where ESD is the energy storage density (kWh/m^3), $q_{adsorption}$ is the amount of water vapour adsorbed under the adsorption conditions (kg), $q_{desorption}$ is the amount of water vapour adsorbed under the desorption conditions (kg), ΔH_{ads} is the heat of adsorption as a function of the amount of water vapour adsorbed (kWh/kg), and V is the volume occupied by the adsorbent bed (m^3).

MCM-41 is a mesoporous aluminosilicate material with large pore volumes (0.73-1.30 cm^3/g) and BET surface areas (758-1137 m^2/g) [5, 17–19]. This hydrophilic material is often used as a catalyst. It has an S-shaped water-vapour adsorption isotherm (Figure 2-1), exceptionally high water-vapour adsorption capacities (0.57-0.90 g/g), and relatively high heats of adsorption (40-60 kJ/mol) [5, 19–21]. Furthermore, pure MCM-41 and MCM-41-based composites have been tested for thermochemical energy storage applications and these materials showed high energy densities (Table 2-1). Therefore, it is expected to have high energy storage density while being easy to regenerate.

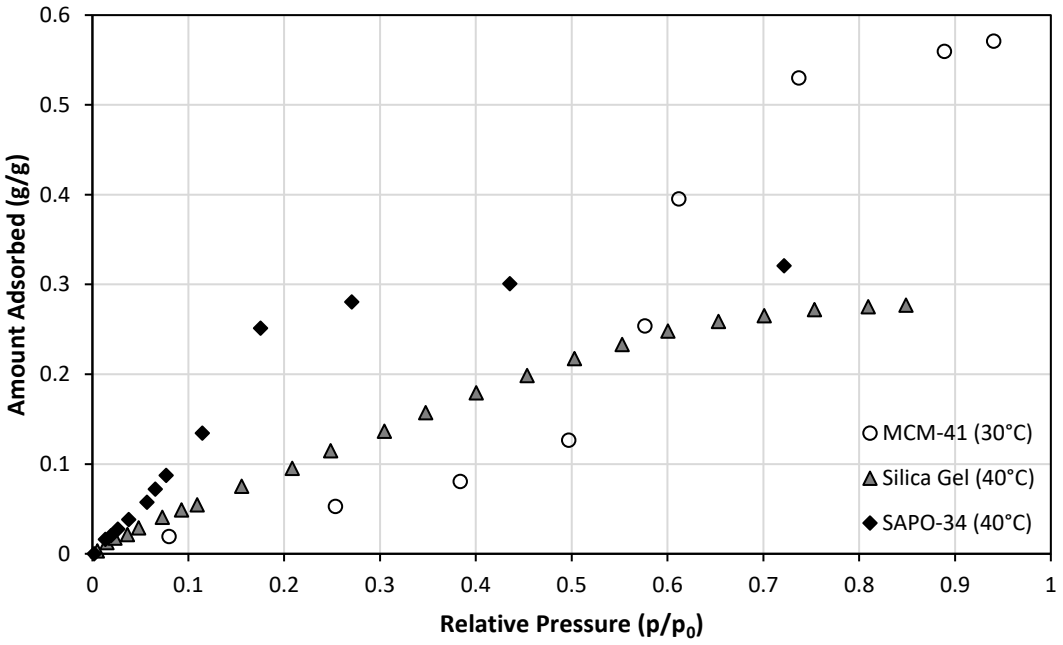

Figure 2-1. Water vapour adsorption isotherms for MCM-41 at 30°C [20], silica gel 40°C [22], and SAPO-34 at 40°C [11].

Table 2-1. Summary of literature water uptake capacity and specific energy values for pure MCM-41 and MCM-41 composites.

Material	Relative Humidity (%)	Water Uptake Capacity (g/g)	Specific Energy (kJ/kg)	Reference
Pure MCM-41	94	0.57	-	[20]
Pure MCM-41	30	0.04	-	[19]
MCM-41/$AlSO_4$	30	0.17	612	[19]
MCM-41/KCl	95	0.55	-	[23]
MCM-41/PEG*	-	-	102	[18]
MCM-41/$CaCl_2$	70	0.75	2000	[24]

*PEG is a phase-change energy storage material, not a sorption material

SAPO-34 (Silico-alumino-phosphate) is a hydrophilic synthetic microporous zeolite. It is another commonly studied advanced material for water vapour adsorption and adsorption-based thermal energy storage [7, 10, 25]. This is due to its high energy storage capacity at low humidity levels and the fact that it can be easily regenerated due to its S-Shaped isotherm (Figure 2-1).

Silica gel is a popular commercial desiccant with a high water-uptake capacity (Figure 2-1). Silica gel and silica gel-based composites have also been studied for thermochemical energy storage applications [10, 12, 26]. Pure silica gel and composites have achieved high energy storage densities after modest regeneration temperatures (94-350 kWh/m^3) [10, 12, 27]. Furthermore, silica gel is an inexpensive adsorbent that is commercially available.

2.4 Materials and Methods

Five adsorbent materials were tested for their mechanical durability and energy storage performances. All of the materials were received as pellets or granules or were pelletized to be able to use them in a lab-scale adsorption column. The mechanical durability of the materials was assessed using a standard drop test [28]. Lab-scale energy storage experiments were performed using a procedure and set-up similar to those described in [29]. Data from these experiments were used to calculate the energy storage density (ESD) and thermal power.

2.4.1 Materials

The titanium silicate (Ti-Si) molecular sieve powder sample was purchased from ACS Material LLC (Pasadena, CA, USA). The powder was pelletized following the pelletizing method described by V. Finsy *et*

al. [30] using poly(vinyl alcohol) (PVA) material (MilliporeSigma Canada Co., Oakville, ON, Canada) as binder. Approximately 3.36 g of PVA was mixed with 40 g of deionized water in a glass beaker with a thermometer to monitor the temperature of the liquid. The mixture was increased to 90°C with continuous stirring to obtain a clear homogeneous solution. 10 g of the PVA/water solution was added to 11.37 g of Ti-Si powdered material to make a paste-like mixture. The Ti-Si paste was then spread on top of a Teflon sheet and dried in the oven at 190°C for 9 hours. The dried Ti-Si/PVA (94:6 weight ratio) material was then crushed and sieved to the desired particle size (12-20 mesh or 0.841 – 2.38 mm).

Pure flax shives were received from SWM International (Alpharetta, GA, USA). Pelletization of flax shives into discs (2.5 cm diameter, 0.2 cm thickness) was attempted by crushing flax shives into a fine powder via pestle and mortar then using a die and punch with a hydraulic press at 100 MPa for 10 min without binder; this was not successful. The same procedure was repeated but with a 22 wt% addition of canola meal as a binder [31], but this was also not successful, possibly because this was done at room temperature. Large flax shive briquettes (7 cm diameter, 2 cm height) were also received from SWM International (Alpharetta, GA, USA). These flax shive briquettes were ripped by hand into smaller pieces (0.5-1.3 cm diameter, 1.3-2.1 cm length) so that they could fit into the lab-scale adsorption column.

MCM-41 was received as a powder from ACS Materials, LLC (Pasadena, CA, USA), and it was pelletized into discs (2.5 cm diameter, 0.2 cm thickness) using a die and punch and a hydraulic press. It was pressed for 10 min at 100 MPa without binder. According to literature this should not affect the material structure or properties [32]. The discs were then crushed using a mortar and pestle and sieved to a 12-20 mesh size (0.841 – 2.38 mm).

SAPO-34 was received as a powder from ACS Materials, LLC (Pasadena, CA, USA) and sent to the Material Center at Dresden University of Technology (Dresden, Germany), where it was pelletized into spherical particles using a proprietary binder and binding process. The particle diameters range was 1-2 mm.

Silica gel was received from XEBEC Adsorption Inc. (Blainville, QC, Canada) as large granular particles. The particles were crushed using a mortar and pestle and sieved into smaller particles (12-20 mesh or 0.841 – 2.38 mm).

2.4.2 Drop Test Apparatus and Procedure

A standard drop test was used to evaluate the mechanical durability of the adsorbent particles [33–35]. They were dropped 4 times from a height of 1.85 m onto a metal plate, and their mechanical durability was based on the mass retained after the 4 drops (eq. 2.2). In order to ensure consistent drops, particles

were placed on a piano hinge 1.85 m above the metal plate. The hinge had holes cut in it so that when the hinge would swing open, it would cause the loaded particle to drop onto the metal plate. By using the piano hinge, all particles were dropped uniformly, whereas dropping the particles by hand may have resulted in inconsistent results due to the experimenter inadvertently increasing or decreasing the speed at which they release the particle. Before dropping the particles, their mass was measured and recorded using a Mettler Toledo (Columbus, OH, USA) PR503 precision balance with an uncertainty of ± 0.002 g. Additionally, following each drop, the particles were sieved, and the mass of particles was measured and recorded.

$$\%\, mass\ retained = \frac{m_{final}}{m_{initial}} \times 100\% \tag{2.2}$$

Where $\%\, mass\ retained$ is the percentage of the initial mass that was retained after being dropped, m_{final} is the mass of the sample after being dropped, and $m_{initial}$ is the initial mass of the sample.

2.4.3 Energy Storage Apparatus and Procedure

The lab-scale energy storage set-up and testing methodology are similar to those described in [29]. The schematic of the system is provided in Figure 2-2. The adsorption column was packed with 5-50 g of the adsorbent material. Next, air with a relative humidity (RH) of less than 3 % was heated to a set regeneration temperature and passed over the column to dehydrate the sample. Once the RH exiting the column was less than 3% for 15 minutes, the dehydration was considered to be complete. After dehydration, the column was sealed with valves and cooled to room temperature (22°C) overnight. For the adsorption portion of the experiments, air at approximately 22°C was humidified to a chosen RH (e.g. 50%) and then passed over the column at a given flow rate. The RH at the inlet and the outlet of the column was measured with an Omega Engineering Inc. (Norwalk, CT, USA) HX-15 RH probe, with readings valid from 3% to 95% RH with a ± 2% RH uncertainty. The flow rate was controlled by an MCW-series mass flow controller (MFC), purchased from Alicat Scientific Inc. (Tucson, AZ, USA). The temperature difference at the inlet and outlet of the column was also measured and recorded, using thermocouples. With this information, it was possible to calculate the amount of energy released during adsorption, using eq. 2.3. Furthermore, by recording the temperature, RH and flow rates throughout the experiment, the breakthrough behaviour, thermal power, and temporal temperature profile could be determined. The maximum thermal power was calculated as the product of the maximum temperature lift, mass flow rate, and specific heat capacity. Note that different columns and flow rates were used for each adsorbent as summarized in (Table 2-2) due to availability of the adsorbent and, in the case of flax shives, the pressure drop associated with higher flow rates.

$$Q_{adsorption} = \int_0^t \dot{m}_{air} C_{p,air} (T_{out} - T_{in}) dt \tag{2.3}$$

where $Q_{adsorption}$ is the heat released during adsorption (kJ), t is the amount of time the adsorption takes place (min), $m_{air}$is the mass flow rate of the air (kg/min), $C_{p,air}$ is the specific heat capacity of the humid air (kJ/kg°C), T_{out} is the temperature at the outlet of the column (°C), and T_{in} is the temperature at the inlet of the column (°C).

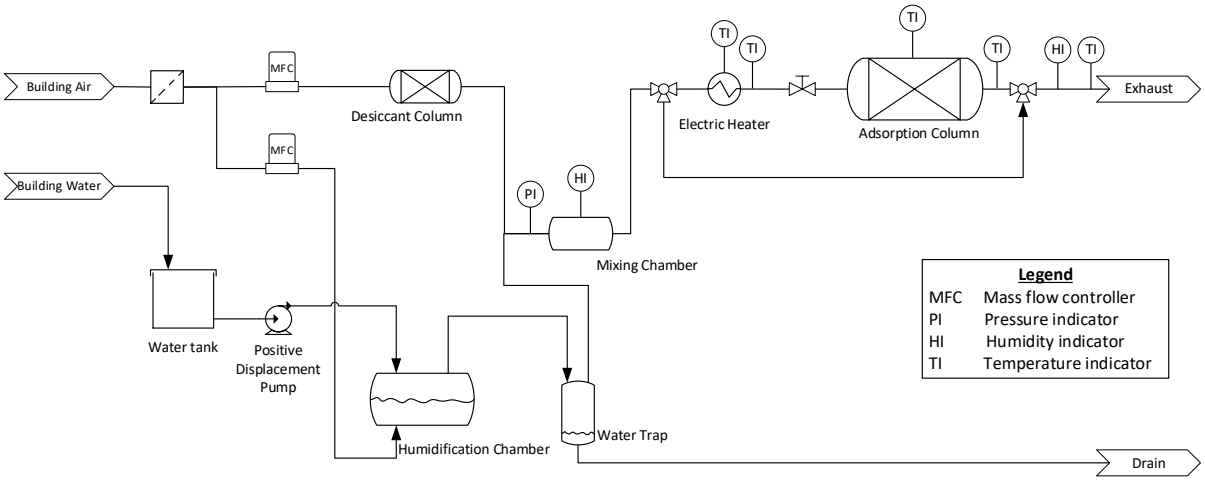

Figure 2-2. Schematic of the lab-scale open adsorption thermal energy storage system used in this study. All measurements were recorded electronically using the LabVIEW software.

Table 2-2. List of column dimensions, adsorbent masses, and volumetric flow rates used for each tested material.

Material (-)	Column Length (cm)	Column Volume (cm^3)	Adsorbent Mass (g)	Flow Rate (SLPM)
Ti-Si	7.6	6.56	3.005	12
Flax Shives	7.1	62.8	24.034	18
MCM-41	7.6	6.56	1.959	12
SAPO-34	7.1	62.8	48.356	24
Silica Gel	7.1	62.8	49.132	24

2.5 Results and Discussion

All materials underwent a standard drop test to assess their mechanical durability. They were also tested using the lab-scale energy storage apparatus to determine their energy storage density, temperature lifts, thermal power, pressure drop, and kinetics. The effect of multiple adsorption and desorption cycles on material performance was also investigated.

2.5.1 Mechanical Durability

All materials were subjected to a standard drop test [33–35], where they were dropped four times from 1.85 m and their mass was measured after each drop. All materials showed less than a 5% reduction in mass after the four drops, except for flax shives, which showed a 35% reduction in mass after the four drops and SAPO-34 which showed a 15% reduction (Figure 2-3). This connotes that flax shives briquettes and SAPO-34 may easily break apart into smaller pieces during handling and use, which will be a disadvantage, whereas the other adsorbents are more resilient to physical impact.

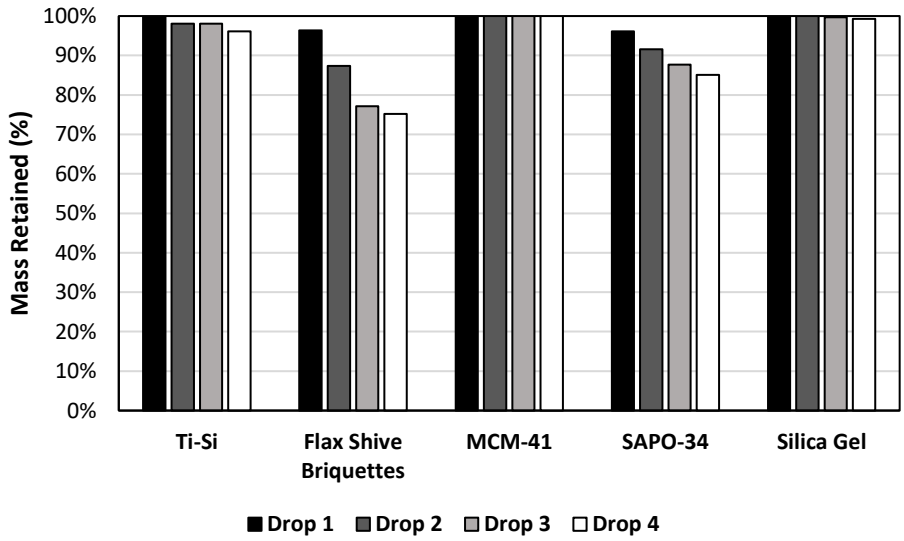

Figure 2-3. Percentage of mass retained after dropping particles four times from 1.85 m onto a metal plate.

2.5.2 Energy Storage Performance

All materials were tested at an inlet humidity of 50% RH at room temperature (22°C) in the feed after a regeneration temperature of 80°C and 120°C, and the corresponding energy storage density values are shown (Figure 2-4). They all showed higher ESD at a regeneration temperature of 120°C than at 80°C, except for MCM-41. This is because generally at higher regeneration temperatures more water-vapour

can be desorbed from the surface of the adsorbent creating more vacant sites for adsorption to take place during the adsorption portion of the experiment. The reason MCM-41 saw the opposite trend was likely because regeneration temperature has minimal effects on the adsorption and energy storage capacity in this range for that adsorbent. Therefore, for MCM-41 in Figure 2-4, the observed variation in ESD is likely due to error introduced by measurement equipment rather than the effects of regeneration temperature.

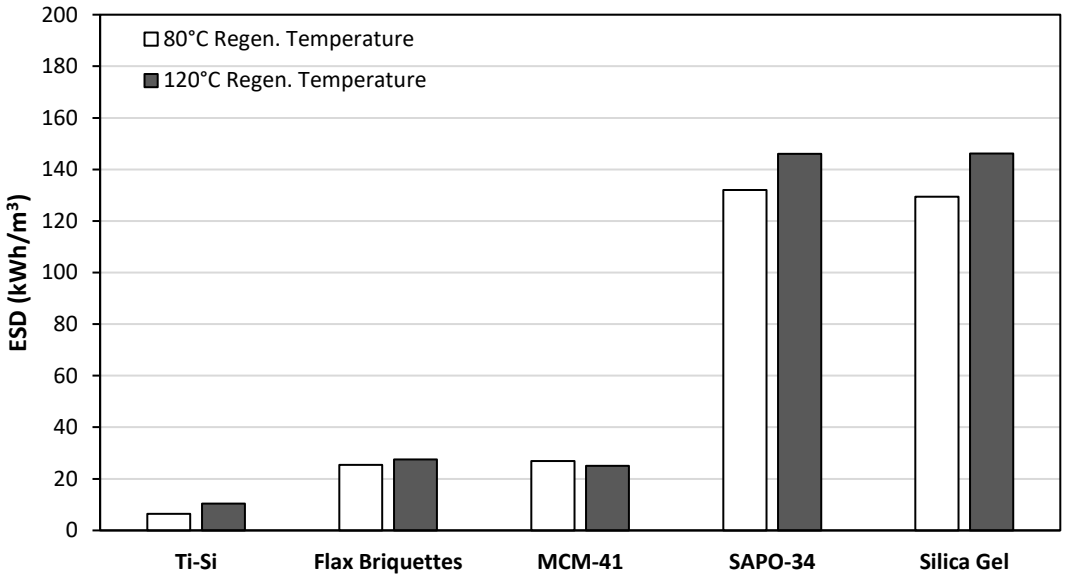

Figure 2-4. ESD values determined after regeneration temperatures of 80°C and 120°C with an adsorption inlet RH of 50%.

In Figure 2-4, SAPO-34 and silica gel outperform the other materials in terms of energy storage density. However, at higher humidity levels MCM-41 is competitive with silica gel and SAPO-34 as can be seen in (Figure 2-5). This is because ESD is directly proportional to the amount of water-vapour adsorbed (eq. 2.1). This behaviour can be explained by the shape of the isotherms of these three materials, since SAPO-34 and silica gel have much higher water uptake capacities at lower RH levels than MCM-41, which has a very low capacity until inlet RH values reach to around 65% RH (Figure 2-1).

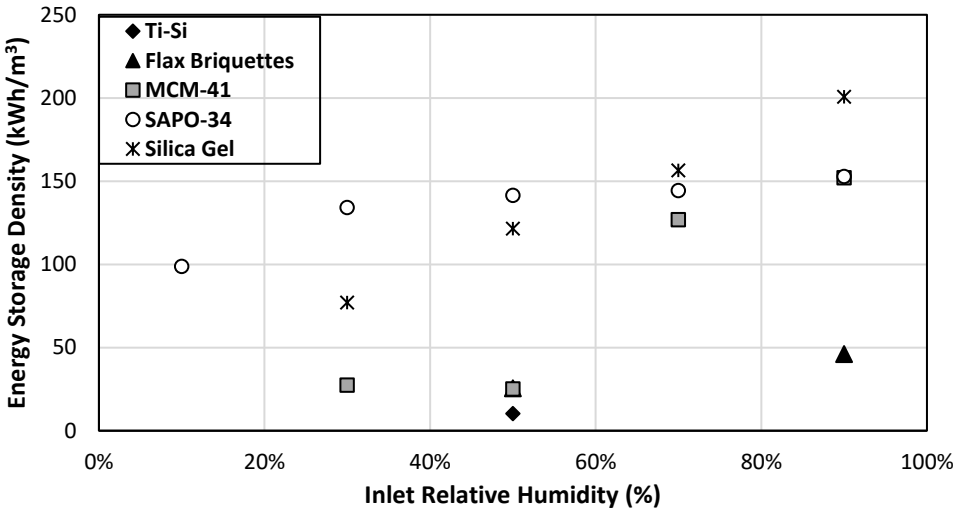

Figure 2-5. ESD of all materials studied at different adsorption inlet RH levels, after a regeneration temperature of 120°C.

Another factor significantly impacting the ESD is the bulk density, since it is directly proportional to the amount of active material that can fit in a given volume. The bulk densities of all the tested materials were measured using a graduated cylinder and scale and are shown in Figure 2-6. It is known that the bulk density is related to the pelletization process and material type. For example, Alcañiz-Monge *et al*. observed that MCM-41 pellets had a bulk density of 410 kg/m^3 when pelletized at 60 MPa but a bulk density of 1120 kg/m^3 when pelletized at 420 MPa [32]. This implies that by pelletizing MCM-41 at higher pressures, higher ESD values can be obtained. Furthermore, adjustments to pelletization techniques of the other materials should be investigated, with the goal of increasing bulk density and not negatively affecting the material properties.

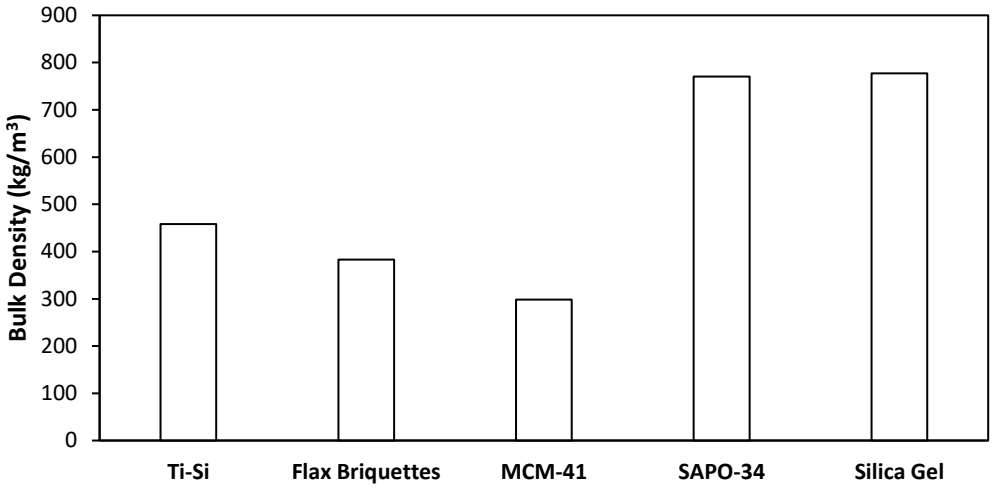

Figure 2-6. Bulk densities of all tested materials, measured using a precision scale and graduated cylinder.

The maximum thermal power, calculated by multiplying the maximum temperature lift with the mass flow rate and the specific heat capacity of humid air, was also compared for all materials at different inlet RH levels (Figure 2-7).

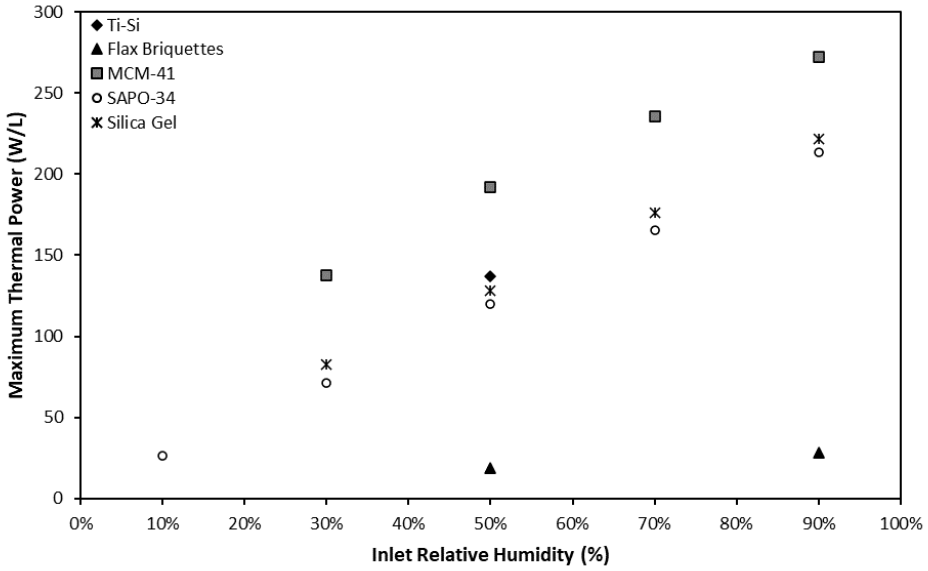

Figure 2-7. Maximum thermal power at different adsorption inlet RH values for different adsorbents studied after a regeneration temperature of 120°C.

It was found that maximum thermal power showed a linear relationship with inlet RH for MCM-41, SAPO-34, silica gel, and flax shives. No trend was observed with Ti-Si since it was only tested at an inlet RH of 50% because of its low ESD values. Note that only the trends should be observed in Figure 2-7 and that

the maximum thermal power values cannot be justly compared between materials. This is because they were tested using different flow rates, column sizes, and amounts of active material (Table 2-2). These are key operating parameters that will significantly affect the maximum power values. Different conditions were used since there was a limited quantity of MCM-41 and Ti-Si and also because the flax shives material caused a large pressure drop and the experimental apparatus could not handle the pressure drop of flax shives being tested at 24 SLPM, as silica gel and SAPO-34 were.

2.5.3 Effects of Multiple Cycles

Since MCM-41, SAPO-34, and silica gel had the highest energy storage performances, they were subjected to further testing. Multiple adsorption and desorption cycles were performed on these materials at different conditions, in order to see if the materials could withstand multiple cycles without a decrease in performance. The effect of number of adsorption and desorption cycles on energy storage density is seen in Figure 2-8. Note that one cycle refers to one full adsorption and desorption experiment. Additionally, a list of the experimental conditions for each adsorption and desorption cycle can be found in the supporting information.

MCM-41, SAPO-34, and silica gel all showed a decrease in ESD of less than 5% after performing 20 or more cycles. The MCM-41 ESD values consistently oscillated around 120 kWh/m^3 for 22 cycles. The SAPO-34 ESD decreased from 147 kWh/m^3 to 141 kWh/m^3 between cycles 12 and 17, but then remained constant for the remaining cycles. The silica gel ESD decreased from 128 kWh/m^3 to 122 kWh/m^3 between cycle 1 and 25, but the majority of this decrease was observed in the first seven cycles. Additionally, upon visual inspection, there were no obvious changes to the materials, except for MCM-41, which appeared slightly more yellow (see figures in supporting information). Note that MCM-41 shows a greater variation in ESD values. This is because it was tested in a smaller adsorption column than SAPO-34 and silica gel (Table 2-2), so the uncertainty in the measurements was more significant.

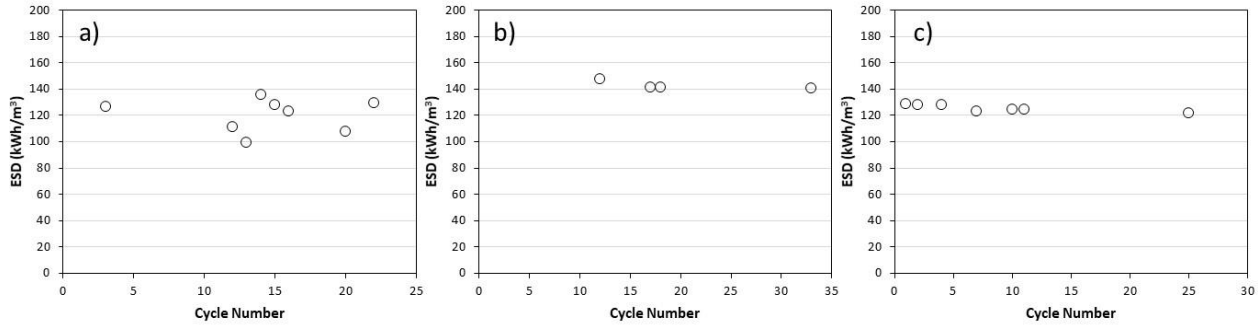

Figure 2-8. Effect of number of adsorption and desorption cycles on the ESD of

a) MCM-41 at a flow rate of 12 SLPM with an adsorption inlet humidity of 70% RH after a regeneration temperature of 120°C
b) SAPO-34 at a flow rate of 24 SLPM with an adsorption inlet humidity of 50% RH after a regeneration temperature of 120°C
c) Silica gel at a flow rate of 24 SLPM with an adsorption inlet humidity of 50% RH after a dry air purge with air at 0-3% RH at room temperature instead of a standard regeneration at a high temperature.

2.6 Conclusions

In this study, five adsorbents were pelletized and tested to determine their mechanical stability, energy storage performance, and their cyclic stability. Materials were dropped four times onto a metal plate from a height of 1.85 m, and all of the materials showed a mass retention of at least 95%, except for flax shives and SAPO-34. The flax shive briquettes lost 35% of their initial mass after the four drops and the pelletized SAPO-34 lost 15% of its initial mass. This may imply that there could be difficulties with commercializing either of these materials, so alternative binding processes should be investigated and considered.

Silica gel, SAPO-34, and MCM-41 all showed high energy densities (>150 kWh/m^3). SAPO-34 showed high performance at all inlet RH levels, silica gel performed well from 50-90% inlet RH, and MCM-41 only performed well from 70-90% inlet RH. These observations were attributed to the shape of the isotherms of these adsorbent materials.

The stability of silica gel, SAPO-34, and MCM-41 was assessed by performing multiple adsorption and desorption cycles on the materials. All three materials underwent 20 or more cycles with no obvious visual changes, apart from MCM-41 which became slightly more yellow. MCM-41 ESD appeared to stay approximately constant for 22 cycles. SAPO-34 ESD decreased by 4% between cycles 12 and 17 then remained constant. Silica gel ESD decreased by 5% between cycle 1 and 25, with the majority of the decrease being observed in the first 7 cycles.

Silica gel, SAPO-34, and MCM-41 all appear to be suitable candidates for thermal energy storage, each with its own unique advantages. SAPO-34 would be well suited to applications where humid air is not readily available, MCM-41 would be a good candidate for applications where infrastructure to regenerate the material at high temperatures is not available but very humid air is. Silica gel is the least expensive and is the only material which is commercially available in large quantities.

Future work should be done to optimize operating parameters and improve the energy storage density of the materials through material modifications like hygroscopic salt impregnation. The energy storage density of these materials could be improved by making changes to the pelletization process which improve bulk density. For example, pelletizing MCM-41 at a higher pressure would increase its bulk density and therefore energy storage density.

2.7 References

[1] Natural Resources Canada, “Energy Efficiency Trends in Canada 1990 to 2013,” 2019.

[2] IEA, “Renewables 2019,” 2019.

[3] D. Lefebvre and F. H. Tezel, “A review of energy storage technologies with a focus on adsorption thermal energy storage processes for heating applications,” *Renew. Sustain. Energy Rev.*, vol. 67, pp. 116–125, 2017.

[4] L. Scapino, H. A. Zondag, J. Van Bael, J. Diriken, and C. C. M. Rindt, “Sorption heat storage for long-term low-temperature applications: A review on the advancements at material and prototype scale,” *Appl. Energy*, vol. 190, pp. 920–948, 2017.

[5] J. S. Oh, W. G. Shim, J. W. Lee, J. H. Kim, H. Moon, and G. Seo, “Adsorption Equilibrium of Water Vapor on Mesoporous Materials,” *J. Chem. Eng. Data*, vol. 48, no. 6, pp. 1458–1462, 2003.

[6] S. Ghanbari and C. H. Niu, “Characteristics of oat hull based biosorbent for natural gas dehydration in a PSA process,” *J. Nat. Gas Sci. Eng.*, vol. 61, no. November 2018, pp. 320–332, 2019.

[7] S. K. Henninger, F. Jeremias, H. Kummer, P. Schossig, and H. M. Henning, “Novel sorption materials for solar heating and cooling,” *Energy Procedia*, vol. 30, pp. 279–288, 2012.

[8] M. J. Goldsworthy, “Measurements of water vapour sorption isotherms for RD silica gel, AQSOA-Z01, AQSOA-Z02, AQSOA-Z05 and CECA zeolite 3A,” *Microporous Mesoporous Mater.*, vol. 196, pp. 59–67, 2014.

[9] M. Tokarev, L. Gordeeva, V. Romannikov, and I. Glaznev, “New composite sorbent $CaCl_2$ in mesopores for sorption cooling / heating,” vol. 41, pp. 470–474, 2002.

[10] J. Jänchen and H. Stach, “Adsorption properties of porous materials for solar thermal energy storage and heat pump applications,” *Energy Procedia*, vol. 30, pp. 289–293, 2012.

[11] A. Ristić, N. Z. Logar, S. K. Henninger, and V. Kaučič, “The performance of small-pore microporous aluminophosphates in low-temperature solar energy storage: The structure-property relationship,” *Adv. Funct. Mater.*, vol. 22, no. 9, pp. 1952–1957, 2012.

[12] G. Gartler, D. Jähnig, G. Purkarthofer, and W. Wagner, “Development of a high energy density sorption storage system,” in *Proceedings of Eurosun 2004*, 2004.

[13] S. P. Mirajkar, A. Thangaraj, and V. P. Shiralkar, “Sorption properties of titanium silicate molecular sieves,” *J. Phys. Chem.*, vol. 96, no. 7, pp. 3073–3079, 1992.

[14] S. Ghanbari and C. H. Niu, “Characterization of a High-Performance Biosorbent for Natural Gas Dehydration,” *Energy and Fuels*, vol. 32, no. 11, pp. 11979–11990, 2018.

[15] D. Lefebvre, “Thermal Energy Storage Using Adsorption Processes for Solar and Waste Heat Applications: Material Synthesis, Testing and Modeling,” 2016.

[16] B. Ugur and F. H. Tezel, “Thermal Energy Storage in Adsorbent Beds,” *M.A.Sc. Thesis Univ. Ottawa, Ottawa, Canada*, 2013.

[17] G. D. Mihai, V. Meynen, M. Mertens, N. Bilba, P. Cool, and E. F. Vansant, “ZnO nanoparticles supported on mesoporous MCM-41 and SBA-15: A comparative physicochemical and photocatalytic study,” *J. Mater. Sci.*, vol. 45, no. 21, pp. 5786–5794, 2010.

[18] L. Feng, W. Zhao, J. Zheng, S. Frisco, P. Song, and X. Li, “The shape-stabilized phase change materials composed of polyethylene glycol and various mesoporous matrices (AC, SBA-15 and MCM-41),” *Sol. Energy Mater. Sol. Cells*, vol. 95, no. 12, pp. 3550–3556, 2011.

[19] A. Jabbari-Hichri, S. Bennici, and A. Auroux, “Effect of aluminum sulfate addition on the thermal storage performance of mesoporous SBA-15 and MCM-41 materials,” *Sol. Energy Mater. Sol. Cells*, vol. 149, pp. 232–241, 2016.

[20] P. J. Branton, P. G. Hall, M. Treguer, and K. S. W. Sing, “Adsorption of carbon dioxide, sulfur dioxide and water vapour by MCM-41, a model mesoporous adsorbent,” *J. Chem. Soc. Faraday Trans.*, vol. 91, no. 13, pp. 2041–2043, 1995.

[21] S. Kittaka, S. Ishimaru, M. Kuranishi, T. Matsuda, and T. Yamaguchi, “Enthalpy and interfacial free energy changes of water capillary condensed in mesoporous silica, MCM-41 and SBA-15,” *Phys. Chem. Chem. Phys.*, vol. 8, no. 27, pp. 3223–3231, 2006.

[22] H. Oh, S. Lim, J. H. Kim, and C. Lee, “Adsorption Equilibria of Water Vapor on an Alumina/Zeolite 13X Composite and Silica Gel,” *J. Chem. Eng. Data*, vol. 62, pp. 804–811, 2017.

[23] L. Liu, L. Y. Kou, Z. C. Zhong, L. Y. Wang, L. F. Liu, and W. Li, “Preparation and humidity sensing properties of KCl/MCM-41 composite,” *Chinese Phys. Lett.*, vol. 27, no. 5, 2010.

[24] Y. Aristov, M. Tokarev, L. Gordeeva, V. Romannikov, Y. Pankrat, I. Glaznev, G. Echevsiy, “New Composite Sorbent "$CaCl_2$ in Mesopores of MCM-41 ” For Sorption Cooling/Heating,” 2000, pp. 98–103.

[25] N. Yu, R. Z. Wang, and L. W. Wang, “Sorption thermal storage for solar energy,” *Prog. Energy Combust. Sci.*, vol. 39, no. 5, pp. 489–514, 2013.

[26] E. Courbon, P. D'Ans, A. Permyakova, O. Skrylnyk, N. Steunou, M. Degrez, M. Frère, “Further improvement of the synthesis of silica gel and $CaCl_2$ composites: Enhancement of energy storage density and stability over cycles for solar heat storage coupled with space heating applications,” *Sol. Energy*, vol. 157, no. September, pp. 532–541, 2017.

[27] J. Jänchen, D. Ackermann, H. Stach, and W. Brösicke, “Studies of the water adsorption on Zeolites and modified mesoporous materials for seasonal storage of solar heat,” *Sol. Energy*, vol. 76, no. 1–3, pp. 339–344, 2004.

[28] M. M. Abdulmumini, “The Effect of Pellets Physiscal Properties on Handling Pelleted Biomass Material in Practical Use,” University of Greenwich, 2016.

[29] Y. Hua, B. Ugur, and F. Handan Tezel, “Adsorbent screening for thermal energy storage application,” *Sol. Energy Mater. Sol. Cells*, vol. 196, no. December 2018, pp. 119–123, 2019.

[30] V. Finsy, L. Ma, L. Alaerts, D. E. De Vos, G. V Baron, and J. F. M. Denayer, “Microporous and Mesoporous Materials Separation of CO_2 / CH_4 mixtures with the MIL-53 (Al) metal – organic framework,” *Microporous Mesoporous Mater.*, vol. 120, no. 3, pp. 221–227, 2009.

[31] Bayartogtokh Rentsen, “Characterization of Flax Shives and Factors Affecting the Quality of Fuel Pellets from Flax Shives,” 2010.

[32] J. Alcañiz-Monge, G. Trautwein, M. Pérez-Cadenas, and M. C. Román-Martínez, “Effects of compression on the textural properties of porous solids,” *Microporous Mesoporous Mater.*, vol. 126, no. 3, pp. 291–301, 2009.

[33] M. I. Al–Widyan and H. F. Al–Jalil, “Stress-Density Relationship and Energy Requirement of Compressed Olive Cake,” *Appl. Eng. Agric.*, vol. 17, no. 6, pp. 749–753, 2001.

[34] K. Khankari, M. Shrivastava, and R. Morey, “Densification characteristics of rice hulls,” *Am. Soc. Agric. Eng.*, vol. Paper No., 1989.

[35] P. Sah, B. Singh, and U. Agrawal, “Compaction behavior of straw,” *J. Agric. Eng.*, vol. 18, no. 1, pp. 89–96, 1980.

2.8 Supplemental Information

Table 2-3. List of experimental conditions for all of the relevant SAPO-34 adsorption cycles.

Cycle Number	Regeneration Temperature (°C)	Relative Humidity (%)	Flow Rate (SLPM)
12	120	50%	24
13	120	70%	24
14	120	10%	24
15	120	30%	24
16	120	90%	24
17	120	50%	24
18	120	50%	24
19	120	70%	24
20	240	50%	24
21	200	50%	24
22	200	10%	24
23	200	30%	24
24	200	70%	24
25	200	90%	24
26	200	50%	24
27	240	50%	24
28	240	10%	24
29	240	30%	24
30	240	70%	24
31	240	90%	24
32	240	50%	24
33	120	50%	24

Table 2-4. List of experimental conditions for all MCM-41 adsorption cycles.

Cycle Number	Regeneration Temperature (°C)	Relative Humidity (%)	Flow Rate (SLPM)
1	80	50%	12
2	120	50%	12
3	120	90%	12
4	120	70%	12
5	120	30%	12
6	50	70%	12
7	80	70%	12
8	22	70%	12
9	22	70%	12
10	22	70%	12
11	120	70%	12
12	120	70%	12
13	120	70%	12
14	120	70%	12
15	120	70%	12
16	120	70%	12
17	160	90%	12
18	200	90%	12
19	240	90%	12
20	120	70%	12
21	120	70%	24
22	120	70%	12
23	120	70%	12

Table 2-5. List of experimental conditions for all silica gel adsorption cycles.

Cycle Number	Regeneration Temperature (°C)	Relative Humidity (%)	Flow Rate (SLPM)
1	22*	10%	24
2	22	30%	24
3	22	50%	24
4	22	70%	24
5	22	90%	24
6	22	50%	12
7	22	50%	18
8	22	50%	15
9	22	50%	21
10	22	50%	24
11	22	50%	24
12	22	50%	24
13	22	50%	24
14	22	50%	24
15	22	50%	6
16	120	50%	24
17	60	50%	24
18	22	50%	3
19	22	30%	6
20	22	70%	6
21	22	30%	15
22	22	70%	15
23	200	50%	24
24	22	10%	24

*Note that dry air (0-3% RH) was used as a purge gas to regenerate the column.

Figure 2-9. Photo of crushed titanium silicate molecular sieve particles sieved to 12-20 mesh size.

Figure 2-10. Photo of flax shive briquette pieces.

Figure 2-11. Photo of crushed MCM-41 particles sieved to 12-20 mesh size before (left) and after (right) lab-scale energy storage testing.

Figure 2-12. Photo of spherical SAPO-34 pellets.

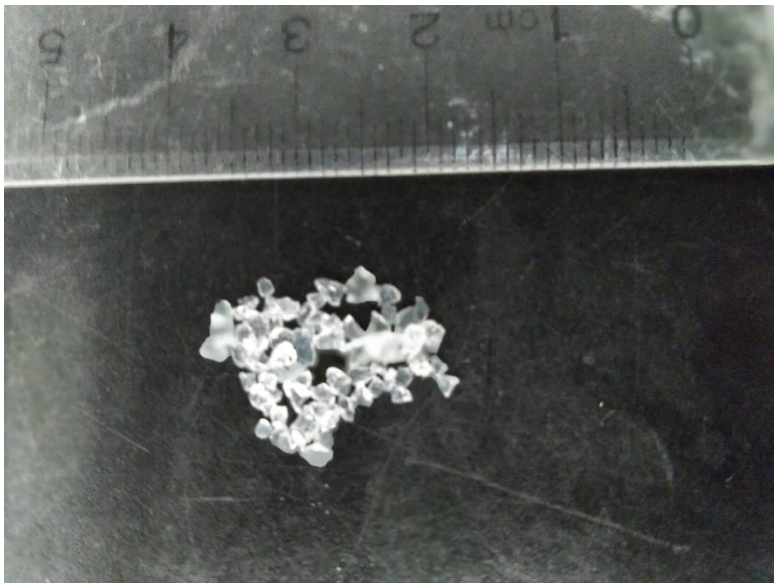

Figure 2-13. Photo of crushed silica gel sieved to 12-20 mesh size.

Chapter 3 - Optimization of operating conditions for an open bulk-scale silica gel/water vapour adsorption energy storage system

Curtis Strong, University of Ottawa

Ye Carrier, University of Ottawa

F. Handan Tezel, University of Ottawa

Abstract

Thermal energy storage is an effective way to reduce the energy supply and demand mismatch and facilitate more widespread use of renewable energy sources like wind and solar power. The objective of this study was to optimize the performance of an open bulk-scale silica gel/water vapour adsorption-based energy storage system by systematically manipulating key operating parameters (relative humidity, particle size, desorption temperature, and flow rate) and observing the effects of these variables. It was found that the optimal conditions for the 50 g system used were a desorption temperature of 120°C, a flow rate of 24 SLPM, an adsorption relative humidity of 90%, and a 12-20 mesh particle size. Under these conditions an energy storage density of 200.7 kWh/m^3 (252.1 Wh/kg) was achieved, with a maximum temperature lift of 28.5°C. The maximum and average thermal power of the system under these optimal conditions were 15.4 W and 5.9 W or 245.2 W/L (308 W/kg) and 93.9 W/L (118 W/kg), respectively. The breakthrough time was 11 min, and it took 126 min for the column outlet humidity to reach 95% of its maximum value.

Keywords: Thermochemical energy storage, Thermal energy storage, Open sorption system, Silica gel, Operating conditions, Optimization, Water adsorption by silica gel

Submitted to Applied Energy

3.1 Nomenclature

a	Regression constant (SLPM·min)
b	Regression constant (min)
C_p	Specific heat capacity (kJ/kg·°C)
$C_{p,g}$	Specific heat capacity of the gas (kJ/kg·°C)
$C_{p,s}$	Specific heat capacity of the sorbent (kJ/kg·°C)
ESD	Energy storage density (kWh/m^3)
$ESD_{theoretical}$	Theoretical energy storage density (kWh/m^3)
$\dot{m}$	Mass flow rate (kg/s)
P	Total Pressure (kPa)
Q	Energy released (kJ)
q	Mass of adsorbate adsorbed (g/g)
RH	Relative humidity (%)
RH_{in}	Relative humidity at the column inlet (%)
RH_{out}	Relative humidity at the column outlet (%)
t	Time (s)
$t_{95\%}$	95% saturation time (s)
T_{in}	Temperature at the inlet of the column (°C)
T_{max}	Maximum outlet temperature of the column (°C)
T_{out}	Temperature at the outlet of the column (°C)
Y_f	Mass fraction of sorbate in carrier gas (-)

Greek Letters

ΔH_{ads}	Heat of adsorption (kJ/mol)

ρ_{bulk} Bulk density of the adsorbent bed (kg/m^3)

3.2 Abbreviations

ESD Energy storage density

MFC Mass flow controller

PTF Pure thermal front

RH Relative humidity

TES Thermal energy storage

3.3 Introduction

The imminent effects of climate change, the steady depletion of natural resources, such as oil and gas, and the increasing energy demand in developing countries have created a crucial demand for more sustainable energy production and use [1]. This demand has incentivized more widespread use of alternative energy sources like solar and wind power [2]. These renewable energy sources are more sustainable and produce fewer emissions, but their power output may vary hourly, daily, or even seasonally. For example, solar panel power output depends heavily on the solar irradiance at a given time [3]. Energy demand is also dynamic. For example, in colder climates, far more energy is required in the winter months than in the summer months. This creates an energy supply and demand mismatch.

One solution to this mismatch problem is to store the energy when there is an energy surplus and release it when there is a deficit. There are several ways to achieve this for different applications. For example, lithium-ion batteries are often used to store electrical energy. However, thermal energy storage (TES) should also be considered, since space heating accounts for 60-70% of all residential energy consumption in Canada and the European Union [4, 5]. Since it is inefficient to convert thermal energy to electrical energy, thermal energy cannot easily be stored as electrical energy. Contemporary TES methods include sensible, latent, and thermochemical thermal energy storage [6].

Sensible heat storage typically involves a heavily insulated hot water tank, or other media, whose temperature is increased by heating it with excess thermal energy, then the energy is stored until it is required. This simple method is the most common form of TES, but it is subject to significant heat losses over time [7] and has low energy storage density (ESD) (≈30 kWh/m^3), meaning that it requires large volumes to store useful amounts of heat [8]. This is impractical in many residential and industrial settings,

since buildings do not generally have free space to retrofit large infrastructure. Latent heat TES is another technology that is being developed, in which energy is stored by heating a solid until it liquefies, then the energy is released by allowing the liquid to solidify. This method has higher energy densities but also loses heat over time [8], and many proposed phase-change materials are toxic and corrosive [9, 10]. Thermochemical energy storage techniques store excess heat by using it to reverse an exothermic physical or chemical process like adsorption or a hydration reaction. The heat is then released by allowing the process to proceed forward. Thermochemical TES exhibits exceptionally high ESD values, often do not require any toxic or corrosive chemicals, and can store heat indefinitely [6, 11]. This makes adsorption-based TES a suitable candidate for compact energy storage applications.

Despite its promise, adsorption-based energy storage has yet to be commercialized successfully, even though several demonstration plants have been built [12–15]. This is likely, in part, due to the scarcity of concise and available experimentally obtained information regarding the effects and the optimization of the operating conditions of energy storage systems.

Silica gel is a hydrophilic amorphous adsorbent made up of mostly SiO_2 [16]. It is widely used as a desiccant material, commercially. Preliminary experiments and literature review have shown that silica gel is an excellent candidate for thermal energy storage [17–19]. This material is non-toxic, is thermally and chemically stable, shows good regeneration properties, has a high ESD, is inexpensive, and is commercially available [8, 20, 21]. It also has potential as a matrix material for various composites used in energy storage, heating, and cooling [22–26].

In this work, a water vapour adsorption energy storage system with 50 g of pure silica gel is used to systematically study the effects of manipulating relative humidity, regeneration temperature, particle size, and volumetric flow rate when using silica gel as the adsorbent material. The impact of these variables on temperature lifts, thermal power, ESD, and breakthrough behaviour is qualified, quantified, and optimized herein. This will hopefully serve as a useful reference for those developing adsorption-based TES system simulations and prototypes.

3.4 System analysis

3.4.1 Experimental set-up

The system used is the same as the one that was used by Hua *et al.* [18]. A schematic diagram of the set-up is shown in Figure 3-1. It uses compressed dry air provided by the University of Ottawa, which passes through an oil filter. The air stream is then split into two streams, one for dry air and one for humid air.

The flow rate in each stream is controlled by an Alicat Scientific MCW-series mass flow controllers (MFC), purchased from Alicat Scientific Inc. (Tucson, AZ, USA). The dry air stream passes over a desiccant column, full of $CaSO_4$ from Drierite Co. Ltd. (Xenia, OH, USA), which captures any residual moisture in the air, whereas the humid air stream passes through a bubbling chamber, where its humidity is increased to nearly 100% relative humidity (RH). After the bubbling chamber, the humid air goes through a condensation trap to condense any free moisture drops in the air. The flow rates of the humid and dry air streams are controlled to obtain the desired RH and then mixed in a chamber. The relative humidity of the combined stream is measured with an Omega Engineering Inc. (Norwalk, CT, USA) HX-15 relative humidity probe, with readings valid from 3% to 95% RH with a ± 2% RH uncertainty. The combined stream then flows to a three-way check valve and either bypasses the column or flows through an inline heater from Omega Engineering followed by the column packed with the adsorbent. The humidity and temperature are measured at various points in this set-up and then transmitted to and recorded by a computer. The insulated stainless-steel adsorption column has a volume of 62.8 cm^3 with a 3.39 cm inner diameter, a length of 6.96 cm, and it is packed with approximately 50 g of silica gel provided by XEBEC Adsorption Ltd. (Blainville, Québec, Canada). The column and the piping were covered in aluminum foil to form thermally insulating stagnant air pockets around the column and piping. This was to help mitigate heat transfer to the surroundings. Prior to packing the column, the silica gel adsorbent was crushed and then sieved to obtain different particle sizes to study the effect of particle size. A table of the mesh sizes used to sieve the particles is provided in Table 3-1. For example, the particle size “8 x 10 Mesh” would indicate particles sizes between 2.00 and 2.38 mm.

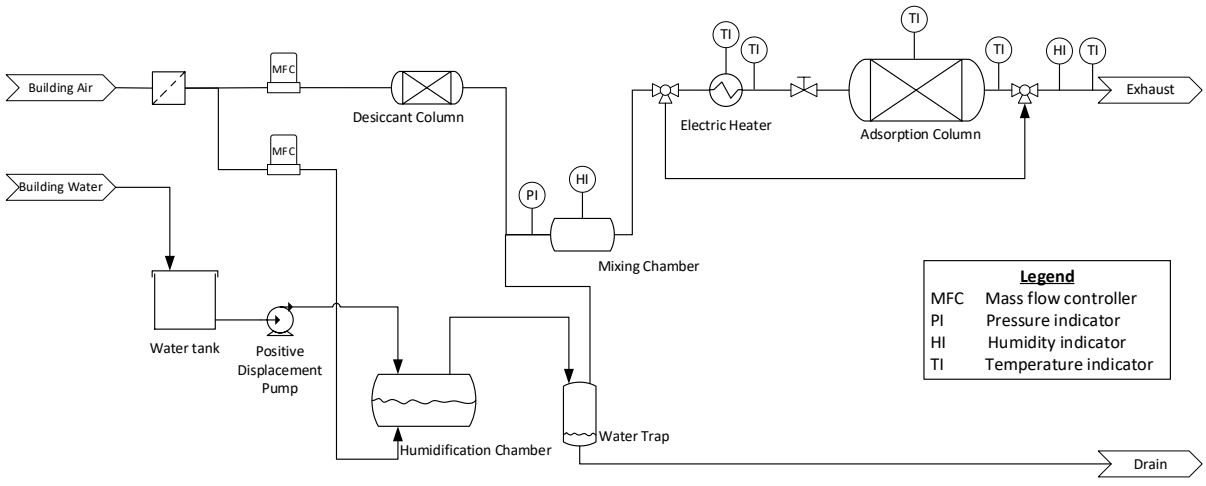

Figure 3-1. Schematic diagram of the adsorption thermal energy storage system. All measurements were recorded electronically using a LabVIEW software.

Table 3-1. Nominal sieve opening diameters for different standard mesh numbers.

Standard Mesh Number	Nominal Sieve Opening (mm)
8	2.38
10	2.00
12	1.68
20	0.841
50	0.297

3.4.2 Experimental method

For the regeneration (charging), of the adsorbent packed in the column, dry air at room temperature (≈22°C), with a relative humidity reading of less than 3%, is heated to a desired regeneration temperature and passed over the adsorbent column at a flow rate of 24 SLPM. However, in experiments with the desorption temperature listed as 22°C, the dry air at 0-3% RH at 22°C is simply used as the purge gas to regenerate the system, without being heated. The volumetric flow rate is calculated and controlled based on the MFC readings which are converted from mass flow rates to volumetric flow rates by using the density of the gas. The hot air flows over the column until the column reaches thermal and adsorption equilibrium, based on the temperature and humidity readings stabilizing. The column is then isolated from the rest of the system by closing the entrance and exit valves and cools to room temperature overnight.

Once the column reaches thermal equilibrium at room temperature, the airflow is set to 24 SLPM and is sent to the bypass, keeping the column isolated from air and humidity. While the air is flowing through the bypass, the RH is set to the desired value by measuring the humidity at the inlet and manipulating the flow rates of the dry and humid streams. This is done by an automatic control system developed using LabVIEW software. Once the humidity reaches the desired value, the air flow is diverted towards the inactive heater and freshly regenerated column, allowing water vapour adsorption to take place. The adsorption (discharging) proceeds until the column reaches equilibrium at the end of the full breakthrough from the column, where outlet humidity and temperature stay constant. The process is then repeated under the next set of desired operating conditions. The sorbent was replaced every 10-20 experiments, but previous studies have shown that performing multiple adsorption-desorption cycles does not degrade silica gel's energy storage performance [18].

The controlled independent variables in this study were the relative humidity, particle size, regeneration temperature, insulation, and flow rate. The impacts of these variables on system temperature lifts, breakthrough behaviours, ESD, and thermal power are all examined herein. The temperature and concentration breakthrough curves were observed by measuring and recording the RH and temperature at the inlet and the outlet of the column throughout the experiment every 10 seconds. The breakthrough time was defined as the time from the start of the adsorption experiment until the time that relative humidity reading at the outlet of the column reached 1.6% relative humidity. The 95% saturation time was defined as the time that was required for the column outlet humidity to reach 95% of its maximum value. The temperature lifts were calculated by subtracting the inlet and outlet column temperatures. The total energy released ($Q_{adsorption}$) was calculated using equation 3.1, by integrating over the entire course of the experiment, from the start of the adsorption until 100% saturation is reached. To obtain the ESD, $Q_{adsorption}$ was divided by the volume of the column.

$$Q_{adsorption} = \int_0^t \dot{m}_{air} C_{p,air} (T_{out} - T_{in}) dt \tag{3.1}$$

where $Q_{adsorption}$ is the heat released during adsorption (kJ), t is the amount of time the adsorption takes place (min), $m_{air}$is the mass flow rate of the air (kg/min), $C_{p,air}$ is the heat capacity of the humid air (kJ/kg°C), T_{out} is the temperature at the outlet of the column (°C), and T_{in} is the temperature at the inlet of the column (°C).

To calculate the average thermal power, first the energy released was calculated by using the integration in equation 3.1 from the start of the adsorption ($t = 0$) until the time when the system reached the chosen saturation point (e.g. when the outlet humidity reaches 50% or 95% of its maximum value). The average thermal power was calculated using two timescales, from the beginning of the adsorption until the outlet humidity reached 50% and 95% of its maximum value. The energy released in this time interval calculated from equation 3.1, was then divided by the time required to reach that level of saturation, yielding the average thermal power. The maximum thermal power was calculated from experimental data by multiplying the maximum temperature difference by the mass flow rate and specific heat capacity.

3.5 Results and discussion

3.5.1 Effect of particle size and inlet relative humidity

The effect of the inlet relative humidity was studied alongside other variables, to see if there were any confounding effects. Therefore, its effect will be described in this section, along with the effects of particle size. For these tests, the operating conditions can be found in Table 3-2. Additionally, two cases of system thermal insulation were considered: basic insulation and additional insulation. These are described in Table 3-3.

Table 3-2. Experimental conditions that were used while studying the effects of inlet relative humidity and particle size.

Variable	Value
Desorption Temperature (°C)	22, 120
Desorption RH (%)	0-3
Air Purge Flow rate (SLPM)	24

Table 3-3. Details of the basic and additional insulation scenarios.

Scenario	Description
Basic Insulation	Fiberglass insulation on the column
Additional Insulation	Fiberglass insulation and aluminum foil on the column plus aluminum foil on the piping

It was observed that the energy storage density (ESD) increases with relative humidity, as can be seen in Figure 3-2. This increase is almost linear at low relative humidity values, and the slope begins to decrease as relative humidity increases beyond 70%. This is because at when RH levels increase, more water vapour molecules will be adsorbed, and more energy will be released, consequently.

The theoretical energy storage density ($ESD_{theoretical}$) was calculated by using equation 3.2 and plotted in Figure 3-2. This equation is the integral of the heat of adsorption curve in Figure 3-3. The isotherm in Figure 3-4 was used to determine q_{charge} and $q_{discharge}$ values, based on the inlet RH during charging and discharging. Equation 3.2 was integrated from the charging inlet RH (0-3%) to the discharging inlet RH (10-90%). In the experiments the desorption purge gas RH was in the range of 0-3%. Therefore, in

calculations, it was assumed that the system was charged at 1.5% RH with 0.9 mol H_2O/kg adsorbed. Equation 3.2 was found to follow the same general trend as the data points in this figure, but it consistently overpredicts the ESD. This is mainly because not all silica gel samples have identical isotherms and heat of adsorption curve shapes. Some variation is expected since this data was taken from literature [21, 27] rather than determined experimentally for the tested sample. Furthermore, heat losses are present in the system during adsorption, decreasing the amount of energy calculated by equation 3.1 and consequently lowering the experimentally measured ESD.

$$ESD_{theoretical} = \rho_{bulk} \int_{q_{charge}}^{q_{discharge}} \Delta H_{ads}(q) dq \tag{3.2}$$

where $ESD_{theoretical}$ is the theoretical energy storage density (kWh/m^3), ρ_{bulk} is the bulk density of the adsorbent in the column (kg/m^3), $q_{dischage}$ is the amount of water vapour adsorbed at equilibrium under the adsorption conditions (mol/kg), q_{charge} is amount of water vapour adsorbed at equilibrium under the desorption conditions (mol/kg), and $\Delta H_{ads}(q)$ is the heat of adsorption as a function of the amount of water vapour adsorbed (kWh/mol).

Particle size showed no impact on ESD, as can be observed in Figure 3-2, if the regeneration is carried out at room temperature. This implies that there are no grain-size related mass transfer limitations under these conditions, when the column is regenerated by 0-3% RH purge gas only, without increasing the temperature of the column.

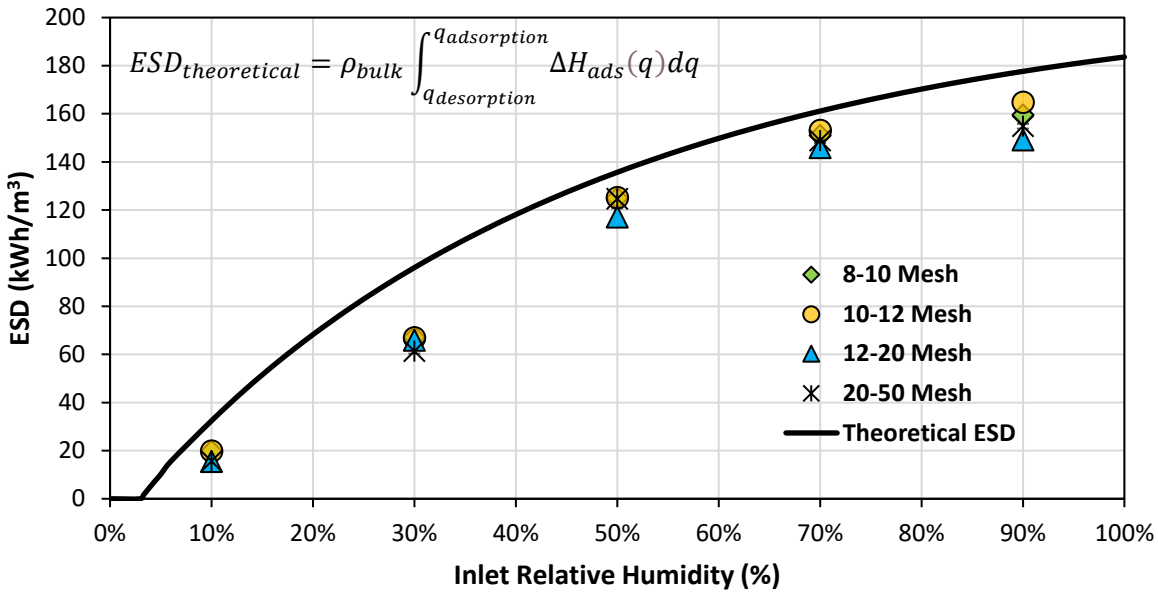

Figure 3-2. Effect of inlet RH and particle size on energy storage density (ESD) with additional insulation, at a flow rate of 24 SLPM, with desorption carried out at room temperature by purging with air of 0-3% relative humidity. The theoretical ESD was plotted based on isotherms and heat of adsorption data from literature [21, 27]. Note that some markers are hidden behind other ones and that there are error bars based on repeat runs for the 50% relative humidity 12-20 mesh data point, but they are hidden by the marker.

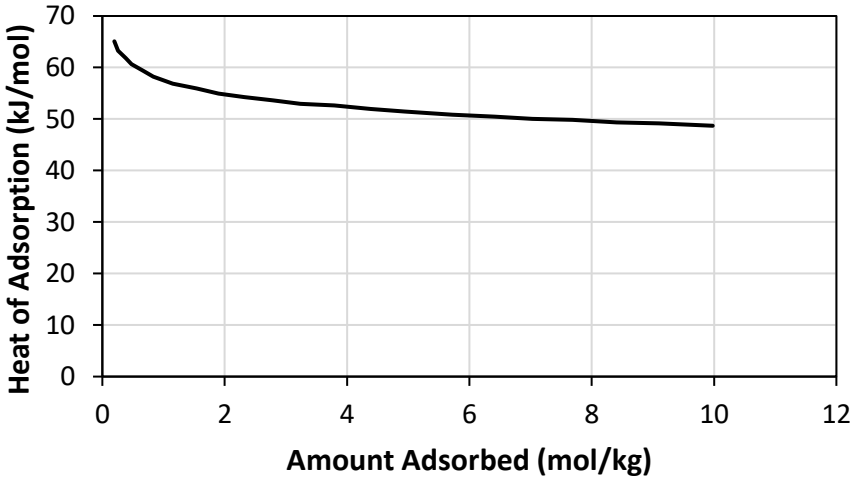

Figure 3-3. The effect of the amount of water vapour adsorbed on the heat of adsorption of a silica gel sample. Data was obtained from Ambrożek, *et al*, 2012 [27].

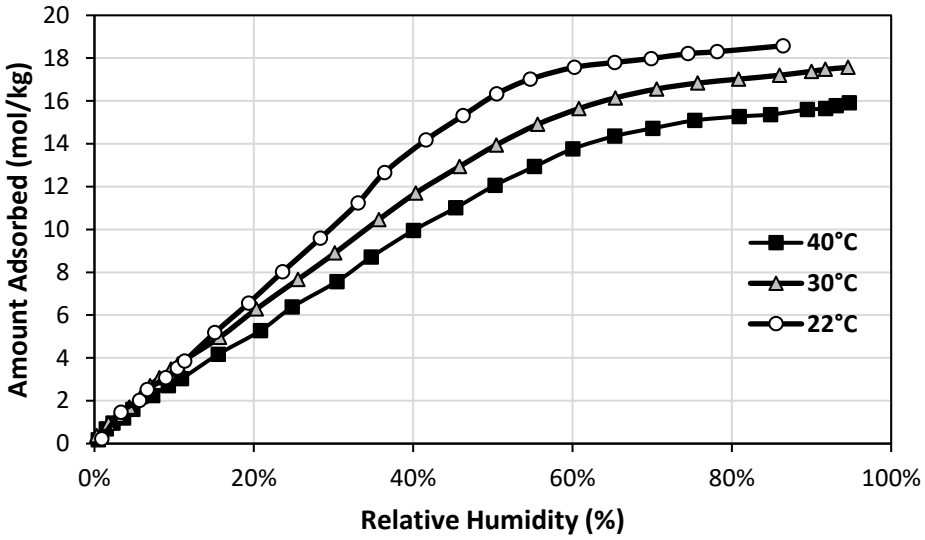

Figure 3-4. A typical water vapour adsorption isotherm for silica gel at different adsorption temperatures. Data was obtained from Oh, *et al*., 2017 [21]. A cubic spline was used to fit the data.

The effect of particle size was also studied when the regeneration temperature was 120°C and the results are summarized in Figure 3-5. It was observed that the ESD increased slightly with increasing particle size, this is potentially due to increased heat transfer rates at lower particle sizes, resulting in greater heat losses to the surrounding. It should also be noted that the bulk density, which was measured using a scale and a graduated cylinder, ranged from 737 kg/m^3 to 803 kg/m^3 (Figure 3-6) would theoretically account for less than 9 % variation in ESD.

It can also be seen in Figure 3-5 that the ESD increases as the relative humidity increases. This is observed, since at high relative humidity levels, the silica gel has a higher water adsorption equilibrium capacity and therefore adsorbs a greater amount of water and releases more energy. The same trend was also observed in Figure 3-2.

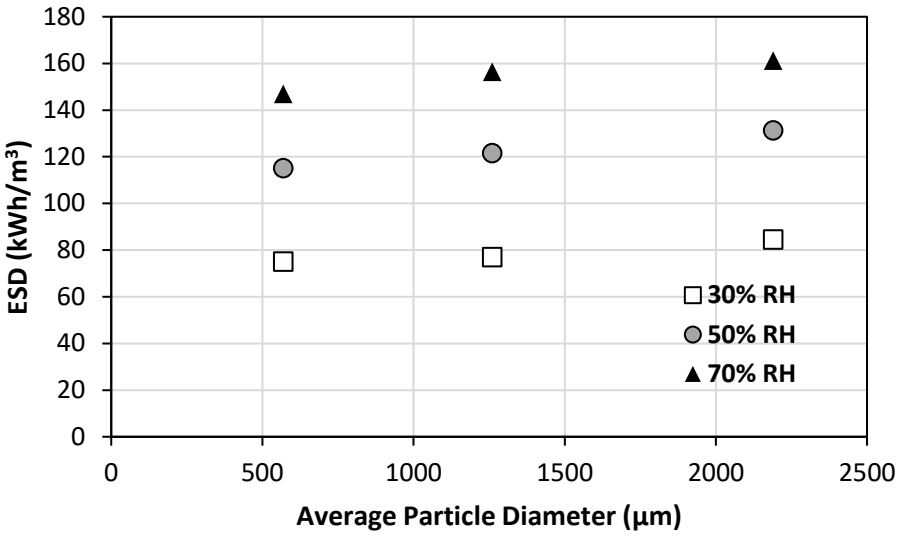

Figure 3-5. Effect of inlet RH and particle size on energy storage density (ESD) after a regeneration temperature of 120°C with basic insulation. The flow rate is 24 SLPM and the arithmetic mean particle diameter is based on the mesh sizes used to sieve the particles.

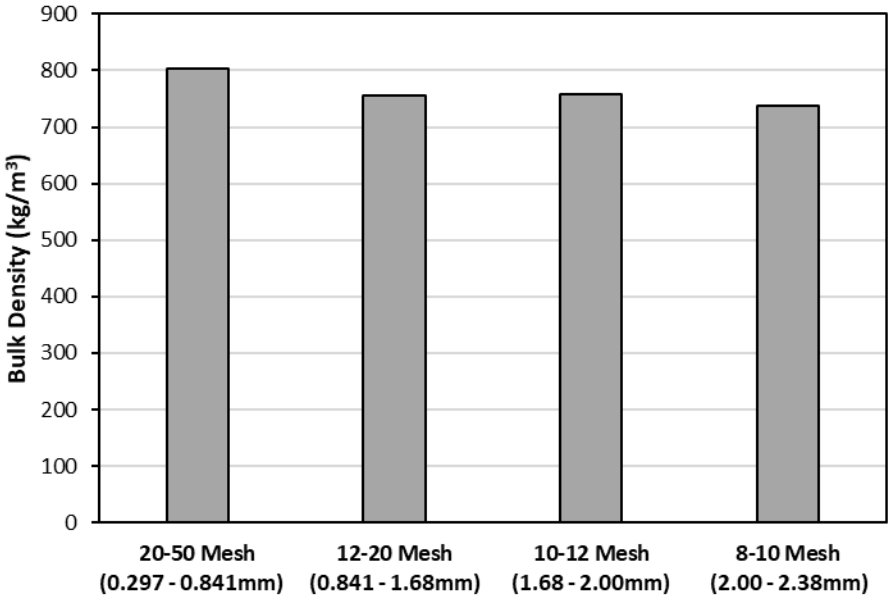

Figure 3-6. Bulk density of the different particle sizes. These values were measured using a graduated cylinder and an analytical scale.

For all experiments, a pure thermal front (PTF) was observed (Figure 3-7), with temperature front detaching from the concentration front and moving ahead of it. The temperature at the exit of the column changes almost immediately, whereas the concentration changes take longer to reach the column exit

[28]. Additionally, there is a discrepancy between the inlet and the outlet relative humidity values at the end of the experiment due to the system pressure drop. This is further discussed in section 3.5.3.

The maximum system temperature lifts increased approximately linearly with the increase in RH and saw no effect from changing particle size as can be seen in Figure 3-8. A theoretical equation was proposed by Basmadjian [28] to model the maximum temperature rise in a packed column with a PTF (equation 3.3), which was derived from a simple energy balance at equilibrium. Since $\frac{C_{p,s}}{C_{p,g}} \ll \frac{q}{Y_f}$, this equation can be practically simplified to equation 3.4. This inequality holds true under all of the experimental conditions used in this study. Using average values for heat capacity and heat of adsorption, equation 3.4 has been plotted as a dotted line in Figure 3-8.

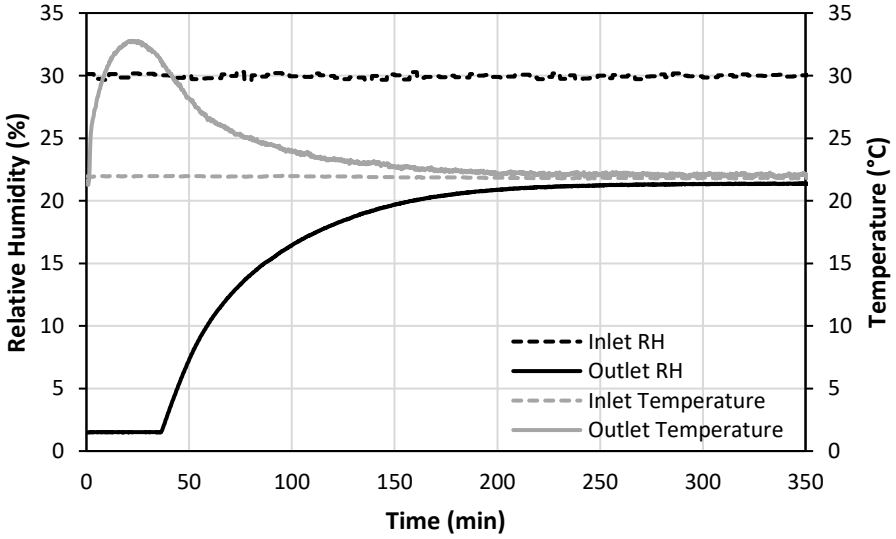

Figure 3-7. Temperature and concentration breakthrough curves for 30% inlet relative humidity, additional insulation, and a 12-20 mesh size after 60°C regeneration temperature. The discrepancy between the inlet and outlet RH is discussed in section 3.5.3.

$$T_{max} - T_{in} = \frac{\frac{q\Delta H_{ads}}{C_{p,g}}}{\frac{q}{Y_f} - \frac{C_{p,s}}{C_{p,g}}} \tag{3.3}$$

$$T_{max} - T_{in} = \frac{Y_f \Delta H_{ads}}{C_{p,g}} \tag{3.4}$$

where T_{max} is the highest observed outlet temperature during the adsorption, T_{in} is the temperature at the inlet of the adsorption column, q is the amount of water vapour adsorbed, ΔH_{ads} is the heat of adsorption, $C_{p,g}$ is the heat capacity of the humid air, $C_{p,s}$ is the heat capacity of the adsorbent, and Y_f is the mole fraction of water vapour present in the air.

A linear relationship was observed, despite eq. 3.4 not being a linear equation, with respect to RH, since both C_p and ΔH_{ads} change non-linearly with respect to RH. This is because the ratio of $\frac{\Delta H_{ads}}{C_{p,g}}$ is nearly constant, even though the heat of adsorption and heat capacity both change with increasing RH [27]-[29]. Furthermore, changing particle size should have no effect on the maximum temperature lift according to eq. 3.4 and this was supported by the results in Figure 3-8. This is because the particle size would primarily affect the heat capacity of the solid, $C_{p,s}$, which has been removed from the equation due to the

$\frac{C_{p,s}}{C_{p,g}} \ll \frac{q}{Y_f}$ assumption.

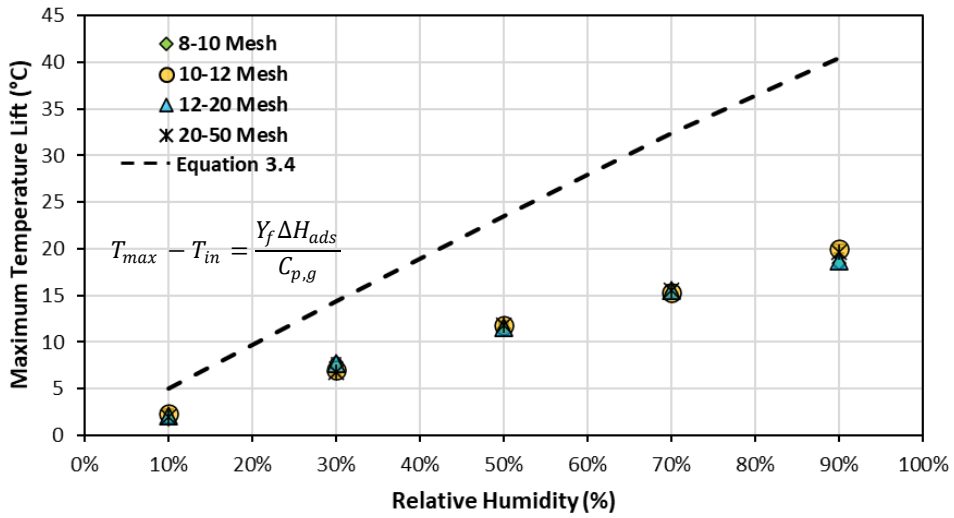

Figure 3-8. Effect of inlet RH and particle size on maximum temperature lift at a flow rate of 24 SLPM while using additional insulation, after desorption using air at room temperature and 0-3% relative humidity as a purge gas. A simplified model (equation 3.4) is plotted as a dashed line along with experimental data points. Note that some markers are hidden by others. The 50% relative humidity, 12-20 mesh run was repeated, but the error bars are hidden by its marker.

As can be seen from Figure 3-8, only about 50% of the expected maximum temperature lift was observed in experimental data. This would be due to factors like heat loss and the effects of the temperature increase on adsorption, which this model does not account for. These effects become even more difficult to overcome at higher temperatures, since there are greater heat losses due to a larger driving force and since the equilibrium adsorption capacity of silica gel decreases at higher temperatures (Figure 3-4). Therefore, it would be beneficial to run the system isothermally, rather than adiabatically, to allow maximum energy extraction. Alternatively, if this technology is being used for space heating, placing the apparatus inside a space that needs to be heated would allow for the heat lost to surroundings not to be wasted.

Figure 3-9 shows the 95 % saturation time as a function of RH for different particle sizes. It appears that this saturation time shows an increase with RH until the RH at around 50%, then it decreases as humidity increases. This would be due to two mechanisms competing, namely the equilibrium adsorption capacity and the mass transfer driving force. As the RH is increased, both of these parameters increase [21, 30]. Increasing the adsorption capacity increases the saturation time, since there is a greater amount of material to be adsorbed. Conversely, an increase in the driving force improves kinetic performance, decreasing the saturation time, because it increases the rate of mass transfer and consequently the slope of the breakthrough curve. The effect of RH on the slope of the breakthrough curves can be seen in Figure

3-10. Therefore, increasing the inlet RH increases the saturation time until 50% RH, due to increases in adsorption capacity. But at higher RH levels, the effects of increased driving force overcome the effects of increased capacity, resulting in a maximum saturation time of around 200 min at an inlet RH of 50%.

Saturation time also showed a slight decrease with decreasing particle size (Figure 3-9) (keep in mind that the higher the mesh size numbers, smaller the particle size). This is likely due to lower mass transfer resistance at lower particle sizes. This is an effect predicted by many mathematical adsorption models [31, 32]. The saturation time could also have been impacted by the particle size distribution, since this has the potential to affect variables like the void fraction and mass transfer resistance in a packed column [33].

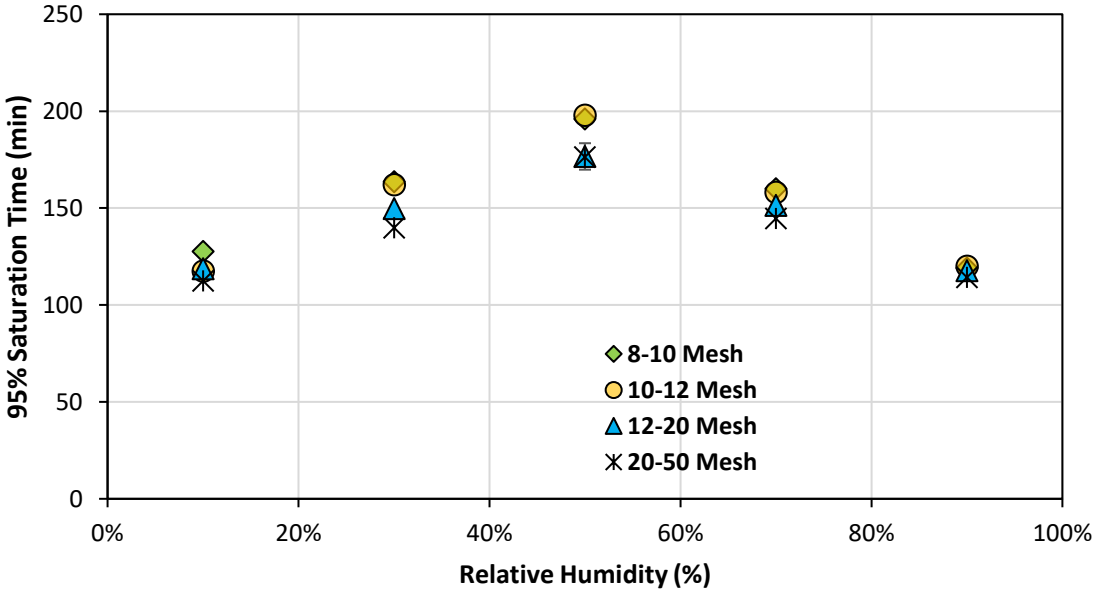

Figure 3-9. Effect of inlet RH and particle size on the time it takes for the column to reach 95% saturation. All experiments were run with additional insulation at a flow rate of 24 SLPM. The desorption carried out at room temperature by purging with air of 0-3% relative humidity. Note that some markers are hidden behind others and error bars are only shown on the 12-20 mesh data point at 50% relative humidity, based on repeated experiments.

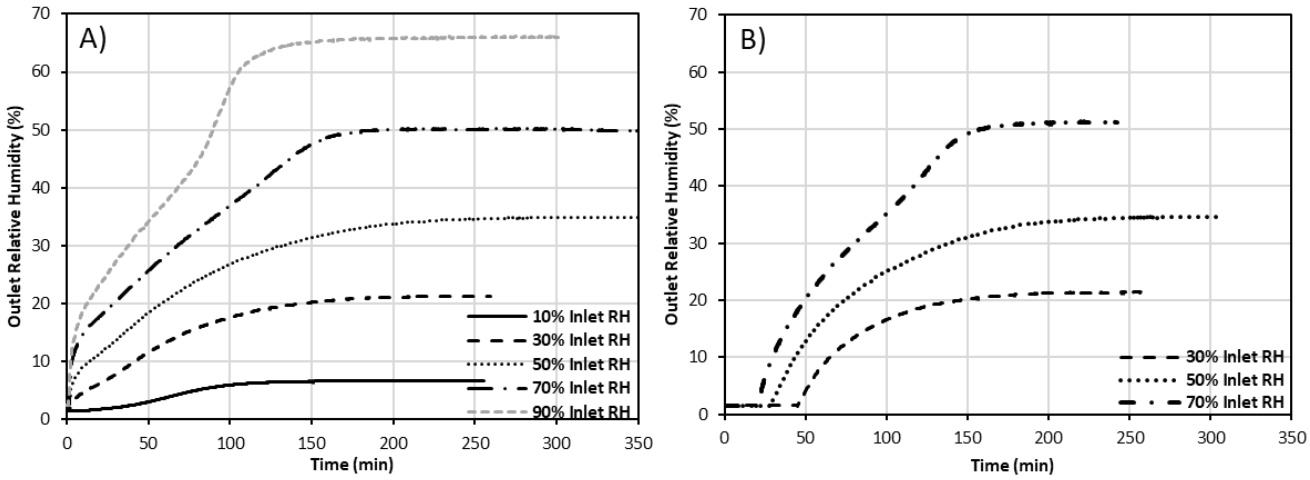

Figure 3-10. Effect of inlet relative humidity on breakthrough behaviour for 12-20 mesh size particles at a 24 SLPM flow rate with additional insulation.
A) After desorption performed at room temperature (22°C) by purging with air with 0-3 % relative humidity
B) After desorption performed at 120°C with air with 0-3 % relative humidity.

As mentioned in section 3.4.2, the average thermal power was calculated over two different timescales: the time required for the column outlet humidity to reach 95% and 50% of its maximum value. The maximum thermal power was calculated by simply multiplying the maximum temperature difference by the mass flow rate and the specific heat capacity of the gas. These three thermal power values were plotted in Figure 3-11 as a function of inlet RH for different particle sizes to illustrate the different thermal powers observed, due to the tailing observed in the temperature and concentration breakthrough curves (Figure 3-7).

None of the three thermal powers show a strong dependence on particle size, but they did show a positive linear trend as the inlet RH increased from 10 to 90% RH (Figure 3-11). From 10% to 50% inlet RH, this linear trend is explained by the fact that both the saturation time and the energy released are increasing linearly (Figure 3-2 & Figure 3-9). However, at inlet RH higher than 70% there is a lesser increase in energy released with increasing humidity (as can be seen in Figure 3-2), but also a decrease in saturation time (as can be seen in Figure 3-9). These two effects appear to offset each other, continuing the linear trend at higher inlet RH values.

The average thermal power when the outlet humidity reaches 95% of its maximum is observed to be only 50% of the maximum thermal power (Figure 3-11). Conversely, the average thermal power when the

outlet humidity reaches 50% of its maximum value is closer to 80% of the maximum thermal power. This is because the temperature profile has a very long tail with low temperature lifts towards the end of the experiment as can be observed from Figure 3-7.

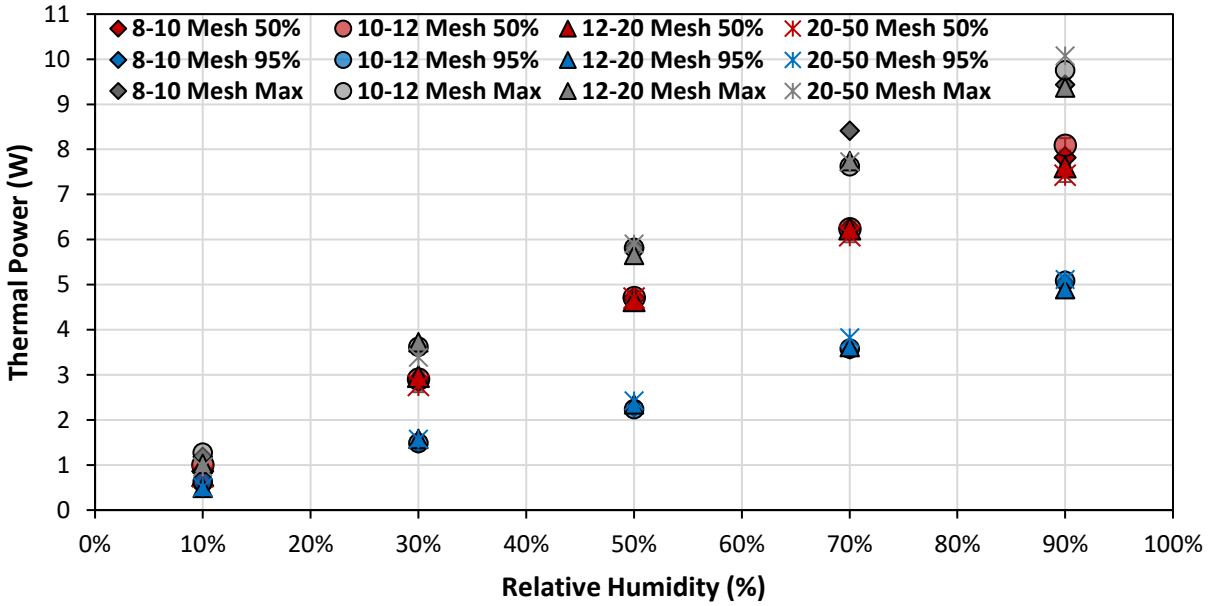

Figure 3-11. Effect of inlet RH and particle size on average and maximum thermal power. Average thermal powers (blue and red) were calculated based on the time until the column outlet RH reaches 95% or 50% of its maximum value. Maximum thermal powers (grey) were calculated by multiplying the maximum temperature lift by the mass flow rate and heat capacity (see section 3.4.2 for details). Desorption was performed at room temperature by purging with air with 0-3% relative humidity; the flow rate was 24 SLPM. These experiments were all performed with additional insulation. Some markers are hidden by other markers. The error bars on the 12-20 mesh trial at 50% relative humidity are based on repeated experiments, but they are hidden.

The pressure drop from the dry and wet stream mixing point to the exhaust of the system was measured using an analog Swagelok pressure gauge from Weston Valve Fittings Ltd. (Mississauga, ON, Canada). The piping and valves contributed greatly to the pressure drop in the system. At a flow rate of 24 SLPM, the valves, piping, and column caused a pressure drop of 35-50 kPa, depending on the particle size as can be seen in Figure 3-12, as observed by the inlet pressure gauge seen in Figure 3-1. Pressure drop was found to increase with decreasing particle size. This is consistent with what is predicted by the Ergun equation for a packed column, since smaller particles lead to higher pressure drops [34].

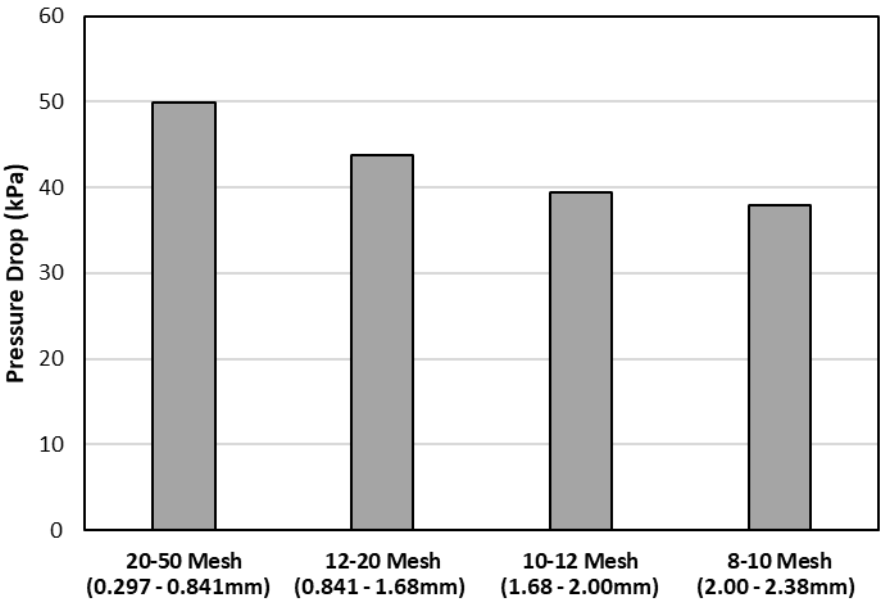

Figure 3-12. Effect of particle size on pressure drop at an inlet relative humidity of 50% and a flow rate of 24 SLPM.

3.5.2 Effect of regeneration temperature

In this section, the same operating conditions that are found in Table 3-2 were used, except that the particle size was held constant at 12-20 mesh and the regeneration temperature was varied. As stated before, when desorption temperature is reported to be 22°C, desorption was carried out using air at a relative humidity of 0-3% as a purge gas, without it being heated up.

Increasing the regeneration temperature of the silica gel increased the ESD and maximum temperature lift as can be seen in Figure 3-13 & Figure 3-14. This increase happens since more water vapour can be desorbed at higher regeneration temperatures, increasing the number of active adsorption sites available. This increases the total amount of water vapour adsorbed, and therefore the amount of energy released during the experiment. For regeneration temperatures above 120°C, little to no difference in energy storage density was observed, since practically all of the active sites are vacant when silica gel is regenerated at 120°C.

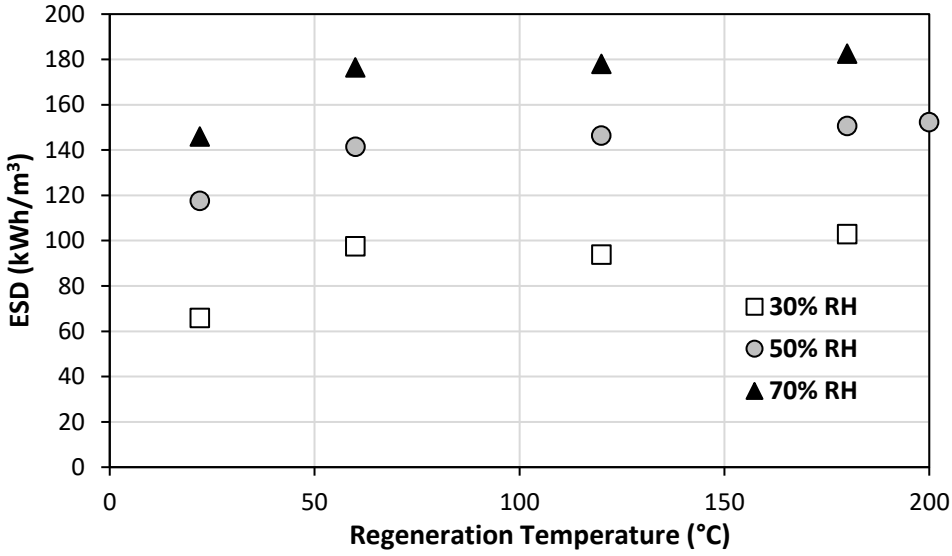

Figure 3-13. Effect of regeneration temperature and inlet relative humidity (RH) on energy storage density (ESD). The flow rate is 24 SLPM and particle sizes are 12-20 mesh. Additional insulation was used. Note that there are error bars on the room temperature desorption for 50% inlet relative humidity, based on repeat runs, but they are hidden by the marker.

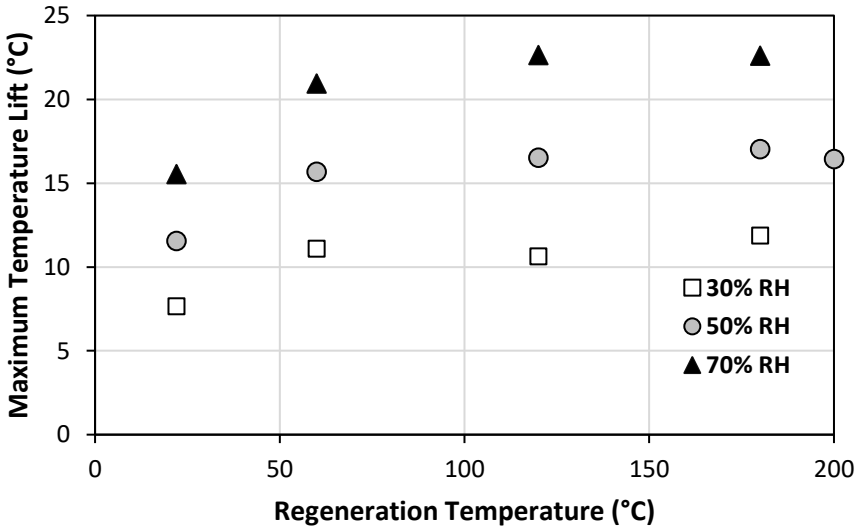

Figure 3-14. Effect of regeneration temperature and inlet relative humidity (RH) on maximum temperature lift. The flow rate is 24 SLPM and particle sizes are 12-20 mesh. Additional insulation was used. Note that there are error bars for the room temperature regeneration data with 50% RH, based on repeat runs, but they are hidden by the marker.

The sample experienced a slight discoloration after attempting a regeneration at 200°C as can be seen in Figure 3-15. The material closest to the inlet of the column, where the highest temperatures were observed during regeneration, was the most discoloured. The discoloration is thought to be related to material degradation, since silica gel is known to degrade at temperatures above 180°C [35]. The discoloration had a rusty hue.

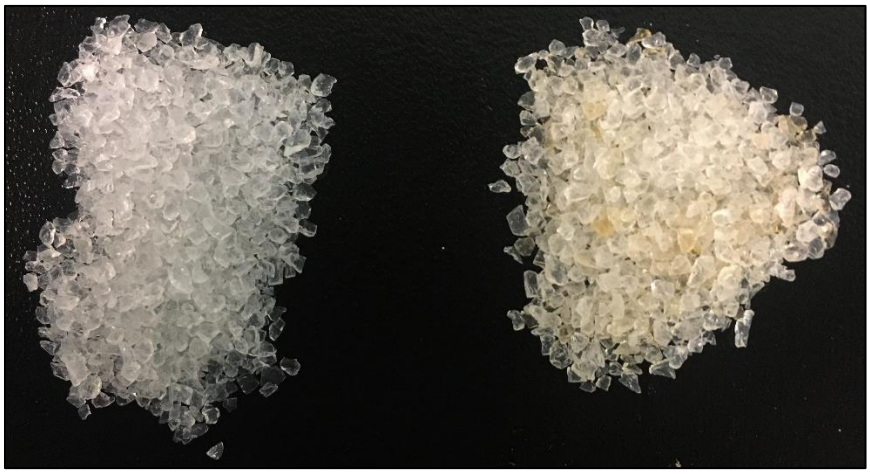

Figure 3-15. Silica gel colour before (left) and after (right) regeneration at 200°C. After regeneration above 200°C, the silica gel showed a yellowish discoloration.

As was mentioned in section 3.5.1, experiments with 12-20 mesh particles were run at 30, 50, and 70% inlet RH, with basic insulation. Both of the basic and additional insulation set-ups had fiberglass insulation on the column, however, the additional insulation scenario also had aluminum foil on the column and on the piping surrounding the column (Table 3-3). By covering the column and piping with aluminum foil, small stagnant air pockets within the foil surround the column and piping. These air pockets act as an insulator because stagnant air exhibits low thermal conductivity.

The set-up with aluminum foil on the piping and column showed higher ESD values by about 17% (Figure 3-16). This is likely because there is less heat being lost to the surroundings. This theory is further supported by the fact that the system with only basic insulation showed lower temperature lifts (25% lower) than the additional insulation set-up that had aluminum foil covering the column and the piping (Figure 3-17).

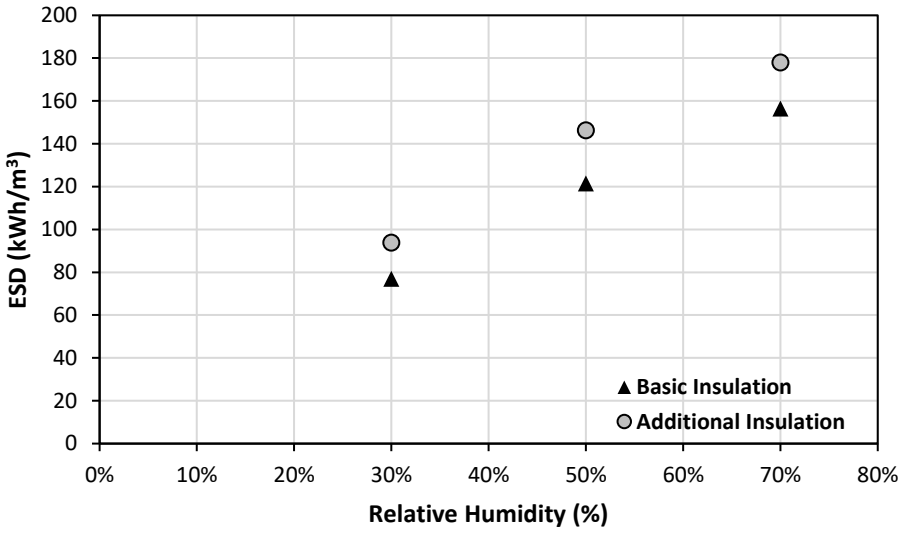

Figure 3-16. The effect of insulation on the column and piping, and the effect of inlet relative humidity on ESD. See Table 3-3 for definitions of the basic and additional insulation scenarios. The regeneration was performed at 120°C and the flow rate was 24 SLPM.

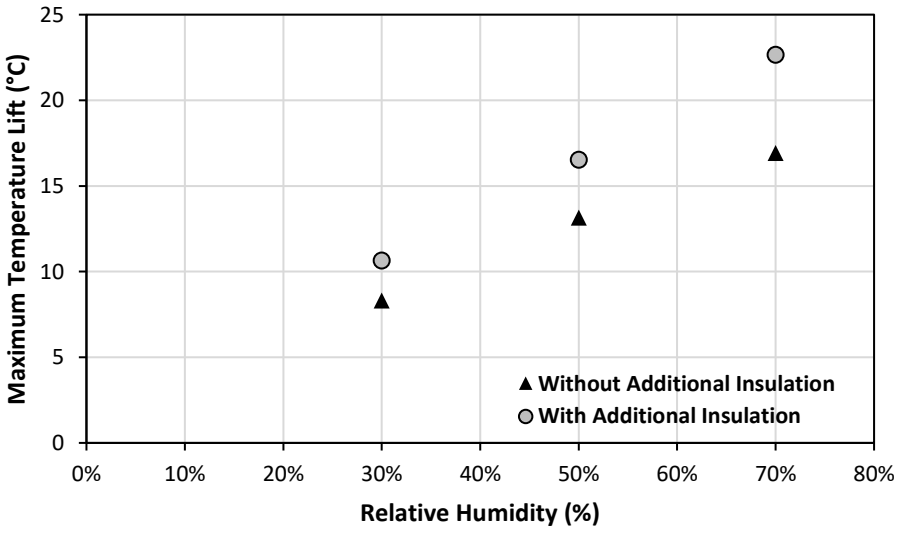

Figure 3-17. The effect of insulation of the column and piping, and the effect of inlet relative humidity on maximum temperature lift. See Table 3-3 for definitions of the basic and additional insulation scenarios. The regeneration was performed at 120°C and the flow rate was 24 SLPM.

The breakthrough time was defined as the time that passed before the outlet relative humidity reading reached 1.6 % RH. The breakthrough time increased as the regeneration temperature increased, and as the inlet RH decreased as can be seen in Figure 3-18. The breakthroughs happened almost immediately when no heat was applied during desorption and only air at room temperature at 0-3% relative humidity

was used as a purge gas. This is likely because the column was not fully regenerated just with purge and there were far fewer available adsorption sites during these adsorption experiments. The differences in breakthrough times above a regeneration temperature of 120°C were minimal.

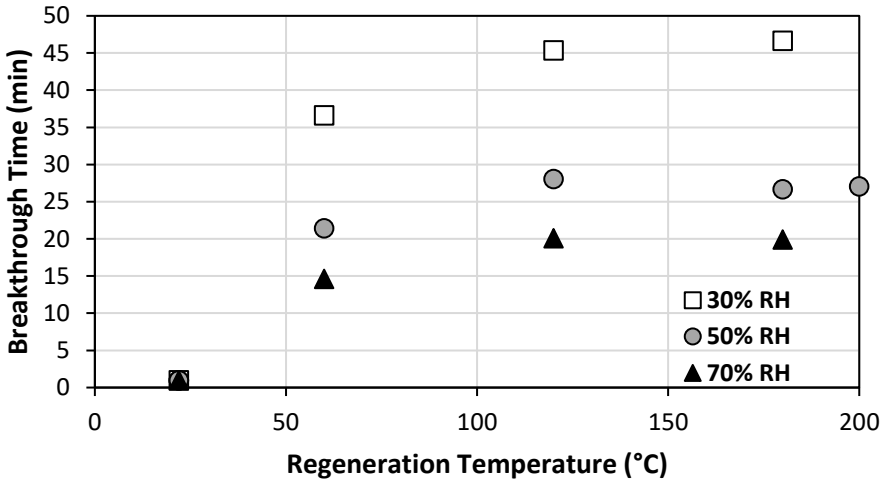

Figure 3-18. Effect of regeneration temperature and inlet relative humidity (RH) on breakthrough time when using additional insulation. The breakthrough time for room temperature desorption with air of 0-3% RH was almost immediate for every adsorption humidity level tested.

3.5.3 Effect of flow rate and pressure

The pressure and flowrate could not be manipulated independently without system modification, so the two variables were analysed simultaneously. The pressure at the inlet of the column was equal to the sum of the atmospheric pressure and the pressure drop, since the exhaust pressure was fixed at atmospheric. The pressure drop was measured right after the first hygrometer at the inlet of the column (Figure 3-1) by subtracting the atmospheric pressure from the gauge pressure reading. The pressure drop through the system, from the inlet humidity probe to system exhaust (Figure 3-1), was plotted as a function of the flow rate for the 12-20 mesh particles in Figure 3-19. A direct quadratic relationship between the pressure drop and the flow rate was observed, regardless of the relative humidity. Note that using an assumed sphericity of 1.0 and a void fraction of 0.4, the pressure drop through the column is predicted by the Ergun equation to be less than 1 kPa through the column [34]. However, this is an oversimplification since the particles were crushed and highly irregular. This still implies that the pressure drop through the system piping has much greater contribution than that of the column to the overall pressure drop from the inlet RH probe to the system exhaust.

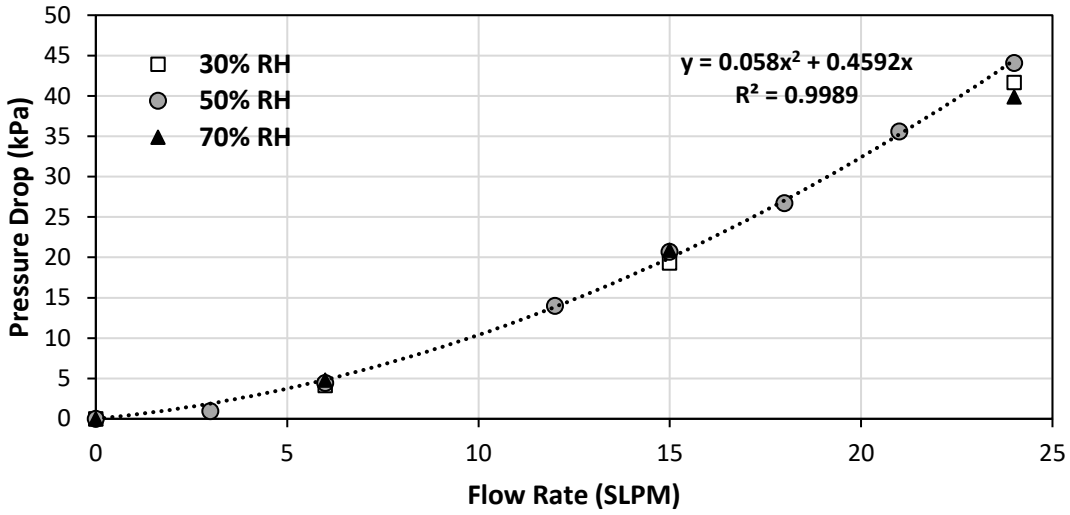

Figure 3-19. Effect of flow rate and inlet relative humidity on pressure drop. The particle size is 12-20 mesh. A quadratic relationship was fit to the data. Note that some data points are hidden by others.

The outlet pressure of the system remains constant at lab atmospheric pressure. Therefore, as the pressure drop in the system increases, the inlet pressure increases proportionally. This difference in total pressure also directly affects the partial pressure of water vapour in the system [36]. This connotes that when there is no adsorption taking place (e.g. after the column is saturated), the RH measured at the inlet of the column will be different from the RH at the outlet, following the relationship observed in equation 3.5. This can be derived using the ideal gas law, because when adsorption is not taking place, the temperature, the number of moles of water vapour, and the volumetric flow rate are supposed to be equal at the two humidity sensors. Therefore, the RH will be proportional to the total pressure. However, the absolute humidity will remain constant, regardless of pressure. This was observed experimentally and can be seen in Figure 3-20.

$$RH_{out} = RH_{in} * \left(\frac{P_{outlet}}{P_{inlet}}\right) \tag{3.5}$$

where RH_{out} is the observed humidity at the outlet of the column when the adsorbent is saturated with water vapour (%), RH_{in} is the relative humidity reading at the inlet of the column, P_{outlet} is the total pressure at the outlet of the column (kPa), and P_{inlet} is the total pressure at the inlet of the column (kPa).

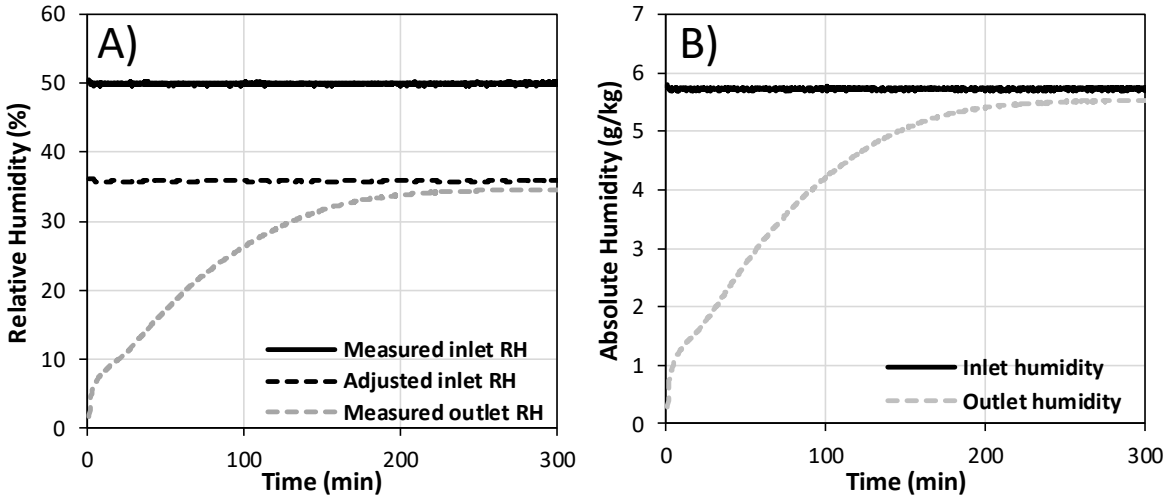

Figure 3-20. Inlet and outlet humidity readings during adsorption breakthrough. The flow rate was 24 SLPM, the particle size was 12-20 mesh, and the desorption was done at room temperature using air with 0-3% relative humidity as a purge gas and additional insulation was used.

A) The measured inlet and outlet RH readings plotted with the adjusted RH reading (Equation 3.5)
B) The calculated absolute humidity readings at the inlet and outlet of the column, based on the total pressure, temperature, and relative humidity reading.

In Figure 3-20A, the measured outlet RH reaches a maximum of 36% RH once the column become saturated, rather than converging with the inlet reading at 50% RH. This discrepancy is explained by the 39 kPa pressure drop that was observed during this trial. The increased pressure drop increases the inlet pressure which increases the RH, according to equation 3.5 (Figure 3-20A). However, the absolute humidity is not affected by pressure and therefore once the column reaches saturation, the inlet and outlet absolute humidity are both approximately at 5.75 g/kg (Figure 3-20B). This phenomenon has also been observed in other non-isobaric energy storage systems [13].

Due to the constraints of the set-up, the pressure and flow rate were manipulated simultaneously. For simplicity, the results will be presented in terms of the flow rate. It was found that the simultaneous manipulation of pressure and flow rate significantly impacted the maximum temperature lifts, the saturation times, the energy storage densities, and the thermal power (Figure 3-21 to 3-23).

As the flow rate increases, so does the energy storage density, until it appears to either level off or decrease at higher flow rates as can be seen in Figure 3-21. The system flow rate could not be increased beyond 24 SLPM, but based on previous results with a similar system, it is expected that there would be an optimal flow rate, above which the energy density would begin to decrease [37]. This is likely due to a trade-off between increased velocity and decreased residence time. A higher velocity will result in higher mass transfer coefficients, leading to faster kinetics for mass transfer, but also leading to more heat losses, as heat transfer coefficient increases at higher fluid velocities. Decreasing the residence time at higher flowrates also decreases the amount of time for sorbent to interact with the surface, decreasing the energy storage density.

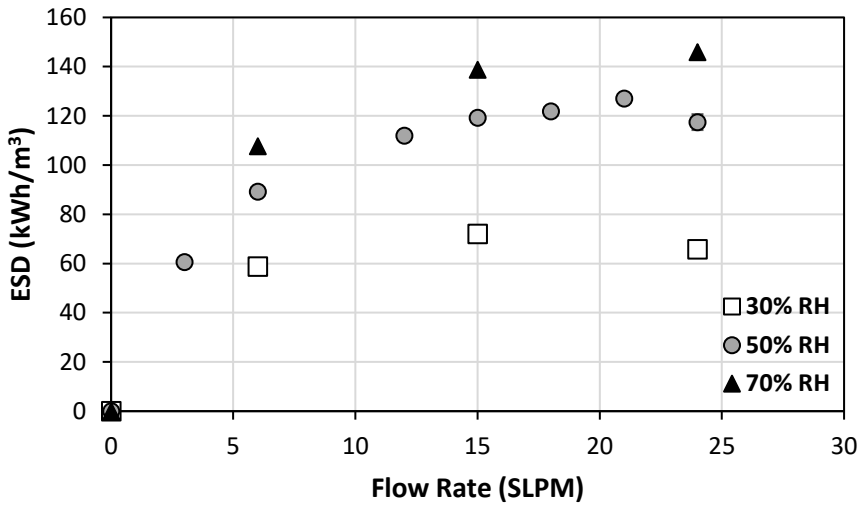

Figure 3-21. Effect of flow rate and inlet relative humidity (RH) on energy storage density (ESD). Desorption performed at room temperature by purging with air at 0-3% relative humidity, the mesh size is 12-20, and additional insulation was used. Error bars were calculated for the 24 SLPM trial at 50% inlet relative humidity, based on repeated experiments, but are hidden by the marker.

The maximum temperature lifts follow similar trends to the energy storage density, implying that beyond 15 SLPM the increase in flow rate does not greatly impact the maximum temperature lift as can be seen in Figure 3-22. At higher relative humidity values, flow rates higher than 15 SLPM have slight negative effects on maximum temperature lifts.

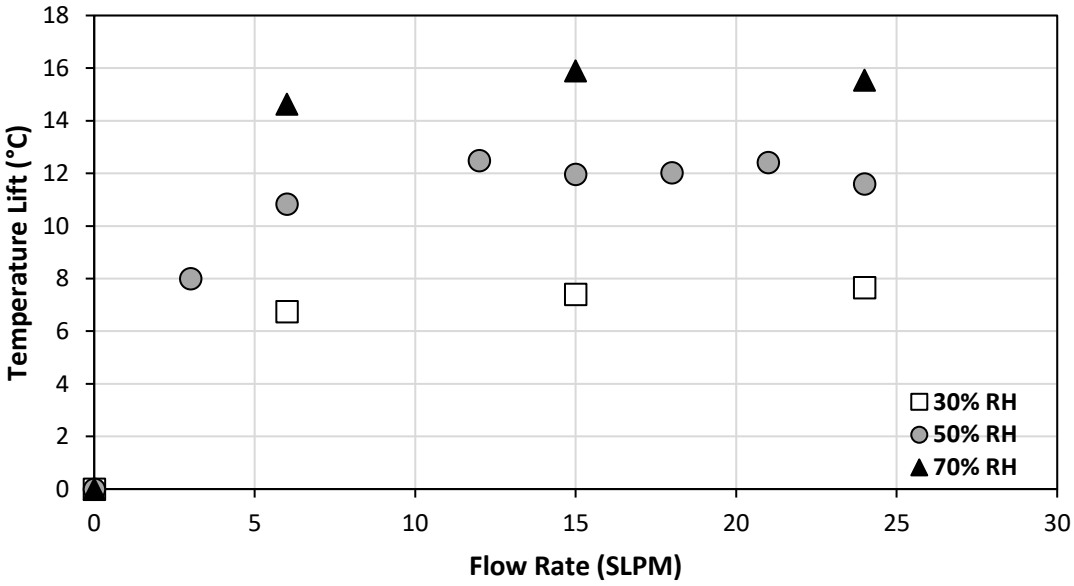

Figure 3-22. Effect of flow rate and inlet relative humidity (RH) on maximum temperature lift. Desorption performed at room temperature by purging with air with 0-3 % relative humidity, the mesh size is 12-20, and additional insulation was used. Error bars were calculated for the 24 SLPM trial at 50% relative humidity, based on repeated experiments, but are hidden by the marker.

The average thermal power shows a strong positive and directly linear correlation with the flow rate as can be observed in Figure 3-23. This is because the flow rate controls the rate at which the sorbate is delivered to the sorbent. In both Figure 3-11 and Figure 3-23, the average thermal power values when the outlet humidity is at 95% and 50% of its maximum value were approximately 50% and 80% of the maximum thermal power values, respectively. A positive correlation between relative humidity and thermal power was observed in both figures.

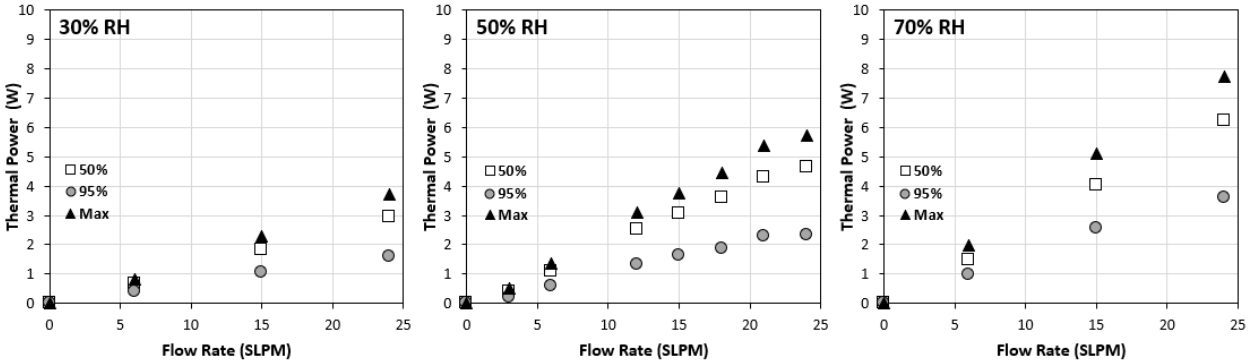

Figure 3-23. Effect of flow rate and inlet RH on thermal power. Average thermal powers (circles and squares) were calculated based on the energy released until the column outlet RH reaches 95% or 50% of its maximum value. Maximum thermal powers (triangles) were the product of the maximum temperature lift, the mass flowrate, and heat capacity (see section 3.4.2). Desorption was performed at room temperature by purging with air with 0-3 % RH; additional insulation was used. The error bars on the trial at 50% RH and 24 SLPM are based on repeated experiments, but they are hidden by the marker.

The 95 % saturation time was observed to be inversely proportional to the flow rate (Figure 3-24). Many equations have been proposed to explain breakthrough behaviours, many of which support the observed relationship that breakthrough and saturation times are inversely proportional to fluid velocity, and therefore, fluid flow rate [32, 38]. A simple two-parameter rational function was fit to the experimental data in Figure 3-24.

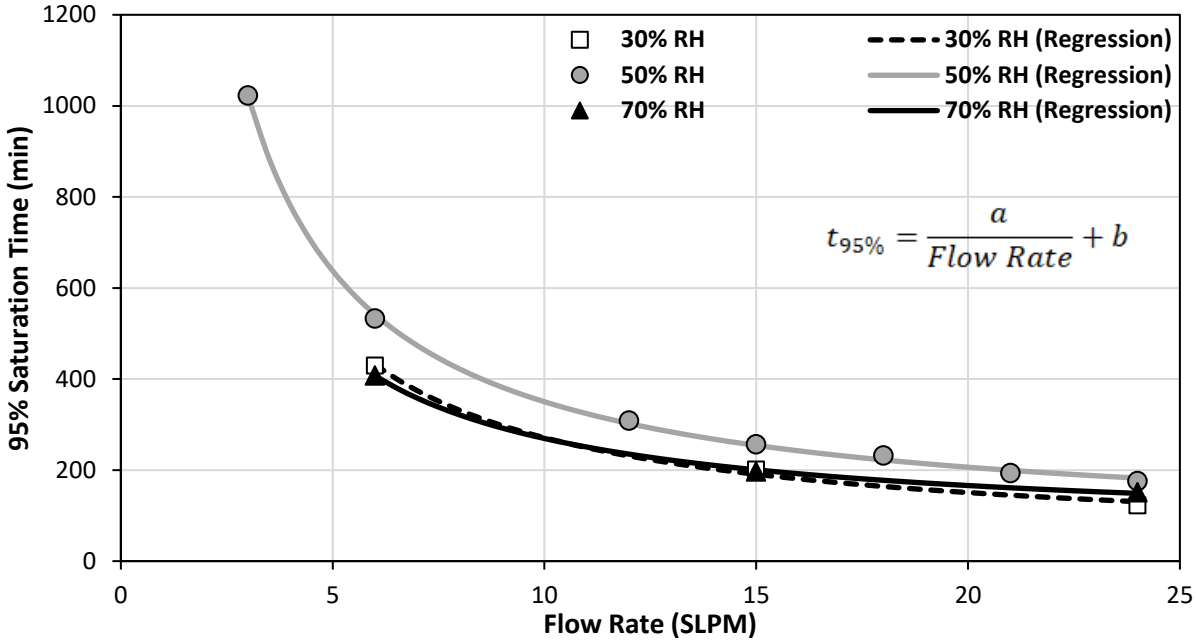

Figure 3-24. Effect of flow rate and inlet relative humidity (RH) on the time that it takes the outlet concentration to reach 95% of its maximum value. Desorption was performed at room temperature by purging with air with 0-3 % relative humidity and particle mesh size is 12-20. Additional insulation was used. Error bars were calculated for the 24 SLPM trial at 50% relative humidity, based on repeated experiments, but are hidden by the marker.

3.6 Conclusions

Key operating parameters were controlled and optimized for an open silica gel/water vapour adsorption-based thermal energy storage system. It was observed that the main effects of particle size were on saturation time and pressure drop with larger particles increasing the saturation time and decreasing the pressure drop. The ESD, maximum temperature lift, and thermal power showed an approximately linear positive trend with increasing inlet RH, essentially following the trend of the silica gel isotherm. The effect of inlet RH on saturation time resulted in a trade-off between driving force and adsorption capacity, resulting in a maximum 95% saturation time of 3.3 hours at about 50% RH, when the desorption was performed at room temperature with air at 0-3% RH used as a purge gas.

Increasing the regeneration temperature from 22°C to 120°C increased the ESD and maximum temperature lifts by approximately 25%, but increasing the regeneration temperature beyond 120°C, showed minimal effects. The breakthrough times also increased with increasing regeneration temperature, but no additional effects were observed above 120°C. It was found that regeneration above 200°C resulted in decolourization of the sorbent.

The inlet pressure and flow rate were manipulated simultaneously in this study. Increasing the flowrate resulted in a linear increase in the thermal power. Increasing the flowrate also increased the ESD and maximum temperature lift, although increasing the flowrate above 15 SLPM had minimal effects. Increasing the flowrate also significantly decreased the column 95 % saturation time, likely due to improved mass transfer.

The conditions chosen to attempt to optimize energy storage density are summarized in Table 3-4. Under these conditions, an energy storage density of 200.7 kWh/m^3 and maximum temperature lift of 28.5°C were obtained. The average and maximum thermal power were 5.9 W (93.9 W/L) and 15.4 W (245.2 W/L). The breakthrough time was 11 min and the 95% saturation time was 126 min. Other researchers have reported silica gel ESD values of 93.6 kWh/m^3 [39] and 123 kWh/m^3 [40]. However, those researchers studied silica gel at lower humidity levels, different desorption temperatures, and different system configurations. This highlights how significantly operating conditions can affect energy storage performance.

Table 3-4. Summary of optimized operating conditions

Variable	Value
Adsorption Relative Humidity	90%
Regeneration Temperature	120°C
Regeneration Relative Humidity	0-3%
Flow Rate	24 SLPM
Particle Size	12-20 mesh

Silica gel has a relatively high energy density, it is inexpensive, and does not require exceptionally high regeneration temperatures. Due to its simplicity, commercial availability, and other favourable properties, it could prove to be useful in demonstrations and pilot scale work. Future studies regarding silica gel-based energy storage systems should consider focussing on reducing heat losses and using salt-in-matrix materials at the bulk scale in order to increase the temperature lifts and energy storage densities. Also, it may be more effective to run the system isothermally, rather than adiabatically, to avoid decreasing the total amount of water that the silica gel can adsorb due to temperature increase. Alternatively, placing the adsorption column in a space that needs to be heated would allow for any lost heat to be captured by the surrounding, increasing the practical energy storage density and system performance.

3.7 References

[1] P. Warneck and J. Hansen, “Global Warming: The Complete Briefing,” *J. Atmos. Chem.*, vol. 30, no. 3, pp. 409–412, 1998.

[2] IEA, “Renewables 2017,” London, England, 2017.

[3] J. K. Fink, *Fuel Cells, Solar Panels, and Storage Devices: Materials and Methods*. John Wiley & Sons, Inc, 2017.

[4] F. Belaïd, “Understanding the spectrum of domestic energy consumption: Empirical evidence from France,” *Energy Policy*, vol. 92, pp. 220–233, 2016.

[5] Natural Resources Canada, “Energy Efficiency Trends in Canada 1990 to 2013,” 2019.

[6] D. Lefebvre and F. H. Tezel, “A review of energy storage technologies with a focus on adsorption thermal energy storage processes for heating applications,” *Renew. Sustain. Energy Rev.*, vol. 67, pp. 116–125, 2017.

[7] T. Wu and C. Lei, “A review of research and development on water wall for building applications,” *Energy Build.*, vol. 112, pp. 198–208, 2016.

[8] P. Tatsidjodoung, N. Le Pierrès, and L. Luo, “A review of potential materials for thermal energy storage in building applications,” *Renew. Sustain. Energy Rev.*, vol. 18, pp. 327–349, 2013.

[9] B. Cárdenas and N. León, “High temperature latent heat thermal energy storage: Phase change materials, design considerations and performance enhancement techniques,” *Renew. Sustain. Energy Rev.*, vol. 27, pp. 724–737, 2013.

[10] Y. Zhang, G. Zhou, K. Lin, Q. Zhang, and H. Di, “Application of latent heat thermal energy storage in buildings: State-of-the-art and outlook,” *Build. Environ.*, vol. 42, no. 6, pp. 2197–2209, 2007.

[11] P. A. J. Donkers, L. C. Sögütoglu, H. P. Huinink, H. R. Fischer, and O. C. G. Adan, “A review of salt hydrates for seasonal heat storage in domestic applications,” *Appl. Energy*, vol. 199, pp. 45–68, 2017.

[12] L. Scapino, H. A. Zondag, J. Van Bael, J. Diriken, and C. C. M. Rindt, “Sorption heat storage for long-term low-temperature applications: A review on the advancements at material and prototype scale,” *Appl. Energy*, vol. 190, pp. 920–948, 2017.

[13] R. van Alebeek, L. Scapino, M. A. J. M. Beving, M. Gaeini, C. C. M. Rindt, and H. A. Zondag, "Investigation of a household-scale open sorption energy storage system based on the zeolite 13X/water reacting pair," *Appl. Therm. Eng.*, vol. 139, no. November 2017, pp. 325–333, 2018.

[14] A. Hauer, "Adsorption system for TES- design and demonstration projects," *NATO Sci. Ser. Therm. Energy Storage Sustain. Energy Consum.*, pp. 409–427, 2007.

[15] Köll, W. van Helden, G. Engel, W. Wagner, B. Dang, J. Jänchen, H. Kerskes, T. Badenhop, T. Herzog, "An experimental investigation of a realistic-scale seasonal solar adsorption storage system for buildings," *Sol. Energy*, vol. 155, pp. 388–397, 2017.

[16] H. Bart and G. Ulrich von, *Ullmann's Encyclopedia of Industrial Chemistry (Adsorption)*, 7th ed. Weinheim, Germany, 2005.

[17] D. Lefebvre, "Thermal Energy Storage Using Adsorption Processes for Solar and Waste Heat Applications: Material Synthesis, Testing and Modeling," 2016.

[18] Y. Hua, A. Godin, and F. H. Tezel, "Water Vapor Adsorption In Silica Gel For Thermal Energy Storage Application," *Adv. Mater. Lett.*, vol. 10, no. 2, pp. 124–127, 2019.

[19] J. Jänchen and H. Stach, "Adsorption properties of porous materials for solar thermal energy storage and heat pump applications," *Energy Procedia*, vol. 30, pp. 289–293, 2012.

[20] T. C. Hui, K. C. Ng, A. Chakraborty, N. M. Oo, and M. A. Othman, "Adsorption characteristics of silica gel/water systems," *J. Chem. Eng. Data*, vol. 47, no. 1177–81, 2002.

[21] H. Oh, S. Lim, J. H. Kim, and C. Lee, "Adsorption Equilibria of Water Vapor on an Alumina/Zeolite 13X Composite and Silica Gel," *J. Chem. Eng. Data*, vol. 62, pp. 804–811, 2017.

[22] E. Courbon, P. D'Ans, A. Permyakova, O. Skrylnyk, M. Steunou, M. Degrez, M. Frère, "A new composite sorbent based on $SrBr_2$ and silica gel for solar energy storage application with high energy storage density and stability," *Appl. Energy*, vol. 190, no. 2017, pp. 1184–1194, 2017.

[23] E. Courbon, P. D'Ans, A. Permyakova, O. Skrylnyk, M. Steunou, M. Degrez, M. Frère, "Further improvement of the synthesis of silica gel and $CaCl_2$ composites: Enhancement of energy storage density and stability over cycles for solar heat storage coupled with space heating applications," *Sol. Energy*, vol. 157, no. September, pp. 532–541, 2017.

[24] O. Skrylnyk, E. Courbon, N. Heymans, M. Frère, J. Bougard, and G. Descy, “Performance characterization of salt-in-silica composite materials for seasonal energy storage design,” *J. Energy Storage*, vol. 19, no. August, pp. 320–336, 2018.

[25] D. Zhu, H. Wu, and S. Wang, “Experimental study on composite silica gel supported $CaCl_2$ sorbent for low grade heat storage,” *Int. J. Therm. Sci.*, vol. 45, no. 8, pp. 804–813, 2006.

[26] N. Yu, R. Z. Wang, Z. S. Lu, and L. W. Wang, “Development and characterization of silica gel-LiCl composite sorbents for thermal energy storage,” *Chem. Eng. Sci.*, vol. 111, pp. 73–84, 2014.

[27] B. Ambrożek, K. Zwarycz-Makles, and W. Szaflik, “Adsorbent-Adsorbate Pairs Used in Adsorption Heat Pumps,” *Pol. Energ. słoneczna*, vol. 1–4, pp. 5–11, 2012.

[28] D. Basmadjian, *The Little Adsorption Book*. Taylor & Francis, 1997.

[29] M. Boukhriss, K. Zhani, and R. Ghribi, “Study of thermophysical properties of a solar desalination system using solar energy,” *Desalin. Water Treat.*, vol. 51, no. 4–6, pp. 1290–1295, 2013.

[30] D. M. Ruthven, *Principles of Adsorption and Adsorption Process*. Wiley-Interscience, 1984.

[31] R. G. Lee and T. W. Weber, “Isothermal adsorption in fixed beds,” *Can. J. Chem. Eng.*, vol. 47, no. 1, pp. 54–59, 1969.

[32] R. K. C. T.W. Weber, “Pore and Solid Diffusion Models for Fixed-Bed Adsorbers,” *J. AIChE*, vol. 20, no. 2, pp. 228–238, 1974.

[33] M. Suzuki, H. Kada, and M. Hirota, “Effect of size distribution on the relation between coordination number and void fraction of spheres in a randomly packed bed,” *Adv. Powder Technol.*, vol. 10, no. 4, pp. 353–365, 1999.

[34] S. Ergun, “Fluid flow through packed columns,” *Chem. Eng. Prog.*, vol. 48, 1952.

[35] G. M. Neves, R. F. S. Lenza, and W. L. Vasconcelos, “Evaluation of the Influence of Microwaves in the Structure of Silica Gels,” *Mater. Res.*, vol. 5, no. 4, pp. 447–451, 2002.

[36] J. R. Elliott and C. T. Lira, *Introductory Chemical Engineering Thermodynamics*. Upper Saddle River, NJ: Prentice Hall PTR, 1999.

[37] B. Ugur and F. H. Tezel, “Thermal Energy Storage in Adsorbent Beds,” *M.A.Sc. Thesis Univ. Ottawa, Ottawa, Canada*, 2013.

[38] J. B. Rosen, “Kinetics of a Fixed Bed System for Solid Diffusion into Spherical Particles,” *J. Chem. Phys.*, vol. 20, no. 387–394, 1952.

[39] J. Jänchen, D. Ackermann, H. Stach, and W. Brösicke, “Studies of the water adsorption on Zeolites and modified mesoporous materials for seasonal storage of solar heat,” *Sol. Energy*, vol. 76, no. 1–3, pp. 339–344, 2004.

[40] G. Gartler, D. Jähnig, G. Purkarthofer, and W. Wagner, “Development of a high energy density sorption storage system,” in *Proceedings of Eurosun 2004*, 2004.

Chapter 4 - $MgSO_4$-based Composites for Space Heating and Cooling Applications

Suboohi Shervani, University of Ottawa

Curtis Strong, University of Ottawa

F. Handan Tezel, University of Ottawa

Abstract

Thermal energy storage based on sorption is an emerging technology used in space heating and cooling applications. Salt hydrates exhibit high energy density and emerged as promising candidates for long-term energy storage. However, their lack of stability due to agglomeration and deliquescence are the main issues for their long-term use and sustainability. To overcome this, composites based on salt hydrates are being investigated by researchers lately. The current paper focuses on $MgSO_4$ salt hydrate-based hybrids for thermal energy storage, and covers the major concerns pertaining to stability and cyclability of the hybrids. The structural characterization of the hybrids is performed by SEM. The hydration/dehydration characteristics are measured by a lab scale thermal energy storage apparatus. The hybrid shows high energy storage density (139 kWh/m^3) when sorption is performed at 50% inlet relative humidity, at room temperature, after a dehydration temperature of 120°C.

Keywords: Salt Hydrates, Hydration, Thermal Energy Storage, Energy Storage Density, Hybrids, $MgSO_4$, Silica gel

4.1 Nomenclature

$C_{p,air}$	Heat capacity of air (kJ/kg °C)
H	Absolute humidity (kg/kg)
L	Length of the column (cm)
$\dot{m}_{air}$	Mass flow rate of air (g/min)
M_{air}	Molar mass of dry air (kg/kmol)
M_{H2O}	Molar mass of water (kg/kmol)
p_{H2O}^{sat}	Saturation vapour pressure of water (kPa)
P_{tot}	Total pressure (kPa)
$Q_{hydration}$	Energy released during hydration (kJ)
$\dot{Q}_{max}$	Maximum thermal power (W)
R^2	Coefficient of determination (-)
RH	Relative humidity (%)
t	Time (min)
T_{in}	Inlet temperature (°C)
T_{out}	Outlet temperature (°C)
V	Volume (cm^3)
x_{H2O}	Volume mixing ratio (-)

Greek Letters

ΔT_{max}	Maximum temperature difference (°C)
⌀	Diameter (cm)

4.2 Abbreviations

AA	Activated alumina
EDX	Energy dispersive X-ray analysis
ESD	Energy storage density
DI	Deionized
$MgSO_4$	Magnesium sulphate
RH	Relative humidity
SE	Specific energy
SEM	Scanning electron microscope
SG	Silica gel
SLPM	Standard liters per minute

4.3 Introduction

From the recent past, the consumption of fossil fuels has been increased significantly, which emits carbon-dioxide, and causes global warming [1]. So, there is a need for economically viable alternative energy sources with fewer emissions. Renewable thermal energy sources, like solar thermal, are some of the best alternatives to fossil fuels as they are efficient and have low carbon dioxide emissions. However, to fully utilize all of the energy potential from a source with an inconsistent power output, like solar thermal, thermal energy storage technology is required.

Thermal energy storage systems are of three types, (i) sensible heat, (ii) latent heat, and (iii) thermo-chemical energy storage. In sensible energy storage, the storage medium is heated, and energy is stored during the process, however, physical and chemical state of the media remains the same. Latent heat involves a phase change. Finally, thermo-chemical energy storage, involves a reversible chemical reaction or a process. Thermal energy is stored by applying heat to reverse the reaction/process (e.g. dehydration of hygroscopic salts), then the energy is released by allowing the reaction/process to proceed forward (e.g. hydration) [2]. Moreover, the thermo-chemical storage has advantages over the two other methods in terms of absence of toxic materials, no heat losses during storage, and higher energy storage density values [3,4].

Among the water-vapour adsorption-based thermo-chemical energy storage materials, nanostructures have shown excellent thermal storage properties due to their high surface area, pore size and pore volume [5]. Metal organic frameworks are different class of adsorbent materials which have considerable high surface area and pore volume and exhibit high thermal energy storage properties [6]. Elsayed *et al*. have studied the thermal energy storage properties of CPO-27 (Ni). The water uptake capacity was measured at 470 g/kg and energy storage density was found to be 170 Wh/kg at 100°C charging temperature [1]. Similarly, zeolites are highly microporous structures and demonstrate reasonably high energy storage properties [7]. Hauer has installed energy storage with 7000 kg of 13X in a school building in Munich. The storage was charged from the heat during off-peak hours at dehydration temperatures of 130-180°C and a total energy storage density of 200 kWh/m^3 was achieved [8]. Similarly, Dawoud *et al*., have taken 13X-water hydration modules for heat pump. The adsorber/desorber contained 13.2 kg of 13X and the measured maximum energy density increased from 144 to 165 kWh/m^3 as the flow rate in the adsorber increased from 0.5 to 2 L min-1 [9]. Hybrid structures emerged as novel structures that display wide range of improved thermal energy properties due to inclusion of constituents [10]. Dicaire and Tezel have tested activated alumina/13X composite to study their thermal storage properties. The composite exhibited the highest energy density of 200 kWh/m^3at 8 L/min flow-rate and 100% relative humidity (RH) at atmospheric pressure and ambient temperature at the inlet [11].

Another type of composites with high energy storage density values, are salt-in-matrix composites. Salt hydrates demonstrate high energy storage density [12] and incorporation of these salt hydrates can increase the sorption capacity of host porous matrixes [13]. Xu et *al*. have fabricated $MgSO_4$ impregnated 13X and activated alumina composites and found that at 60% RH the energy storage density was 123.4 kWh/m^3 and 82.6 kWh/m^3, respectively. They demonstrated that the impregnated $MgSO_4$ improves the overall TES performances of both zeolite 13X and activated alumina host materials. The impregnation has also increased the kinetics of the composites. The temperature lifts of activated alumina/$MgSO_4$ and 13X/$MgSO_4$ were 69.2°C and 16.7°C, respectively [14]. Similarly, Hongois *et al*., have developed a $MgSO_4$/13X composite by impregnation method. The $MgSO_4$ was confined in the microporous structure of the zeolite 13X pellets with an optimum percentage of $MgSO_4$ of 15% wt. With an airflow rate of 8 L/min and an inlet air at 50% RH, an energy density of 180 Wh/kg (166 kWh/m^3) was obtained [15]. Similarly, Korhammer *et al*., have synthesized $CaCl_2$-molten salt hydrate-graphite composite, which had 610 g/kg of water uptake capacity and 148 kJ/mol of enthalpy of hydration. The incorporation of graphite has increased the stability and thermal conductivity and the water sorption performance [16]. Zhang *et*

al. have fabricated activated alumina/LiCl composite and the maximum energy storage density of 191 kWh/m^3 was achieved at input air temperature and relative humidity of 20°C and 80%, respectively [17].

Despite their favorable energy storage properties, the deliquescence relative humidity (DRH) of LiCl and $CaCl_2$ is very low, 11% at 25 °C and 29 % at 30 °C for LiCl and $CaCl_2$, respectively. Conversely, $MgSO_4$ has high DRH value (92% at 25°C). So, for this study the $MgSO_4$ was chosen as a salt to avoid the issues related to deliquescence. Moreover, in comparison to other matrices, silica gel (SG) is inexpensive, commercially available, non-toxic, and exhibits long-term stability [18]. Therefore, in the current study various MgSO4-based hybrids were synthesized and their thermal energy storage properties were explored and compared. However, the study mainly focuses on the synthesis, characterization, and energy storage performance of the best performing hybrid, $MgSO_4$/SG with different $MgSO_4$ concentrations. This paper demonstrates the stability of $MgSO_4$/SG hybrid and optimum concentration of salt hydrate in the hybrid.

4.4 Materials and Methods

Four types of $MgSO_4$-based composites (Table 4-1) have been synthesized via dry impregnation method [19]. Silica gel was provided by Xebec Adsorption, Inc. (Blainville, QC, Canada), activated alumina was provided by Axens Canada (formerly Rio Tinto Alcan) (Brockville, ON, Canada), zeolite 13X was provided by Axens Canada (formerly Rio Tinto Alcan) (Brockville, ON, Canada), polyvinyl alcohol (PVA) and ethanol were purchased from Sigma Aldrich, Canada (Oakville, ON, Canada), and $MgSO_4$ was purchased from ThermoFisher Scientific Canada (Whitby, ON, Canada). The energy storage characteristics of these composites were measured using a lab scale energy storage set-up (section 4.4.5).

Table 4-1. List of $MgSO_4$ based composites with activated alumina and silica gel, together with their corresponding abbreviations used in this document.

Composite	**Abbreviation**
Activated alumina/ $MgSO_4$	AA/ MgSO4
Activated alumina/ $MgSO_4$/ polyvinyl alcohol	AA/ MgSO4/PVA
Activated alumina +silica gel+13 X/ $MgSO_4$	AA+SG+13X/ MgSO4
Silica gel/ 15 g $MgSO_4$	SG/MgSO4-15g

4.4.1 Activated alumina/ $MgSO_4$ synthesis

First, 30 g of activated alumina was kept inside a beaker filled with 100 mL ethanol for half an hour to remove the impurities and contaminations. Activated alumina was then extracted from ethanol via filtration. 15 g of $MgSO_4$ and 30 g of activated alumina were mixed together in 100 mL deionized (DI) water and stirred for 24 h. The mixture was then dried for 6 h at 120°C in an oven.

4.4.2 Activated alumina/ $MgSO_4$/ polyvinyl alcohol synthesis

First, 30 g of activated alumina was kept inside a beaker filled with 100 mL ethanol for half an hour to remove the impurities and contaminations. Activated alumina was then extracted from ethanol via filtration. 15g of $MgSO_4$, 30g of activated alumina, and 5 g of PVA were mixed together in 100 mL deionized (DI) water and stirred for 24 h. The mixture was then dried for 6 h at 120°C in an oven.

4.4.3 Activated alumina + silica gel + 13X/ $MgSO_4$ synthesis

First, 10 g of activated alumina, 10 g of silica gel, and 10 g of zeolite 13X was kept inside a beaker filled with 100 mL ethanol for half an hour to remove the impurities and contaminations. The host materials were then extracted from ethanol via filtration. 15g of $MgSO_4$, 10g of activated alumina, 10g of silica gel, and 10g of zeolite 13X were mixed together in 100 mL deionized (DI) water and stirred for 24 h. The mixture was then dried for 6 h at 120°C in an oven.

4.4.4 Silica gel/$MgSO_4$ synthesis

First, 30 g of silica gel was kept inside a beaker filled with 100 mL ethanol for half an hour to remove the impurities and contaminations. Silica gel was then extracted from ethanol via filtration. 15 g of $MgSO_4$ and 30 g of silica gel were mixed together in 100 mL deionized (DI) water and stirred for 24 h. The mixture was then dried for 6 h at 120°C in an oven.

Of the tested composites, the silica gel/ 15 g $MgSO_4$ was found to have the best energy storage performance (see section 4.5.2). Therefore, multiple silica gel/$MgSO_4$ samples were synthesized with various amounts of $MgSO_4$ in order to determine the effects of its $MgSO_4$ concentration in the best performing $MgSO_4$ hybrid. The same synthesis procedure as the silica gel/ 15 g sample was followed except with 10g, 15g, 30g, 45g, 60g, and 120g of $MgSO_4$, rather than 15g. Note that for the 120 g sample, 150 mL of DI water was used, rather than 100 mL. These composites were further characterized by SEM to observe the structural characteristics. A list of the silica gel/$MgSO_4$ composites tested in this study can be found in Table 4-2.

Table 4-2. List of silica gel/ $MgSO_4$ based composites.

Sample Number	Composites	Weight of $MgSO_4$ (g)	Wt. % $MgSO_4$
1	SG_10 gm MgSO4	10	25%
2	SG_15 gm MgSO4	15	33%
3	SG_30 gm MgSO4	30	50%
4	SG_45 gm MgSO4	45	60%
5	SG_60 gm MgSO4	60	67%
6	SG_120 gm MgSO4	120	80%

4.4.5 Energy storage density measuring set-up and methodology

The energy storage performance tests were done using a lab-scale experimental set-up and testing methodology similar to those described by Hua *et al*. [20]. The schematic diagram of the system is provided in Figure 4-1. Approximately 5 g of the sorbent material was crushed and sieved to a 7x20 mesh size (0.841 mm – 2.83 mm). The stainless-steel sorption column (⌀=1.09 cm, L=7.67 cm, V=7.15 cm^3), insulated with fiberglass, was then packed with the sorbent material. Next, air with an RH of less than 3% at 22°C was heated by an electric heater to a dehydration temperature of 120°C and passed over the column at a flow rate of 12 standard liters per minute (SLPM) to dehydrate the sample and store the thermal energy. Once the column effluent RH reading was less than 3% for at least 15 minutes, the dehydration was considered complete. After dehydration, the column was sealed with valves and allowed to cool to room temperature (22°C) overnight.

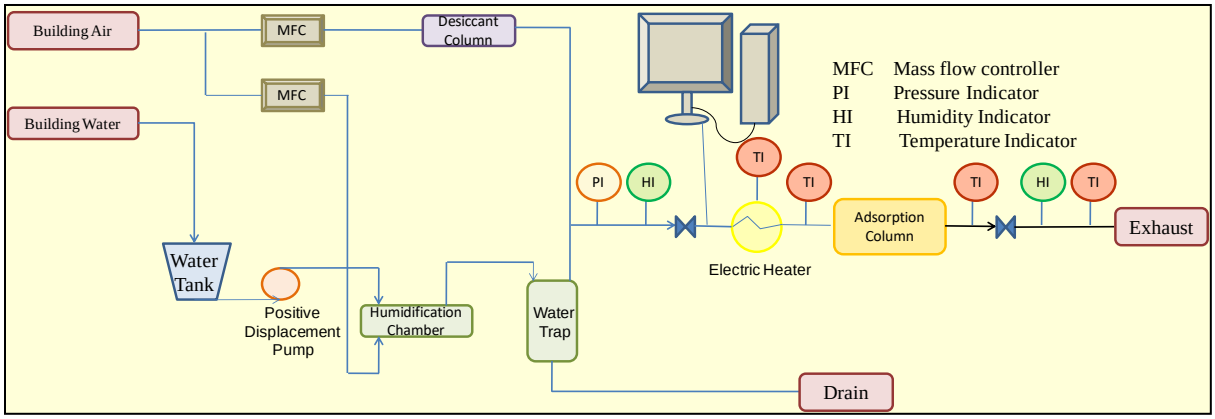

Figure 4-1. Schematic diagram of the lab-scale thermal energy storage set-up used in this study. All measurements were recorded electronically using a LabVIEW program.

For the hydration experiments, dry building air at approximately 22°C was humidified to 50% RH (13 mbar partial pressure of water vapour) and was passed over the column at a flow rate of 12 SLPM. The temperature difference at the inlet and outlet of the column was measured and recorded, as well as the mass flow rate passing over the column. With this information, it was possible to calculate the amount of energy released, $Q_{hydration}$ during hydration using eq. 4.1. Furthermore, the temperature, humidity and flow rates were recorded throughout the experiment so that the breakthrough behavior, thermal power, and temperature profile could also be examined.

$$Q_{hydration} = \int_0^t \dot{m}_{air} C_{p,air} (T_{out} - T_{in}) dt \qquad (4.1)$$

where $Q_{hydration}$ is the heat released during hydration (kJ), t is the amount of time the adsorption takes place (min), m_{air} is the mass flow rate of the air (kg/min), $C_{p,air}$ is the specific heat capacity of the humid air (kJ/kg°C), T_{out} is the temperature at the outlet of the column (°C), and T_{in} is the temperature at the inlet of the column (°C).

By calculating the amount of energy released during hydration, it is possible to calculate important energy storage performance parameters like energy storage density (ESD), specific energy (SE), and thermal power. In this study, ESD was calculated by dividing $Q_{hydration}$ by the volume of the column and specific energy was the quotient of $Q_{hydration}$ and the mass of the dehydrated sample in the sorption column. The maximum thermal power was computed based on the maximum difference between the inlet and outlet temperature of the column during hydration (ΔT_{max}) according to eq. 4.2.

$$\dot{Q}_{max} = \dot{m}_{air} C_{p,air} \Delta T_{max} \quad (4.2)$$

Where $\dot{Q}_{max}$ is the maximum thermal power observed during hydration (W), $\dot{m}_{air}$ is the mass flow rate of air (g/s), $C_{p,air}$ is the specific heat capacity of air (J/g°C), and ΔT_{max} is the maximum observed temperature difference between the inlet temperature and outlet temperature of the column during the hydration experiment (°C).

4.5 Results and Discussions

Structural characterization of the $MgSO_4$ impregnated silica gel composites was performed by scanning electron microscopy (SEM) surface analyzer. Final concentration of the $MgSO_4$ in the composites was calculated through the energy dispersive X-ray analysis (EDX). The charging/discharging characteristics of the composites were measured by a lab scale thermal energy storage set-up.

4.5.1 Scanning Electron Microscopy Analysis

The composites were characterized through JSM-7500F field emission scanning electron microscopy (FE-SEM) of JEOL. Figure 4-2 shows the surface morphology for different amounts of $MgSO_4$ added to the silica gel. It is clear from this figure that as the weight of the $MgSO_4$ increases, more deposition of the salt on the silica gel appeared, as the surface becomes smoother. This also correlates with elemental mapping results in Figure 4-3. The SEM micrographs in Figure 4-2 depict the homogeneous distribution of the $MgSO_4$ over the silica gel. The 120 g $MgSO_4$ sample exhibits more incorporation of salt in the silica gel. Furthermore, it is clear from the micrographs that the size and structure of silica gel is not homogeneous. The particles are of different shapes and sizes; however, the distribution of the salt in the composites is homogeneous. Figure 4-3 represents the elemental mapping of the 120 g and 15 g $MgSO_4$/SG composites. It is clear from this figure that for 120 g $MgSO_4$/SG composite, there is more salt distributed over the silica gel which can be confirmed from the darker elemental colors in Figure 4-3 (b), 3 (c) and 3 (d). Figure 4-3 (a) and Figure 4-3 (f) are the scanning electron microscopy images of the 120 g $MgSO_4$/SG and 15 g $MgSO_4$/SG composites, respectively. The Si content (Figure 4-3 (e)) is less while Mg (Figure 4-3 (b)), S (Figure 4-3 (c)), and O (Figure 4-3 (d)) contents are more for 120 g $MgSO_4$/SG composite. On the other hand, for 15 g $MgSO_4$/SG composite, the Si contents (Figure 4-3 (j)) are more in comparison to Mg (Figure 4-3 (g)), S (Figure 4-3 (h)), O (Figure 4-3 (i)) contents. It means that the salt concentration is less in this composite, which highly agrees with our preparation of the sample.

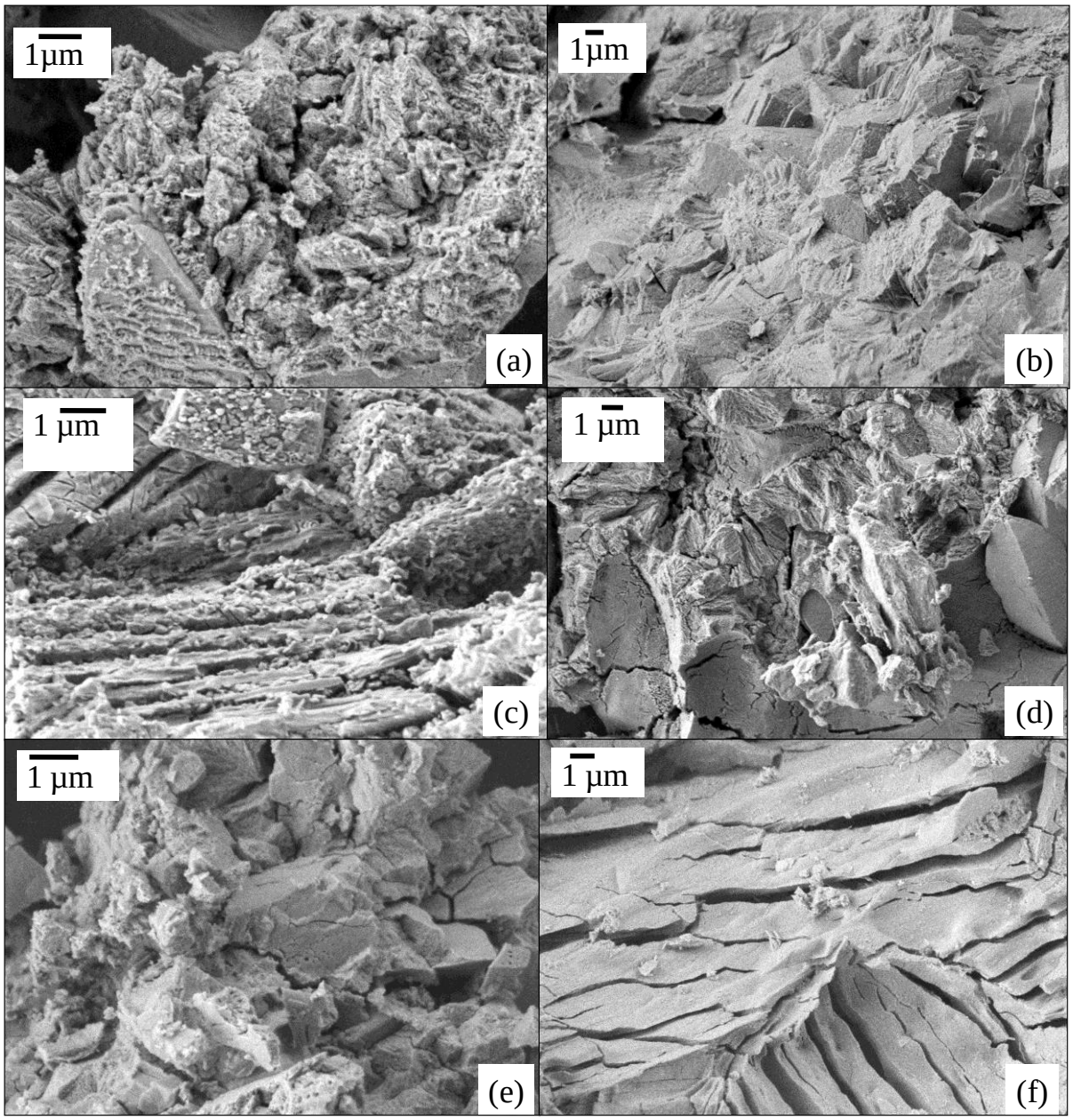

Figure 4-2. Surface morphology of $MgSO_4$ impregnated silica gel composite by Scanning electron microscopy (SEM) with $MgSO_4$ weight,

(a) 10 g, (b) 15 g, (c) 30 g, (d) 45 g, (e) 60 g, and (f) 120 g.

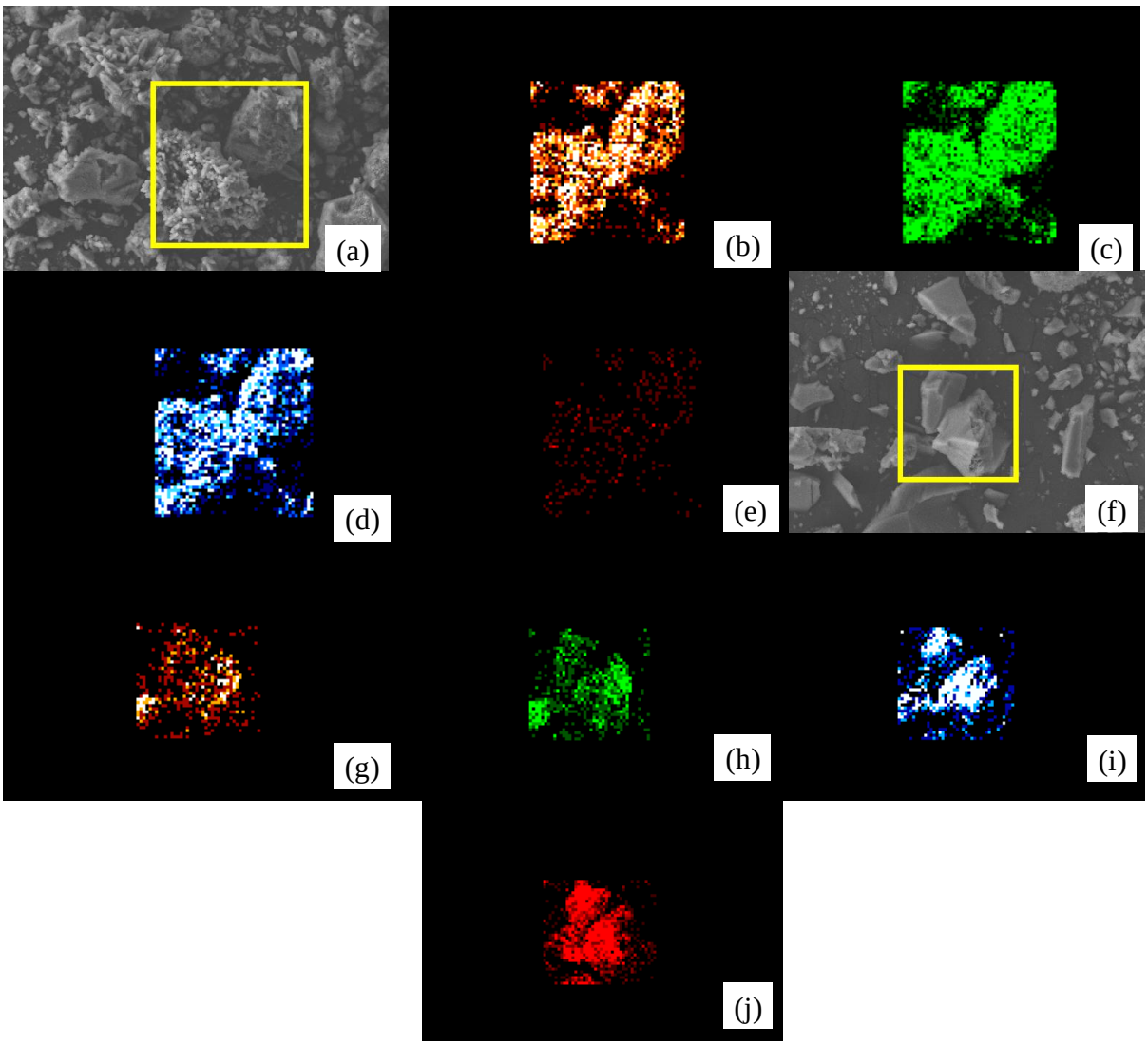

Figure 4-3. The EDX elemental Mapping of 120 g $MgSO_4$/SG composite, and 15 g $MgSO_4$/SG composite.
(a) Scanning electron microscopy (SEM) image of 120 g $MgSO_4$/SG composite
(b) Mg element of the 120 g $MgSO_4$/SG composite
(c) S element of the 120 g $MgSO_4$/SG composite
(d) O element of the 120 g $MgSO_4$/SG composite
(e) Si element of the 120 g $MgSO_4$/SG composite.
(f) SEM image of the 15 g $MgSO_4$/SG composite,
(g) Mg element of 15 g $MgSO_4$/SG composite
(h) S element of 15 g $MgSO_4$/SG composite
(i) O element of 15 g $MgSO_4$/SG composite
(j) Si element of 15 g $MgSO_4$/SG composite.

To investigate the elemental composition, composites were characterized by EDX. The confirmation of the wt. % concentration of the $MgSO_4$ and silica gel in each composite after synthesis is calculated based on the EDX results and the masses used in synthesis and shown in Figure 4-4. Note that these values are not quite in agreement with the wt% values that were calculated using the weights of materials used during synthesis. This is because the EDX measures the concentration on the surface only, implying that there is a large deposition of $MgSO_4$ on the surface of the samples.

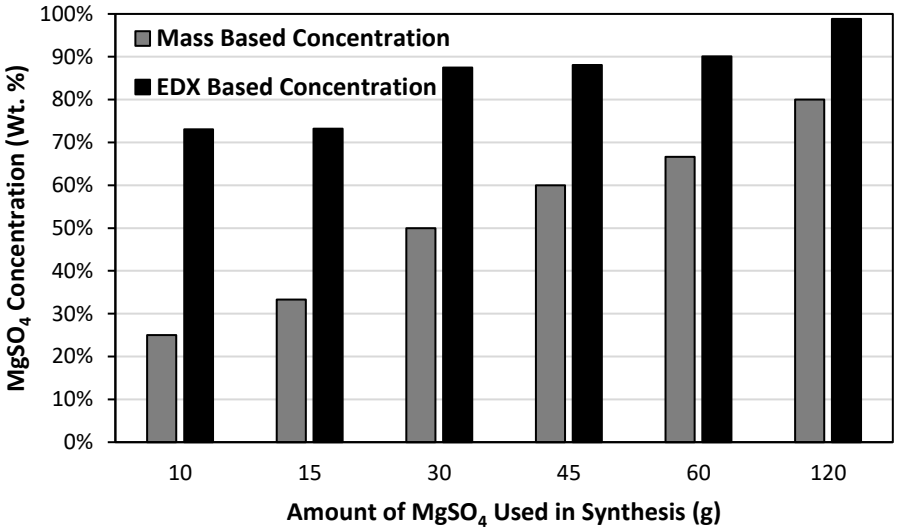

Figure 4-4. The concentration of salt in the $MgSO_4$/SG samples based on the masses used during synthesis and based on the EDX analysis.

4.5.2 Energy storage experiments

Due to the high deliquescence relative humidity of $MgSO_4$ (92% RH at 25°C) [21], it was selected as the hygroscopic salt that was investigated. Several $MgSO_4$ based composites were synthesized and their performances were compared to a standard baseline of pure silica gel. The energy storage density, specific energy and maximum thermal power of these compounds are reported in Figure 4-5 for three consecutive hydration and dehydration cycles. Note that the hydration relative humidity was 50% at room temperature (22°C), dehydration was performed at 120°C, and the flow rate was 12 SLPM during hydration and dehydration.

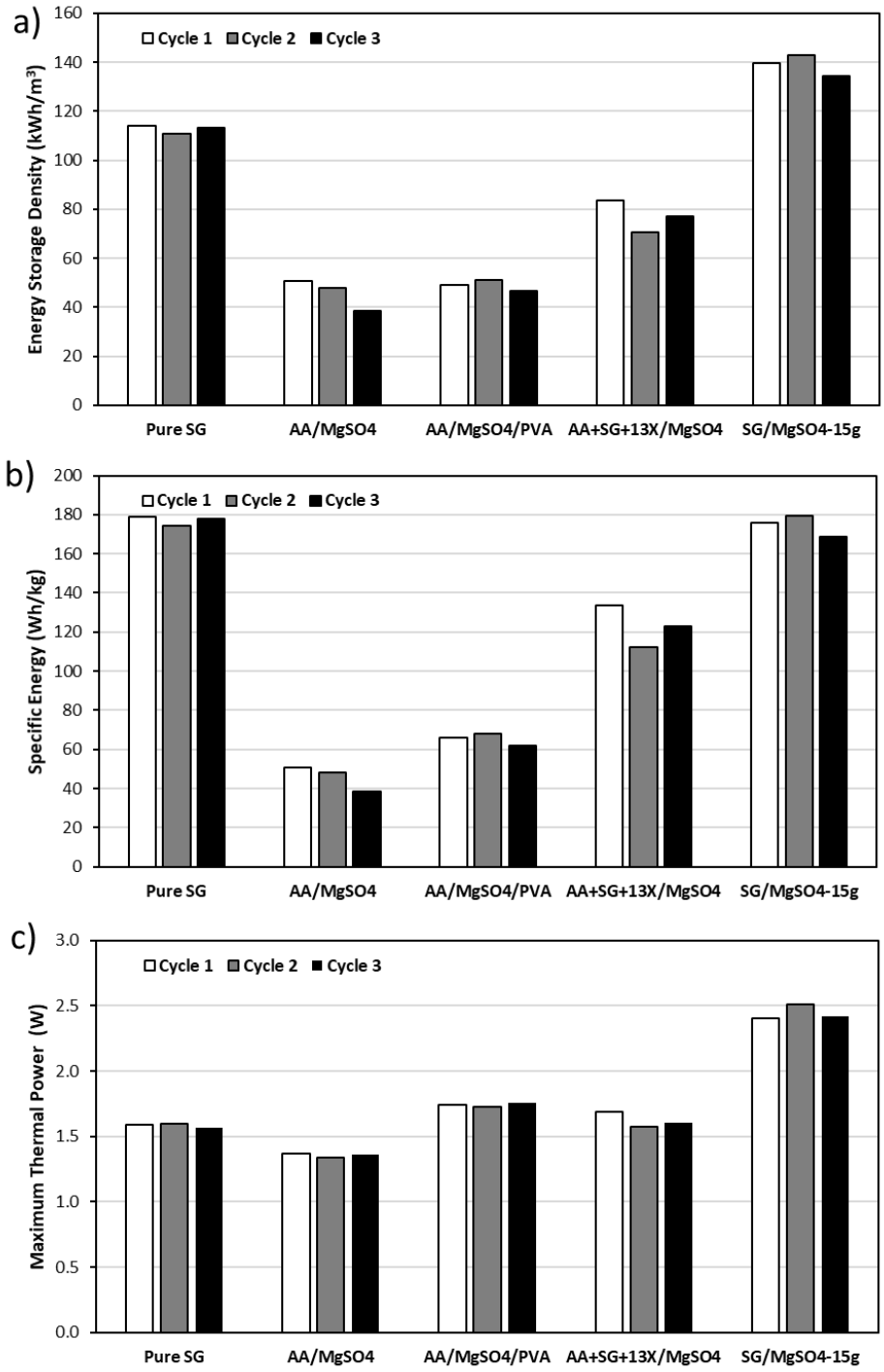

Figure 4-5. The a) energy storage density, b) specific energy, and c) maximum thermal power for four $MgSO_4$ based composites and their comparisons to pure silica gel. Three consecutive hydration and dehydration cycles were performed at a flow rate of 12 SLPM, a hydration relative humidity of 50%, and after a dehydration at 120°C.

All $MgSO_4$ composites showed relatively good cyclic stability after 3 hydration and dehydration cycles under these conditions. This was expected since the hydration humidity was less than the deliquescence relative humidity of $MgSO_4$ (92% RH at 25°C), so the salt should not become deliquescent. The silica gel composite with 15 g of $MgSO_4$ had the highest values for energy storage density, specific energy, and maximum thermal power, compared to the other composites, according to Figure 4-5. Thus, silica gel/$MgSO_4$ composites with different amounts of salt were synthesized and tested in order to quantify and optimize the effects of salt concentration in the adsorbent on energy storage performance.

Six SG/$MgSO_4$ composites synthesized with different amounts of salt, ranging from 10 g to 120 g, were tested in the energy storage apparatus at a hydration inlet RH of 50% at 22°C, after a dehydration at 120°C, and a flow rate of 12 SLPM. The energy storage density, specific energy, and maximum thermal power were calculated for each SG/$MgSO_4$ composite (Figure 4-6).

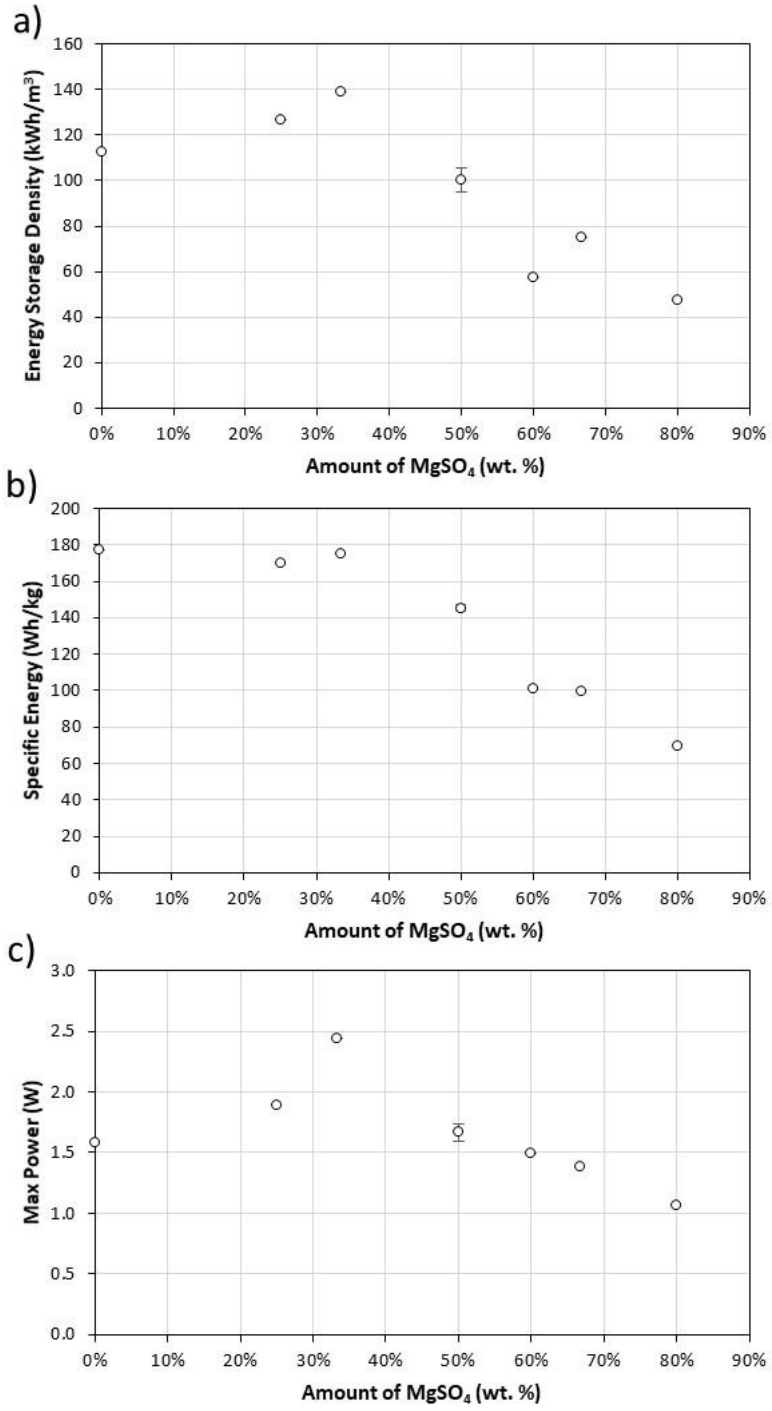

Figure 4-6. The a) energy storage density, b) specific energy, and c) maximum thermal power for pure silica gel (SG) and six SG/$MgSO_4$ composites with various amounts of salt. Hydration was performed at a flow rate of 12 SLPM and 50% inlet relative humidity, after a dehydration at 120°C and a flow rate of 12 SLPM. The weight percent on the x-axis was calculated based on the synthesis masses. The error bars are based on repeated runs with freshly synthesized material. This bar on the 50 wt% run in b) is hidden by its marker.

As the amount of salt is increased, the performance of the system increased first and then started to decrease at higher salt concentrations in the silica gel above 33 wt %, indicating the optimum wt % of the $MgSO_4$ as 33 % (which corresponds to the 15 g $MgSO_4$ addition in Table 4-2). Up to a certain amount of the salt, the performance is increased due to the existing interactions of the salt and the dehydrated silica gel with the water molecules. This could imply that at low salt concentrations the $MgSO_4$ acts as a pump and attracts the water into the silica gel pores, facilitating hydration of both silica gel and the salt, as was observed by Jabbari-Hichri *et al*. [22]. However, this can also be explained by the differences in bulk density between the samples (Figure 4-7), since the ESD is simply the product of the specific energy and the bulk density.

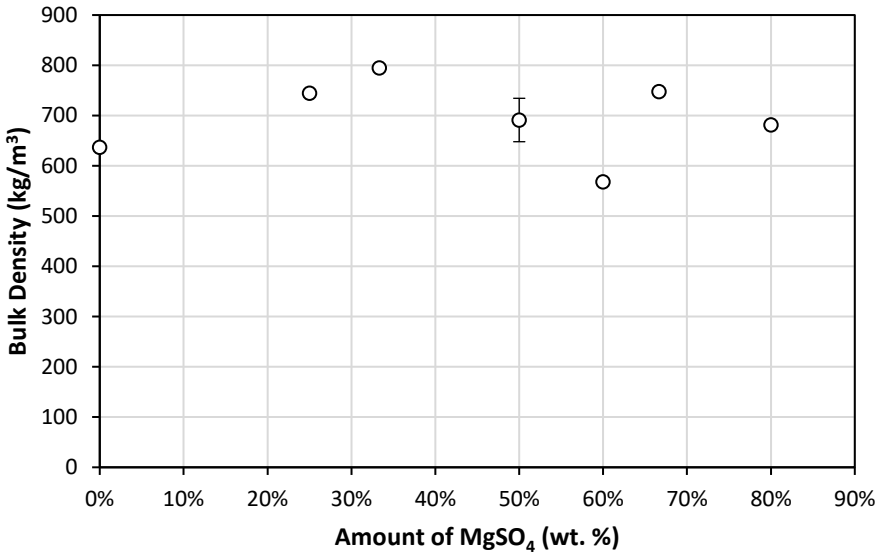

Figure 4-7. Bulk density of all $MgSO_4$/SG composites and pure SG. They were calculated by dividing the mass of the sample in the column by the volume of the column. The weight percent on the x-axis was calculated based on the synthesis masses.

By adding more salt to the composite, the silica gel host performance is decreased due to a reduction in number of active sites that are being occupied by the salt. This is essentially blocking the higher specific energy silica gel sites [23], in order to increase the amount of $MgSO_4$, which has a lower specific energy than pure silica gel. This ultimately reduces the performance of the material.

In addition to the energy storage performance parameters, it is also useful to examine the breakthrough behavior of the composites with different salt concentrations. The resulting absolute humidity breakthrough curves can be seen in Figure 4-8 for different SG- $MgSO_4$ composites.

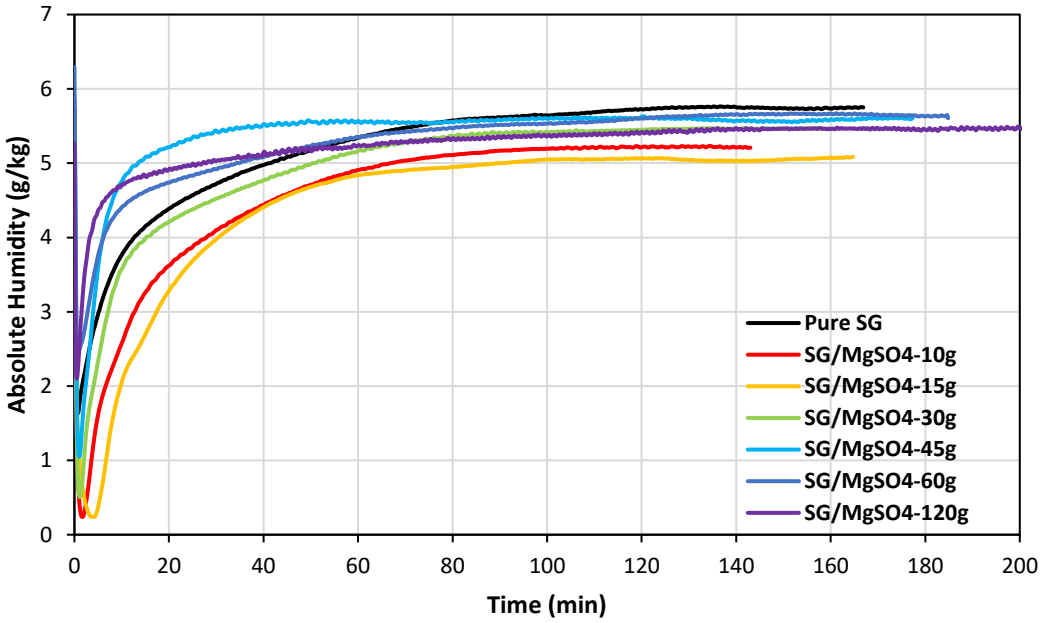

Figure 4-8. The outlet absolute humidity is plotted as a function of time during hydration for all 6 composites and pure silica gel. The inlet relative humidity was 50%, the flow rate was 12 SLPM, and the dehydration was performed at 120°C. Note that the inlet absolute humidity varied for each material (Table 4.3), since it is a function of the system pressure, and therefore system pressure drop (eq. 4.4 & eq. 4.5).

Although the inlet relative humidity was set to 50% for each experiment, the final outlet absolute humidity levels were not exactly the same for each sample. This is because each sample had a different pressure drop through the column and therefore different inlet absolute humidity levels (Table 4.3), since the RH is dependent on the total pressure (eq. 4.4 & eq. 4.5) and the total pressure at the inlet is the sum of the atmospheric pressure and the system pressure drop. The variation in pressure drop between samples is likely due to variation in particle size distributions and particle shapes from sample to sample and variance relating to packing the sorption column with the sample.

$$x_{H2O} = \frac{p_{H2O}^{sat} \times RH}{P_{tot}} \tag{4.4}$$

$$H = \frac{x_{H2O} \times M_{H2O}}{x_{H2O} \times M_{H2O} + (1 - x_{H2O}) \times M_{air}} \tag{4.5}$$

where x_{H2O} is the mole fraction of water vapour, p_{H2O}^{sat} is the saturation vapour pressure of water vapour at the temperature of the humid air (kPa), RH is the relative humidity (%), P_{tot} is the total pressure of the humid air, H is the absolute humidity (g/kg), M_{H2O} is the molar mass of water, and M_{air} is the molar mass of air.

Table 4-3. Inlet absolute humidity levels for each sample.

Sample Name	**Inlet Humidity (g/kg)**
Pure SG	5.77
SG/MgSO4-10g	5.23
SG/MgSO4-15g	5.08
SG/MgSO4-30g	5.45
SG/MgSO4-45g	5.43
SG/MgSO4-60g	5.64
SG/MgSO4-120g	5.50

The amount of water-vapour adsorbed is proportional to the area bound between the inlet and the outlet absolute humidity on the breakthrough curve. Based on this, the hydration capacity was calculated and plotted (Figure 4-9) for different SG- $MgSO_4$ composites.

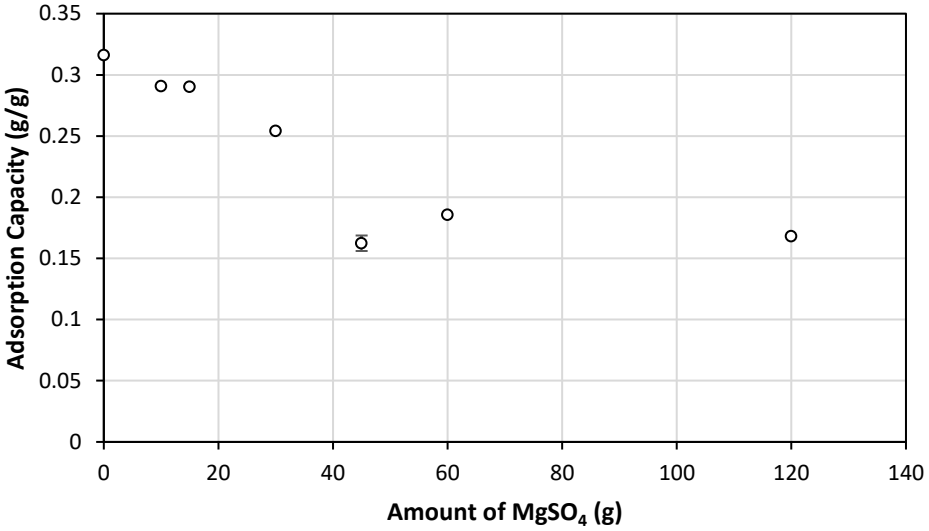

Figure 4-9. The amount of water vapour adsorbed during the hydration cycle at an inlet relative humidity of 50%, a flow rate of 12 SLPM after a dehydration at 120°C with a flow rate of 12 SLPM. The adsorption capacity is calculated based on the breakthrough curves. The weight percent on the x-axis was calculated based on the synthesis masses.

As the concentration of salt increases, the water vapour uptake capacity decreases. This is because after being regenerated at 120°C, $MgSO_4$ has a lower sorption capacity at 50% RH than silica gel. Additionally, by impregnating silica gel with $MgSO_4$ some of its active hydration sites are blocked, reducing the hydration capacity of the silica gel host matrix.

The temperature breakthrough curve shows important information about the thermal power profile over the course of the experiment. Additionally, the area under its curve is proportional to the energy storage density (see eq. 4.1 and section 4.4.5). The temperature breakthrough curves for pure silica gel and the six silica gel- $MgSO_4$ composites are given in Figure 4-10.

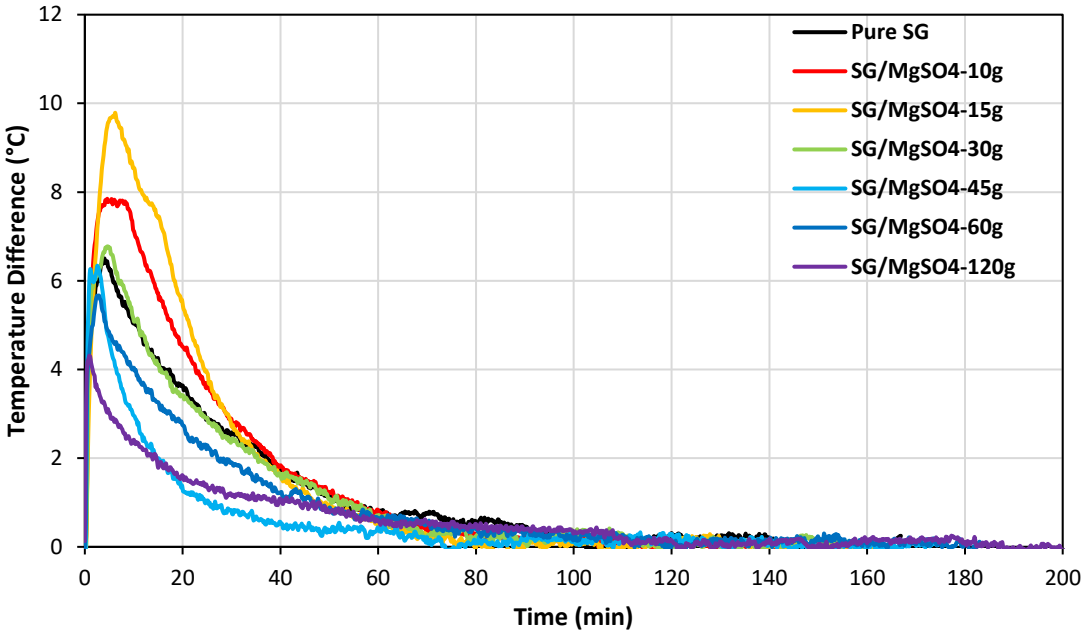

Figure 4-10. The temperature difference between the inlet and the outlet of the column over the course of the hydration experiment is plotted for all 6 composites and pure silica gel. Samples with a larger area under their temperature breakthrough curve exhibit higher energy storage density values (Figure 4-6). Additionally, a higher maximum temperature lift results in a higher maximum thermal power value (Figure 4-6). The inlet relative humidity was 50%, the flow rate was 12 SLPM, and the dehydration was performed at 120°C.

4.6 Conclusions

At the beginning of this study, four $MgSO_4$-based composites (AA/$MgSO_4$, AA/$MgSO_4$/PVA, AA+SG+13X/ $MgSO_4$, and SG/$MgSO_4$) were synthesized via dry impregnation and their energy storage performance and cyclic stability were tested using a lab-scale energy storage apparatus. All four hybrids were stable after 3 cycles. Of the four materials, SG/$MgSO_4$ had the highest performance, so more SG/$MgSO_4$ composites were synthesized with different amounts of $MgSO_4$ salt used to optimize that amount for the maximum energy storage performance.

$MgSO_4$/SG composites with different amounts of $MgSO_4$ (10 g, 15 g, 30 g, 45 g, 60 g, and 120 g) have been synthesized afterwards through dry impregnation method. The structural characteristics of these samples via SEM show the homogeneous distribution of the salt over the silica gel. Moreover, as we increase the salt concentration more deposition of the $MgSO_4$ over silica gel appeared, which is further confirmed by EDX.

By testing the energy storage performance of different $MgSO_4$ salt-in-matrix composites, it was found that all of the SG/$MgSO_4$ composites were stable after three hydration/dehydration cycles. It was observed that 33 wt % $MgSO_4$ salt (with 15 g of $MgSO_4$ addition) with silica gel showed the best thermal energy storage performance among all the composites studied in this work at a hydration inlet relative humidity of 50% after a dehydration at 120°C.

4.7 References

[1] A. Kalair, N. Abas , M.S. Saleem, A.R. Kalair, and N. Khan, Role of energy storage systems in energy transition from fossil fuels to renewable. Energy Storage. 135, 1-27, 2020.

[2] D. Lefebvre, F. H. Tezel. A review of energy storage technologies with a focus on adsorption thermal energy storage processes for heating applications. Renewable and Sustainable Energy Reviews, 67, 116-125, 2017.

[3] A.H. Abedin,. and M.A. Rosen, A Critical Review of Thermochemical Energy Storage Systems. The Open Renewable Energy Journal, 4, 42-46, 2011.

[4] I. Sarbu, and C.A. Sebarchievici, Comprehensive Review of Thermal Energy Storage. Sustainability, 10, 191, 2018.

[5] H. H. Al-Kayiem, S.C. Lin, and A. Lukmon. Review on Nanomaterials for Thermal Energy Storage Technologies. Nanoscience & Nanotechnology-Asia, 3, 60-71, 2013.

[6] A. Elsayed, E. Elsayed, R. Al-Dadah, S. Mahmoud, A. Elshaer, and W. Kaialy, Thermal energy storage using metal–organic framework materials. Applied Energy,186, 509-519, 2017.

[7] J. Janchen, T.H. Herzog and E. Thrun, Natural Zeolites in thermal adsorption storage and building materials for solar energy utilization in houses. 3rd Southern African Solar Energy Conference, South Africa, 11-13 May, 2015.

[8] A. Hauer. Thermal energy storage with zeolite for heating and cooling applications. Proceedings of 3rd Workshop of Annex. 17, 2002.

[9] B. Dawoud, E.-H. Amer and D.-M. Gross. Experimental investigation of an adsorptive thermal energy storage. Int. J. Energy Res. 31, 135–147, 2007.

[10] A. L. M. Reddy, S. R. Gowda, M. M. Shaijumon, P. M. Ajayan. Hybrid nanostructures for energy storage applications." Advanced Materials 24.37 (2012): 5045-5064.

[11] D. Dicaire and F. H. Tezel. Use of adsorbents for thermal energy storage of solar or excess heat: improvement of energy density. Int. J. Energy Res. 2013; 37:1059–1068.

[12] C. Barreneche, A. I. Fernández, L. F. Cabeza, R. Cuypers. Thermophysical characterization and thermal cycling stability of two TCM: CaCl2 and zeolite. Applied Energy 137, 2015, 726-730.

[13] A. Permyakova, S. Wang, E.Courbon, F. Nouar, N. Heymans, P. D'Ans, N. Barrier, P. Billemont, G. De Weireld, N. Steunou, M. Frère and C. Serre. Design of Salt-Metal Organic Frameworks Composites for Seasonal Heat Storage Applications. J Mater. Chem. A., 2013, 00, 1-3.

[14] S.Z. Xu, R.Z. Wang, L.W. Wang, and J. Zhu. Performance characterizations and thermodynamic analysis of magnesium sulfate-impregnated zeolite 13X and activated alumina composite sorbents for thermal energy storage. Energy, 167, 2019, 889-901.

[15] S. Hongois, F. Kuznik, P. Stevens, J.-J. Roux. Developement and characterisation of a new $MgSO_4$-zeolite composite for long-term thermal energy storage. Solar Energy Materials and Solar Cells, Elsevier, 95, 1831-1837, 2011.

[16] K. Korhammer, M.-M. Druske, A. Fopah-Lele, H. Urs Rammelberg, N. Wegscheider, O. Opel, T. Osterland, W. Ruck. Sorption and thermal characterization of composite materials based on chlorides for thermal energy storage. Applied Energy. 162, 1462-1472, 2016.

[17] Y.N. Zhang, R.Z. Wang , T.X. Li. Experimental investigation on an open sorption thermal storage system for space heating. Energy, 141, 2017, 2421-2433.

[18] S.Vasta, V. Brancato, D.L. Rosa, V. Palomba, G. Restuccia, A. Sapienza and A. Frazzica. Adsorption Heat Storage: State-of-the-Art and Future Perspectives. Nanomaterials, 8, 522, 2018.

[19] L.G. Gordeeva, A.V. Gubar, L.M. Plyasova, V.V. Malakhov, and A. Aristov. Composite Water Sorbents of the Salt in Silica Gel Pores Type: The Effect of the Interaction between the Salt and the Silica Gel Surface on the Chemical and Phase Compositions and Sorption Properties. Kinetics and Catalysis, 46, 736–742,2005.

[20] Y. Hua, A. Godin and F.H. Tezel. Water vapor adsorption in silica gel for thermal energy storage application. Advaced Materials Letters, 10, 124-127, 2019.

[21] H. Jarimi, D. Aydin, Z. Yanan, G. Ozankaya, X. Chen. and Riffat, S. Review on the recent progress of thermochemical materials and processes for solar thermal energy storage and industrial waste heat recovery. International Journal of Low-Carbon Technologies, 14, 44–69, 2019.

[22] A. Jabbari-Hichri, S. Bennici and A. Auroux. Effect of aluminum sulfate addition on the thermal storage performance of mesoporous SBA-15 and MCM-41 materials. Solar Energy Materials and Solar Cells, 149, 232-241, 2016.

[23] H. Jarimi, A. Devrim , Y. Zhang, Y. Ding, O. Ramadan, X. Chen, A. Dodo, Z. Utlu and S. Riffat. Materials characterization of innovative composite materials for solar-driven thermochemical heat storage (THS) suitable for building application. International Journal of Low-Carbon Technologies, 14, 313–325, 2019.

Chapter 5 - Impregnation and Microencapsulation of $CaCl_2$ Using Silica Gel and Methylcellulose for Thermochemical Energy Storage Applications

Curtis Strong, University of Ottawa

Suboohi Shervani, University of Ottawa

F. Handan Tezel, University of Ottawa

Abstract

Thermochemical energy storage (TCES) is a promising thermal energy storage technology due to its high energy density and minimal heat losses. Salt hydrates and salt hydrate composites, such as calcium chloride ($CaCl_2$) and $CaCl_2$-based composites, have shown favourable energy storage properties. However, these materials have shown issues with stability due to swelling, agglomeration, and deliquescence. In this work, $CaCl_2$ was stabilized using three methods, impregnation into silica gel, encapsulation in methylcellulose, and both stabilization techniques used simultaneously. Three $CaCl_2$-based composites were synthesized: silica gel impregnated with $CaCl_2$, $CaCl_2$ encapsulated by methylcellulose, and silica that was impregnated with $CaCl_2$ and then encapsulated in methylcellulose. Similarly, LiCl-based composites were also synthesized and examined in this work, but issues of deliquescence, swelling, and agglomeration made the materials impractical to work with. To determine material energy storage performance 2-6 g of active material was tested in a lab-scale energy storage apparatus. The $CaCl_2$-impregnated silica gel demonstrated high energy storage performance on the first cycle but was unstable after multiple hydration and dehydration cycles. The $CaCl_2$ encapsulated in methylcellulose showed high energy storage performance and good cyclic stability, but experienced slight agglomeration. The $CaCl_2$-impregnated silica gel that was encapsulated in methylcellulose showed the highest stability and energy storage performance after 3 hydration and dehydration cycles with minimal agglomeration. An energy storage density of 241 kWh/m^3 (0.87 GJ/m^3) and a specific energy of 630 Wh/kg (2268 kJ/kg) at 90 % relative humidity (RH) was achieved.

Keywords: Calcium chloride, Composites, Encapsulation, Hybrid, Impregnation, Lithium chloride, Methylcellulose, Salt hydrates, Silica gel, Sorption heat storage, Thermochemical energy storage

5.1 Nomenclature

$C_{p,air}$	Heat capacity of air (kJ/kg °C)
H	Absolute humidity (g/kg)
H_{inlet}	Absolute humidity at the column inlet (g/kg)
H_{outlet}	Absolute humidity at the column outlet (g/kg)
L	Length of the column (cm)
$\dot{m}_{air}$	Mass flow rate of air (g/min)
m_{bed}	Mass of adsorbent in the column (g)
M_{air}	Molar mass of dry air (kg/kmol)
M_{H2O}	Molar mass of water (kg/kmol)
p_{H2O}^{sat}	Saturation vapour pressure of water (kPa)
P_{tot}	Total pressure (kPa)
q	Water vapour uptake capacity (g/g)
$Q_{hydration}$	Energy released during hydration (kJ)
$\dot{Q}_{max}$	Maximum thermal power (W)
RH	Relative humidity (%)
t	Time (min)
T_{in}	Inlet temperature (°C)
T_{out}	Outlet temperature (°C)
V	Volume of the column (cm^3)
x_{H2O}	Volume mixing ratio (-)

Greek Letters

ΔT_{max}	Maximum temperature difference (°C)
ρ_{bulk}	Bulk density (kg/m^3)
⌀	Diameter (cm)

5.2 Abbreviations

$CaCl_2$	Calcium chloride
DSC	Differential scanning calorimetry
ESD	Energy storage density
LiCl	Lithium chloride
MC	Methylcellulose
MOF	Metal-organic-framework
PCMs	Phase change materials
RH	Relative humidity
SE	Specific energy
SG	Silica gel
SLPM	Standard liters per minute
TCES	Thermochemical energy storage
TES	Thermal energy storage
TGA	Thermogravimetric analysis

5.3 Introduction

The use of renewable thermal energy sources, like thermal solar power, has been increasing for many years and is expected to continue increasing in the coming decades [1]. Despite the advantages of technologies such as solar thermal, their heat output varies with the amount of solar irradiation [2]. Solar irradiation varies hourly, daily, and seasonally, which results in an inconsistent thermal power output. Furthermore, this variance in power supply output does not match up with the consumer demand, creating a supply and demand mismatch, with respect to time. This demonstrates the need for and importance of thermal energy storage (TES) technology.

Conventional TES technologies involve sensible and latent heat, but these systems have various disadvantages like low energy storage density, the need for toxic chemicals, and significant heat losses [3]. Thermochemical energy storage (TCES) is a newer technology which involves a chemical transformation. TCES theoretically exhibits no heat losses during storage, high energy densities, and no need for toxic chemicals. This makes it an attractive alternative to sensible and latent heat storage.

Salt hydration/dehydration reactions have been favourable options for space heating and domestic hot water applications, due to their optimal operating temperature ranges, high energy density values, and lack of toxic chemicals [3–5]. One popular reaction involves the hydration/dehydration of $CaCl_2$ [6–14]. This salt has favourable hydration and dehydration temperatures, is non-toxic, is inexpensive, has a high heat of sorption, and a large water vapour sorption capacity. However, it has been criticized for its low temperature lifts [4]. Further, $CaCl_2$ and many other hygroscopic salts with high water sorption capacity experience practical issues like deliquescence, swelling, particle agglomeration which lead to lack of cyclic stability [4].

To mitigate these issues, researchers have tried impregnating porous matrix materials with $CaCl_2$ and other hygroscopic salts [6–14]. A variety of host materials have been used including alumina [15], carbonaceous materials [16], cement [17], porous silica [14], metal-organic-frameworks (MOFs) [18] and zeolites [19]. Some researchers have also attempted encapsulation of the salts in polymeric coatings and hollow spheres in order to stabilize them [20–22]. There has also been significant attention related to the encapsulation of phase change materials (PCMs) [23]. These techniques have successfully increased the stability of hygroscopic salts and PCMs, although many of these composites still experience a decrease in performance after multiple hydration and dehydration cycles [24].

Silica gel is a popular commercial desiccant. It is porous and amorphous, and its pore structure varies depending on the synthesis conditions. It has a high water-vapour sorption capacity, as well as a large surface area and pore volume [25]. As such, many researchers have opted to use this material as a matrix for hydration/dehydration material stabilization. Gordeeva *et al*. synthesized a silica gel/$CaCl_2$ composite and tested it using thermogravimetric analysis (TGA) and differential scanning calorimetry (DSC) analysis. The composite exhibited a sorption capacity of 1.2 g/g and specific energy of 940 Wh/kg at 80% RH and 25°C (25.4 mbar) [26]. Zhu *et al*. have also synthesized a silica gel/$CaCl_2$ composite which showed a water vapour uptake capacity of 0.73 g/g and specific energy of 264 Wh/kg at 30°C and 80% RH (34 mbar). This material was tested using a lab-scale energy storage apparatus prototype [24]. Courbon *et al*. have made improvements to the synthesis method of $CaCl_2$/silica gel composites and achieved an energy storage density of 211 kWh/m^3 (0.76 GJ/m^3) and a water vapour uptake capacity of 0.4 g/g at a water vapour pressure of 12.5 mbar (30% RH), an adsorption temperature of 30°C, and a desorption temperature of 80°C [14]. There have also been other silica-based materials like MCM-41, SBA-15, and aluminosilicate which have been successfully impregnated with $CaCl_2$ and have achieved high energy storage density and water uptake values [8, 13, 27]. Despite the promising performance of these materials, silica/$CaCl_2$ composites lack stability [24, 28]. This has prompted the need for new composites and synthesis methods which can adequately stabilize hygroscopic salts like $CaCl_2$ and minimize practical issues, like particle agglomeration and deliquescence, while maintaining high energy storage performance.

The mircoencapsulation of PCMs has been explored thoroughly in the literature [23], but the literature about encapsulation of hygroscopic salts is scarce. Shkatulov *et al*. synthesized hollow mesoporous silica shells and filled them with $CaCl_2$, LiCl, and $SrBr_2$ [21]. The $CaCl_2$ material was stable for up to 50 cycles and showed a specific energy of 305 Wh/kg and an energy density of 0.9 GJ/m^3 (250 kWh/m^3), with a hydration water vapour pressure of 15 mbar. The LiCl and $SrBr_2$ samples were also stable, and they showed energy density values of 0.6 GJ/m^3 and 0.65 GJ/m^3 (167 kWh/m^3 and 181 kWh/m^3), respectively. Note that the LiCl sample was subjected to 15 mbar of water vapour pressure whereas the $SrBr_2$ sample water vapour pressure was 21 mbar. Cuypers *et al*. reported that encapsulating $CaCl_2$ enhanced physical stability and kinetics [22]. Gaeini *et al*. encapsulated $CaCl_2$ with an ethylcellulose coating. They found that the encapsulated material showed improved cyclic stability and made the kinetics faster. They also observed an energy storage density value of 0.4 GJ/m^3 (111.1 kWh/m^3) at 13 mbar hydration water vapour pressure and 20°C, which is a 75% decrease compared to pure $CaCl_2$ [20]. It was also reported that issues of swelling and agglomeration were still present for the ethylcellulose coated $CaCl_2$. Similar to ethylcellulose, methylcellulose (MC) is a non-toxic and environmentally friendly polymeric material derived from

cellulose, often used commercially as an emulsifier or thickener [29]. It has not been previously used for the encapsulation of TCMs, but MC and its derivatives have been used for encapsulation of other materials [30–33]. In the current study, it is used to hold $CaCl_2$ in silica gel matrix and to encapsulate pure $CaCl_2$.

In this study, a novel technology involving the simultaneous impregnation of hygroscopic salts into a porous host matrix and encapsulation by a polymeric coating was implemented. Calcium chloride, a promising hygroscopic salt for thermal energy storage and transformation applications, was stabilized using three methods: impregnation in silica gel, encapsulation in methylcellulose, and simultaneous impregnation in silica gel and encapsulation in methylcellulose; the latter two compound have yet to be seen in the literature. The three materials were synthesized and tested then compared to pure silica gel. Additionally, three LiCl composites were synthesized and tested using the same methodologies as for the $CaCl_2$-based composites, but the LiCl composites exhibited practical issues, which will be discussed in section 5.5.1.

5.4 Experimental

5.4.1 Material preparation

$CaCl_2$-based composites have been synthesized via impregnation and encapsulation methods. Silica gel was provided from Xebec Adsorption Inc. (Blainville, QC, Canada) and the $CaCl_2$ and LiCl were purchased from Fisher Scientific (Ottawa, ON, Canada). Methylcellulose was purchased from Sigma Aldrich, Canada (Oakville, ON, Canada). A table listing all of the composites and their abbreviated names are provided in Table 5-1.

Table 5-1. List of all materials tested in this study and their abbreviated names.

Composite	**Acronyms**
Pure silica gel	Pure SG
Silica gel/$CaCl_2$	SG/$CaCl_2$
Methylcellulose/$CaCl_2$	MC/$CaCl_2$
Methylcellulose + silica gel/$CaCl_2$	MC+SG/$CaCl_2$
Methylcellulose + silica gel/LiCl	MC+SG/LiCl

Figure 5-1 represents the mechanism used to encapsulate the silica gel and salt hydrate by methylcellulose. Impregnation is the process where salt adheres to the surface and pores of the host, while encapsulation is the process where a material forms an envelope around the sorbent material. In

the current study, methylcellulose is used to encapsulate the pure $CaCl_2$ and to encapsulate a silica gel/$CaCl_2$ composite because the deliquescence relative humidity of the $CaCl_2$ is very low, and it is not stable on its own or in the silica gel without encapsulation. The current study shows the simultaneous impregnation and encapsulation of salt hydrate into the host matrix for the first time.

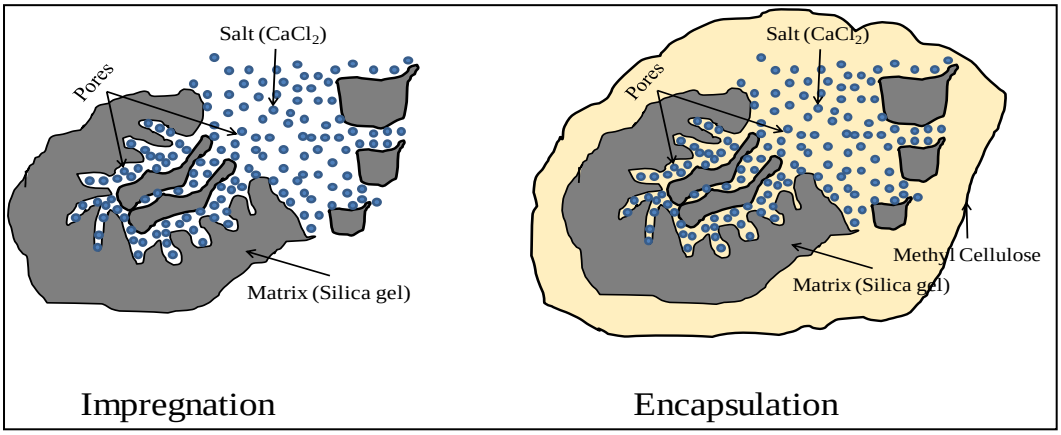

Figure 5-1. Schematic representation of impregnation and encapsulation mechanisms used for the current study.

5.4.1.1 SG/$CaCl_2$ Synthesis

First, 30 g of silica gel was kept inside a beaker filled with 100 mL ethanol for half an hour to remove the impurities and contaminations. Silica gel was then extracted from ethanol. 15 g of $CaCl_2$ and 30 g of silica gel were mixed together in 100 mL de-ionized (DI) water. The solution was stirred continuously for 24 h. The mixture was dried for 6 h at 120°C in oven.

5.4.1.2 MC/$CaCl_2$ Synthesis

15 g of $CaCl_2$ and 10 g MC were mixed together in 100 mL de-ionized (DI) water and 5 mL of ethanol was poured into the mixture. The solution was stirred continuously for 24 h. The mixture was dried for 24 h at 90°C in an oven.

5.4.1.3 MC+SG/$CaCl_2$ Synthesis

First, 30 g of silica gel was kept inside a beaker filled with 100 mL ethanol for half an hour to remove the impurities and contaminations. Silica gel was then extracted from ethanol. 15 g $CaCl_2$, 10 g MC and 30 g silica gel were mixed together in 100 mL de-ionized (DI) water and 5 mL of ethanol was poured into the mixture. The solution was stirred continuously for 24 h. The mixture was then dried for 24 h at 90°C in an oven.

5.4.1.4 MC+SG/LiCl Synthesis

First, 30 g of silica gel was kept inside a beaker filled with 100 mL ethanol for half an hour to remove the impurities and contaminations. Silica gel was then extracted from ethanol. 15 g of LiCl, 10 g MC and 30 g of silica gel were mixed together in 100 mL de-ionized (DI) water and pour 5 mL ethanol into the mixture. The solution was stirred continuously for 24 h. The mixture was dried for 24 h at 90°C in an oven.

5.4.2 Energy storage apparatus and methodology

A lab scale energy storage apparatus was used to test the energy storage performance. The system and methodology used is similar to those described in Hua, *et al*. [34]. The schematic diagram of the energy storage apparatus is given in Figure 5-2. The stainless-steel sorption column, covered in fiberglass insulation, had a volume of 7.15 cm^3, with an inner diameter of 1.09 cm and a length of 7.67 cm. Small pieces of glass wool were placed at the inlet and outlet of the column to avoid particles exiting the column. The column was filled with 2-6 g of adsorbent material, depending on the bulk density. The material was crushed and sieved to a 7×20 mesh size (0.841 mm – 2.83 mm) using a mortar and a pestle. Note that the MC/$CaCl_2$ sample was rubbery and elastic, so unlike the more brittle samples, it could not be crushed with a mortar and pestle. Therefore, it was chopped into finer pieces using a knife.

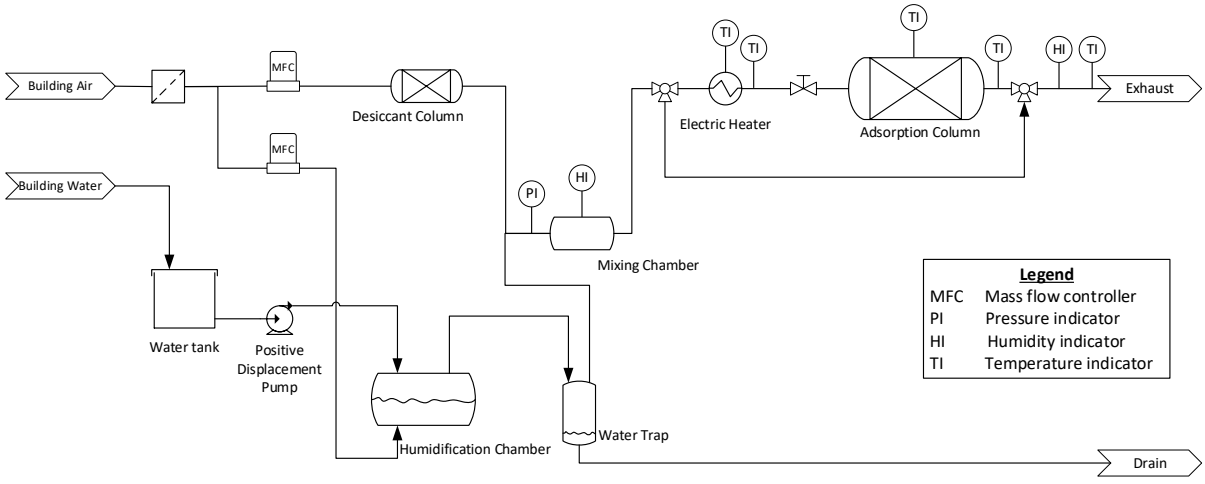

Figure 5-2. Schematic diagram of the lab-scale energy storage apparatus that was used to test the energy storage performance of the materials in this study. All measurements were recorded electronically using LabVIEW.

To dehydrate the sample and store thermal energy, air with an RH of 0-3% at room temperature (≈22°C) was heated to 120°C and flowed over the column at a rate of 12 standard litres per minute (SLPM). The flow rate and humidity levels are controlled using two mass flow controllers at the inlet of the column. The dehydration continued until the RH reading at the outlet of the column was less than 3% for at least 15 minutes. Following dehydration, the column was isolated by closing the inlet and outlet valves and left to cool to room temperature overnight.

During hydration, the stored energy was released by humidifying dry building air at room temperature to 50% or 90% RH (13 mbar or 24 mbar partial pressure of water vapour) and allowing the humid air to pass over the column, at a flow rate of 12 SLPM. This allowed the water molecules in the air to be adsorbed by the adsorbent. The hydration experiment proceeds until the humidity reading at the outlet of the column remains constant for at least 15 minutes. Since the column is insulated and nearly adiabatic, this results in a temperature increase at the outlet of the column, due to the exothermic nature of adsorption, which is monitored and recorded by a temperature sensor. The total energy released during hydration is then calculated using eq. 5.1, with the information from the column inlet and outlet temperatures, the mass flow reading from the mass flow controller, and the heat capacity of air at the given temperature and humidity level. Note that zero is the time at the start of the hydration and t is the time at the end of the experiment.

$$Q_{hydration} = \int_0^t \dot{m}_{air} C_{p,air} (T_{out} - T_{in}) dt \qquad (5.1)$$

where $Q_{hydration}$ is the amount of heat released during the hydration portion of the experiment (kJ), t is the total time the hydration takes place (min), $\dot{m}_{air}$ is the mass flow rate of air passing over the column (kg/min), $C_{p,air}$ is the specific heat capacity of the humid air (kJ/kg°C), T_{out} is the temperature at the outlet of the sorption column (°C), and $T_{in}$is the temperature at the inlet of the sorption column (°C).

Based on $Q_{hydration}$, the energy storage density (ESD) and specific energy (SE) can be calculated. The ESD was calculated by dividing $Q_{hydration}$ by the column volume (7.15 cm^3) and the SE was calculated by dividing $Q_{hydration}$ by the mass of the dehydrated sample. The maximum thermal power can also be calculated from these results. It is taken as the product of the maximum temperature difference between the inlet and outlet column temperatures during hydration (ΔT_{max}), the specific heat capacity of air, and the mass flow rate as shown in (eq. 5.2).

$$\dot{Q}_{max} = \dot{m}_{air} C_{p,air} \Delta T_{max} \quad (5.2)$$

where $\dot{Q}_{max}$ is the maximum thermal power observed during the experiment (W), $\dot{m}_{air}$ is the mass flow rate of humid air (kg/s), $C_{p,air}$ is the specific heat capacity of humid air (J/kg°C), and ΔT_{max} is the highest observed difference between the inlet and outlet temperature of the column (°C).

The absolute humidity and water-vapour concentration (H), were calculated using eq. 5.3 & eq. 5.4, respectively. Then, based on the difference in inlet and outlet absolute humidity over the course of the water-vapour breakthrough experiment, the water vapour uptake capacity was calculated using eq. 5.5. Note that at the inlet of the column, the total pressure (P_{tot}) is assumed to be 101.3 kPa plus the reading on the pressure gauge by the mixing chamber (Figure 5-2), and the pressure at the outlet of the column is assumed to be 101.3 kPa.

$$x_{H2O} = \frac{p_{H2O}^{sat} \times RH}{P_{tot}} \quad (5.3)$$

$$H = \frac{x_{H2O} \times M_{H2O}}{x_{H2O} \times M_{H2O} + (1 - x_{H2O}) \times M_{air}} \quad (5.4)$$

$$q = \frac{\left(\int_0^t \dot{m}_{air} \times (H_{inlet} - H_{outlet}) dt\right)}{m_{bed}} \quad (5.5)$$

where x_{H2O} is the mole fraction of water vapour, p_{H2O}^{sat} is the saturation vapour pressure of water vapour at the temperature of the humid air (kPa), RH is the relative humidity (%), P_{tot} is the total pressure of the humid air, H is the absolute humidity (g/kg), M_{H2O} is the molar mass of water, M_{air} is the molar mass of air, q is the total amount of water vapour adsorbed throughout the hydration experiment per gram or adsorbent (g/g), t is the duration of the hydration experiment (min), m_{air} is the mass flow rate of humid air (kg/min), H_{inlet} is the absolute humidity at the inlet of the column (g/kg), H_{outlet} is the absolute humidity at the outlet of the column (g/kg), and m_{bed} is the mass of adsorbent contained in the column.

5.5 Results and discussion

5.5.1 Energy storage performance

All three composite materials and pure silica gel were tested at a hydration inlet relative humidity of 50% at room temperature (≈22°C) and a regeneration temperature of 120°C. The flow rate during both hydration and dehydration was 12 SLPM. Each material underwent three consecutive dehydration and hydration cycles. Based on these experiments, the ESD, maximum thermal power, SE, and water-vapour uptake capacity were calculated for each of these three cycles. The results for all of these experiments can be seen in Figure 5-3.

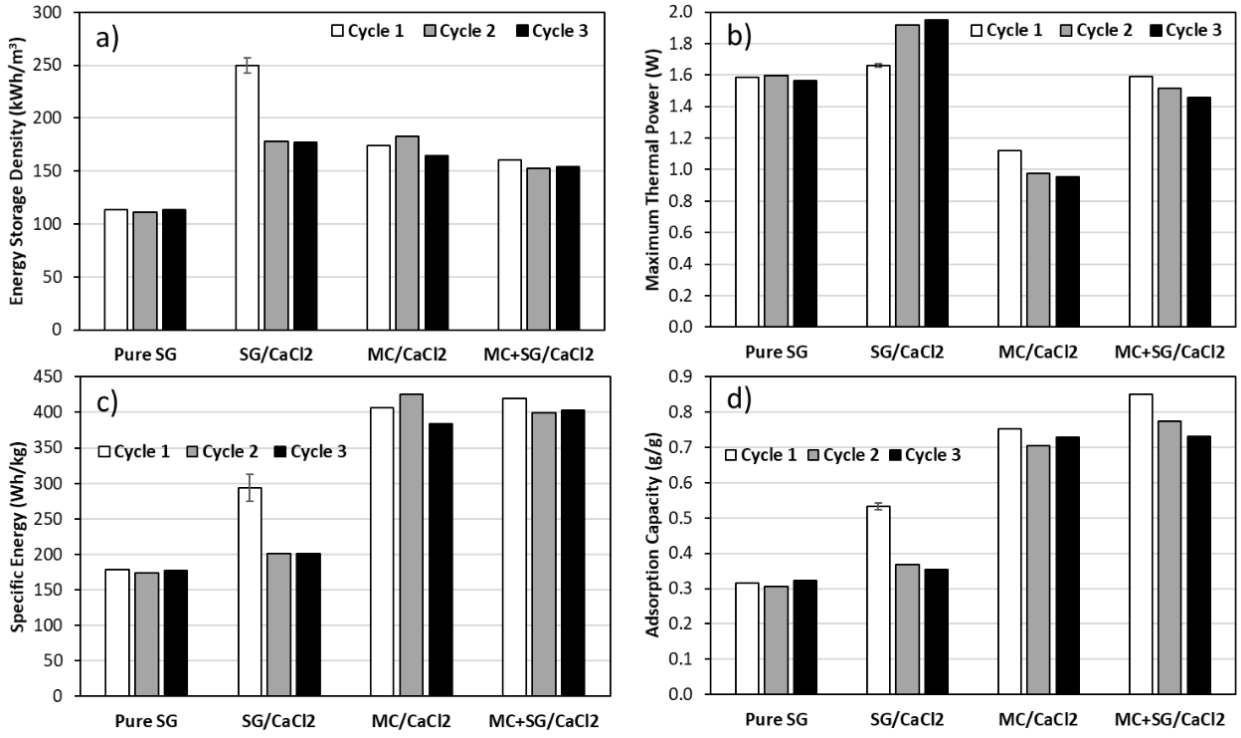

Figure 5-3. Three hydration/dehydration cycles at a regeneration temperature of 120°C, adsorption inlet relative humidity of 50%, and flow rate of 12 SLPM were performed. The a) energy storage density b) maximum thermal power c) specific energy and d) water-vapour uptake capacity are all plotted. The error bars on the first cycle of SG/$CaCl_2$ are based on repeated experiments.

Pure silica gel showed low performance apart from its relatively high maximum thermal power, but it had excellent stability and its performance did not decrease during the three hydration/dehydration cycles. The SG/$CaCl_2$ sample had high performance on the first cycle but much lower performance in the subsequent cycles, except for maximum thermal power. This is likely due to the salt not being properly bound to the silica gel and then detaching itself from the silica gel during hydration and leaving the column. Its performance after multiple cycles is close to that of pure silica gel, since most of the salt has likely left the matrix. The MC/$CaCl_2$ and MC+SG/$CaCl_2$ also have high energy storage performance and are more stable than the SG/$CaCl_2$ sample. However, both of these materials show a slight decrease in performance after each cycle, implying that there may still be some instability. Additionally, the MC/$CaCl_2$ particles exhibited slight agglomeration after the three cycles. In Figure 5-3a, it appears that on the second and third cycle all of the composites show similar ESD values. However, the SE of the MC/$CaCl_2$ and MC+SG/$CaCl_2$ samples are much higher. This is because the bulk density of MC/$CaCl_2$ and MC+SG/$CaCl_2$ was much lower than that of the SG/$CaCl_2$ sample and pure silica gel (Figure 5-4).

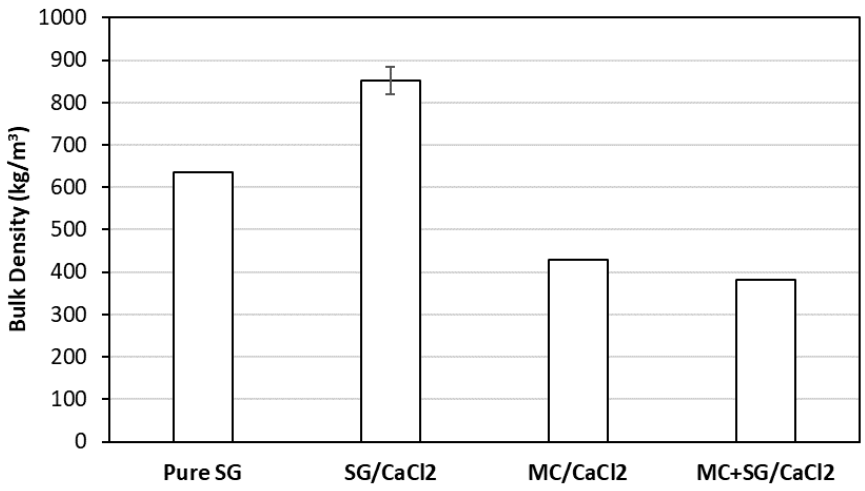

Figure 5-4. The bulk density values of pure silica gel and the three composites were measured by weighing the column that was filled with dehydrated sample and dividing the sample mass by the column volume. The error bar for the SG/$CaCl_2$ sample are based on repeated experiments for this material.

The temperature and concentration breakthrough curves for each material were plotted for all three cycles for silica gel and the three $CaCl_2$-based composites (Figure 5-5 & Figure 5-6). Note that not all of the trials exhibited the same outlet humidity at the end of the hydration. This is because the pressure drop was not the same for all samples and therefore the inlet total pressure was different for each sample. This resulted in variance in the inlet humidity, as per eq. 5.3 and eq. 5.4.

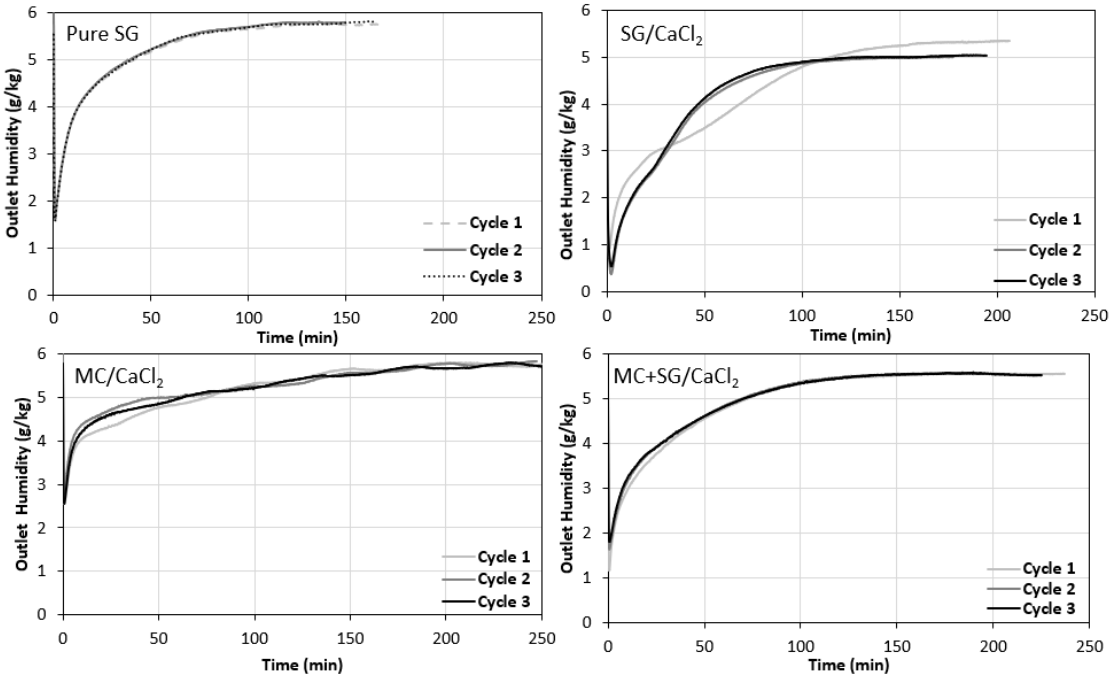

Figure 5-5. The concentration breakthrough curves for all three hydration cycles for pure silica gel and the three $CaCl_2$-based composite materials after a regeneration temperature of 120°C. The inlet RH was set at 50%, and the flow rate was 12 SLPM.

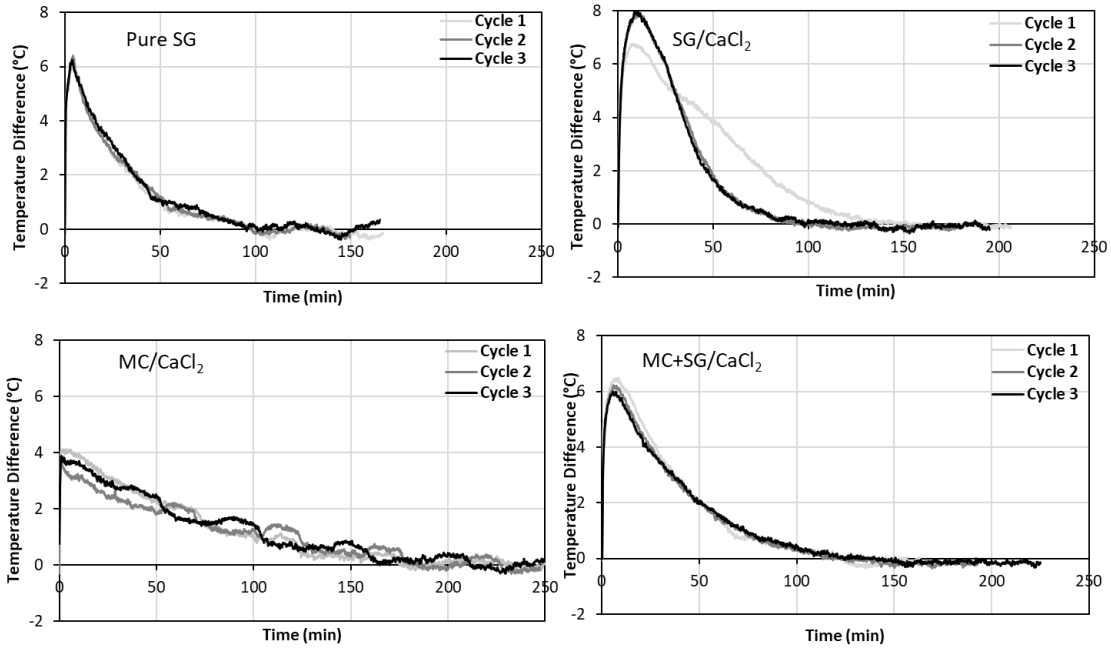

Figure 5-6. Temperature breakthrough curves for all three hydration cycles for pure silica gel and the three $CaCl_2$-based composite materials after a regeneration temperature of 120°C. The inlet RH was set at 50%, and the flow rate was 12 SLPM. The temperature difference was defined as the difference between the inlet and outlet temperature of the column.

In Figure 5-5, we can see that the pure silica gel breakthrough curves are nearly superimposed for cycles 1-3. It is also apparent that the SG/$CaCl_2$ exhibits a significant change after the first cycle, which completely changes the shape of the breakthrough curve. The MC/$CaCl_2$ sample showed a more gradual and sluggish breakthrough behavior. It also shows higher variations in humidity readings compared to the other samples since it was more sensitive to the atmospheric temperature. This is because the MC/$CaCl_2$ sample was known to swell slightly so the column was packed very loosely, meaning that there was less solid material to act as a heat sink and therefore it was more directly affected by the ambient temperature, which oscillated due to the temperature control system in the laboratory. This is further supported by the temperature oscillations seen in Figure 5-6 for MC/$CaCl_2$. The MC+SG/$CaCl_2$ breakthrough curve was similar to that of pure silica gel but with a slightly lesser slope. There is also a slight but discernable increase in the rate of change of the outlet humidity as the number of cycles increases. This is likely related to the water-vapour uptake capacity slightly decreasing after multiple cycles (Figure 5-3d).

In Figure 5-6, the pure silica gel temperature breakthrough curve shows a sudden and sharp increase at the beginning of the experiment, followed by a very long tail. All three cycles exhibit similar behavior. For the first cycle for the SG/$CaCl_2$ sample a large initial temperature lift is observed, then the temperature difference decreases almost linearly and finally tails off. However, in the subsequent two cycles, the maximum temperature lift is higher, but the tailing is more rapid. This ultimately reduces the area under the curve and therefore the ESD (Figure 5-3a). However, the second and third cycles for SG/$CaCl_2$ are almost coincident, further supporting that there is a significant change in the material properties after the first cycle but very little change after the second. Once again, the MC/$CaCl_2$ breakthrough experiences oscillations due to changes in ambient temperature. This is attributed to the fact that the MC/$CaCl_2$ experienced slight swelling and was therefore packed very lightly into the column, leaving large void space and increasing the relative effects of the ambient temperature since there is less sorbent material to act as a heat sink. Finally, the MC+SG/$CaCl_2$ sample shows an initial peak in temperature difference then a long tail, similar to pure silica gel but with a lower maximum temperature difference, and a broader tailing. As the cycle number increases, the maximum temperature lift decreases and the overall area under the curve decreases, implying that the ESD, SE, and maximum thermal power decreases slightly after each cycle, as was observed in Figure 5-3.

The MC+SG/$CaCl_2$ sample exhibited the best energy storage performance and stability out of the tested materials, and unlike MC/$CaCl_2$ it did not exhibit practical issues like swelling or agglomeration. As such, a fourth dehydration at 120°C and fourth hydration at an inlet humidity of 90% RH was performed. The energy storage performance and breakthrough curves under these conditions are given in Figure 5-7 and Figure 5-8, respectively.

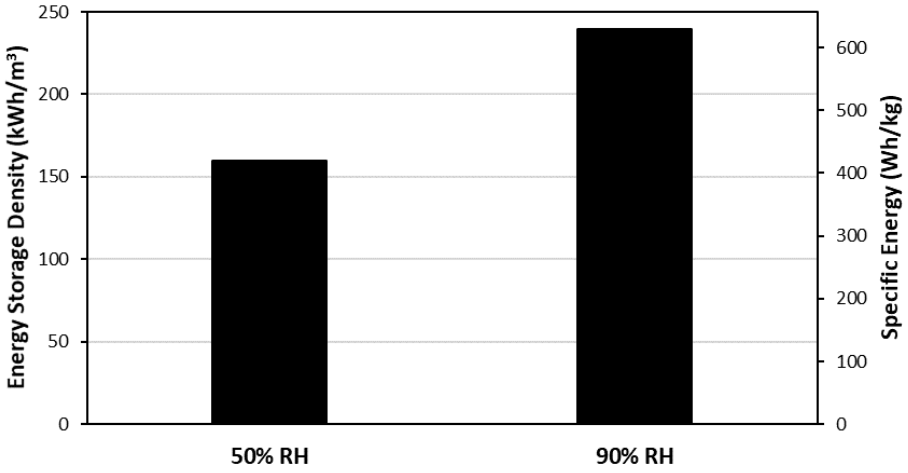

Figure 5-7. The energy storage density and the specific energy for MC+SG/$CaCl_2$ at 50% inlet RH and 90% inlet RH after the regeneration temperature of 120°C for a flow rate of 12 SLPM. The values for 50% RH, are the average value of the three cycles in Figure 5-3.

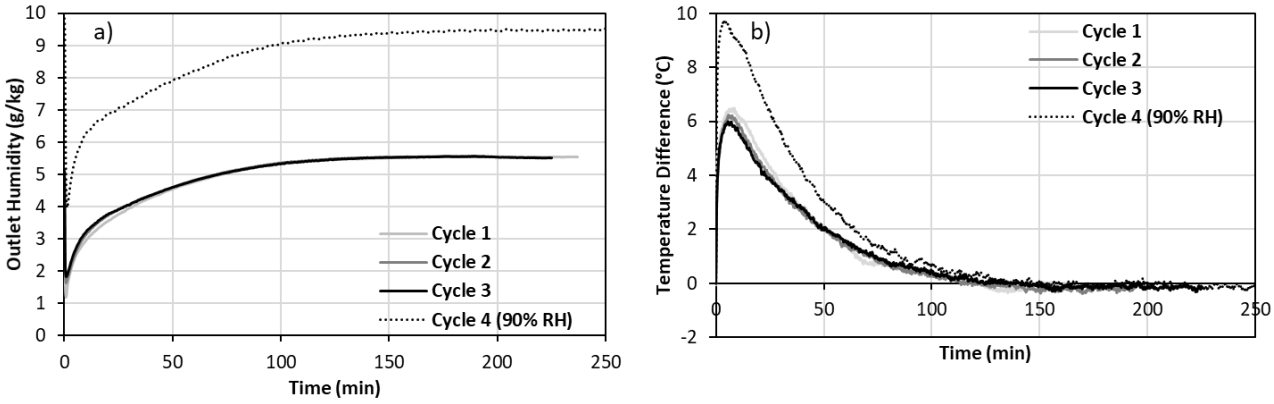

Figure 5-8. The a) concentration breakthrough curve and b) temperature breakthrough curve for MC+SG/$CaCl_2$ for 3 consecutive cycles (cycles 1-3) at 50% inlet RH and one subsequent cycle (cycle 4) at 90% inlet RH. The regeneration temperature was 120°C and the flow rate was 12 SLPM for all experiments.

The ESD and SE of the MC+SG/$CaCl_2$ increased by 50% when the inlet RH was increased from 50% to 90%. Additionally, the concentration and temperature breakthrough behaviours were significantly affected. The slope of the concentration breakthrough curve at the start of the experiment is much larger when the inlet RH is 90% and the maximum temperature difference is about 4°C higher than the three cycles at an inlet RH of 50%.

LiCl-based composites were also synthesized and tested since LiCl has high heat of adsorption values and water vapour uptake capacity [4]. However, it swells considerably more than $CaCl_2$ and its deliquescence relative humidity is lower [4]. Therefore, when the LiCl samples were tested in the lab-scale energy storage apparatus, there was significant issues of deliquescence, swelling, and agglomeration (Figure 5-9a). This even resulted in a cake being formed on the glass wool at the exit of the column (Figure 5-9b). These issues ultimately caused an increase in pressure drop in the column as the hydration experiment progressed until the flow was completely blocked by the agglomerated particles, causing the release of a pressure relief valve. Therefore, the LiCl samples could not be practically tested using the same system as the $CaCl_2$-based composites.

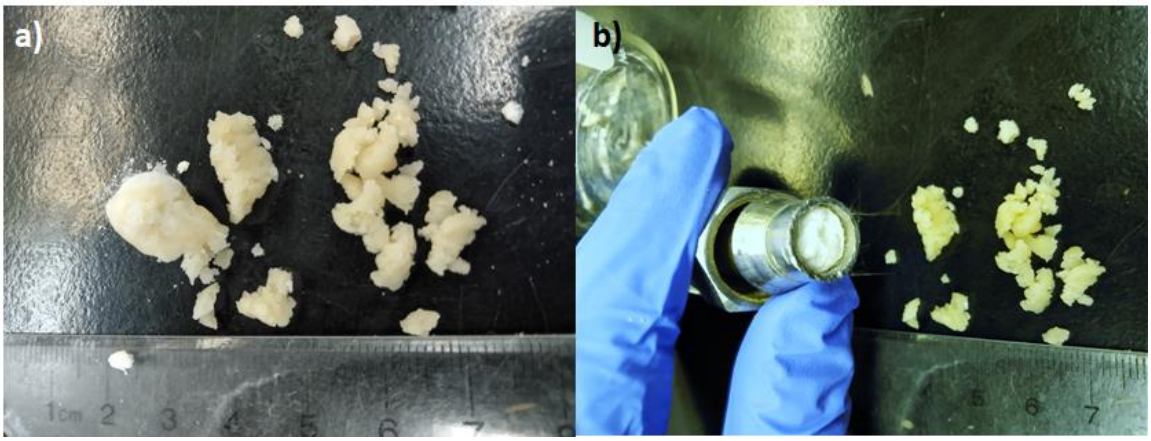

Figure 5-9. Two photos of the MC+SG/LiCl composite after a dehydration at 120°C and 12 SLPM and a hydration at 50% RH where

a) significant particle agglomeration was observed

b) a filter cake was formed on the glass wool at the exit of the column, blocking the flow through the column.

Note that the original particle size was 0.841 mm – 2.83 mm before the hydration experiment.

5.6 Conclusions

In this study, three $CaCl_2$-based composites (SG/$CaCl_2$, MC/$CaCl_2$, and MC+SG/$CaCl_2$) were synthesized for low temperature long-term TCES applications. The SG/$CaCl_2$ sample was synthesized by dry impregnation method, the MC/$CaCl_2$ composite was synthesized by encapsulation method and the and MC+SG/$CaCl_2$sample was synthesized by employing both the dry impregnation method and the encapsulation method. $CaCl_2$ has high energy storage performance but needs to be stabilized as it has low deliquescence relative humidity, and it was shown that impregnation and encapsulation are effective ways to enhance performance and stability.

All of the composite materials and a pure silica gel sample were tested using a lab-scale energy storage apparatus at a regeneration temperature, flow rate, and hydration inlet RH of 120°C and 12 SLPM, and 50% respectively. The SG/$CaCl_2$ composite exhibited high energy storage performance on the first cycle (ESD = 249 kWh/m^3 & SE = 294 Wh/kg), but its performance decreased starkly in the second and third cycle. The MC/$CaCl_2$ sample exhibited high energy storage performance (ESD ≈ 174 kWh/m^3 & SE ≈ 406 Wh/kg) and high stability after 3 cycles, but it exhibited some mild swelling and agglomeration, despite the column being packed very lightly. The MC+SG/$CaCl_2$ composite had high stability and energy storage performance (ESD ≈ 156 kWh/m^3 & SE ≈ 407 Wh/kg), and it did not exhibit any practical use issues like the MC/$CaCl_2$ composite. This implies that using impregnation and encapsulation simultaneously results in high stability composites without a large sacrifice in performance.

LiCl-based composites were also synthesized, and an attempt was made to test them in the lab-scale energy storage apparatus. Due to issues with deliquescence and swelling, particle agglomeration occurred and a cake was formed at the exit of the column. This caused an increase in pressure drop as the hydration progressed and ultimately blocked the flow through the column, making it impossible to test the material performance.

Since the MC+SG/$CaCl_2$ composite showed high energy storage performance and stability at a hydration inlet RH of 50% for 3 cycles, a fourth cycle was performed at an inlet RH of 90%. This resulted in a 50% increase in the energy storage density and specific energy (ESD = 241 kWh/m^3 & SE = 630 Wh/kg). Additionally, the maximum temperature lift increased by 4°C at a flow rate of 12 SLPM.

The MC+SG/$CaCl_2$ composite showed excellent stability and energy performance at 50% RH and 90% RH, at a regeneration temperature of 120°C and flow rate of 12 SLPM. Since it is known that operating conditions have a significant impact on energy storage performance of sorption-based energy storage systems [35–37], further experiments should be performed under different conditions and the cyclic stability should be investigated further. Furthermore, other salts (e.g. $MgSO_4$, $CuCl_2$), matrices (e.g. zeolite 13X, activated alumina), and encapsulation materials (e.g. ethylcellulose) can be used to synthesize similar composites that may also exhibit favorable energy storage properties.

5.7 References

[1] IEA, “Renewables 2019,” 2019.

[2] P. Warneck and J. Hansen, “Global Warming: The Complete Briefing,” *J. Atmos. Chem.*, vol. 30, no. 3, pp. 409–412, 1998.

[3] D. Lefebvre and F. H. Tezel, “A review of energy storage technologies with a focus on adsorption thermal energy storage processes for heating applications,” *Renew. Sustain. Energy Rev.*, vol. 67, pp. 116–125, 2017.

[4] P. A. J. Donkers, L. C. Sögütoglu, H. P. Huinink, H. R. Fischer, and O. C. G. Adan, “A review of salt hydrates for seasonal heat storage in domestic applications,” *Appl. Energy*, vol. 199, pp. 45–68, 2017.

[5] L. Scapino, H. A. Zondag, J. Van Bael, J. Diriken, and C. C. M. Rindt, “Sorption heat storage for long-term low-temperature applications: A review on the advancements at material and prototype scale,” *Appl. Energy*, vol. 190, pp. 920–948, 2017.

[6] A. Ristić and S. K. Henninger, “Sorption composite materials for solar thermal energy storage,” *Energy Procedia*, vol. 48. pp. 977–981, 2014.

[7] K. Korhammer, M. Druske, F.-L., Armand, H. U. Rammelberg, N. Wegscheider, O. Opel, T. Osterland, W. Wolfgang, “Sorption and thermal characterization of composite materials based on chlorides for thermal energy storage,” Appl. Energy, vol. 162, pp. 1462–1472, 2016.

[8] A. Jabbari-Hichri, S. Bennici, and A. Auroux, “Enhancing the heat storage density of silica–alumina by addition of hygroscopic salts ($CaCl_2$, $Ba(OH)_2$, and $LiNO_3$),” *Sol. Energy Mater. Sol. Cells*, vol. 140, pp. 351–360, 2015.

[9] R. Sutton, E. Jewell, J. Searle, and J. Elvins, “Discharge performance of blended salt in matrix materials for low enthalpy thermochemical storage,” *Appl. Therm. Eng.*, vol. 145, no. September, pp. 483–493, 2018.

[10] Y. I. Aristov, G. Di Marco, M. Tokarev, and V. Parmon, “Selective water sorbents for multiple applications, 3. $CaCl_2$ solution confined in micro- and mesoporous silica gels: Pore size effect on the ‘solidification-melting’ diagram,” *React. Kinet. Catal. Lett.*, vol. 61, no. 1, pp. 147–154, 1997.

[11] A. Jabbari-Hichri, S. Bennici, and A. Auroux, "$CaCl_2$ -containing composites as thermochemical heat storage materials," *Sol. Energy Mater. Sol. Cells*, vol. 172, no. July, pp. 177–185, 2017.

[12] Y. Aristov, M. Tokarev, L. Gordeeva, V. Romannikov, Y. Pankrat, I. Glaznev, G. Echevsiy, "New Composite Sorbent "$CaCl_2$ in Mesopores of MCM-41 " For Sorption Cooling / Heating," 2000, pp. 98–103.

[13] I. Glaznev, I. Ponomarenko, S. Kirik, and Y. Aristov, "Composites $CaCl_2$ / SBA-15 for adsorptive transformation of low temperature heat : Pore size effect," *Int. J. Refrig.*, vol. 34, no. 5, pp. 1244–1250, 2011.

[14] E. Courbon, P. D'Ans, A. Permyakova, O. Skrylnyk, N. Steunou, M. Degrez, M. Frère, "Further improvement of the synthesis of silica gel and $CaCl_2$ composites: Enhancement of energy storage density and stability over cycles for solar heat storage coupled with space heating applications," *Sol. Energy*, vol. 157, no. September, pp. 532–541, 2017.

[15] Y. N. Zhang, R. Z. Wang, and T. X. Li, "Experimental investigation on an open sorption thermal storage system for space heating," *Energy*, vol. 141, pp. 2421–2433, 2017.

[16] N. Yu, R. Z. Wang, Z. S. Lu, and L. W. Wang, "Study on consolidated composite sorbents impregnated with LiCl for thermal energy storage," *Int. J. Heat Mass Transf.*, vol. 84, pp. 660–670, 2015.

[17] L. Lavagna, D. Burlon, R. Nisticò, V. Brancato, A. Frazzica, M. Pavese, E. Chiavazzo, "Cementitious composite materials for thermal energy storage applications: a preliminary characterization and theoretical analysis," *Sci. Rep.*, vol. 10, no. 1, pp. 1–13, 2020.

[18] P. D'Ans, E. Courbon, A. Permyakova, F. Nouar, C. Simonnet-Jégat, F. Bourdreux, L. Malet, C. Serre, M. Frère, N. Steunoub, "A New Strontium Bromide MOF Composite with Improved Performance for Solar Energy Storage Application," *J. Energy Storage*, vol. 25, pp. 1–14, 2019.

[19] S. Hongois, F. Kuznik, P. Stevens, and J. J. Roux, "Development and characterisation of a new $MgSO_4$-zeolite composite for long-term thermal energy storage," *Solar Energy Materials and Solar Cells*, vol. 95, no. 7. pp. 1831–1837, 2011.

[20] M. Gaeini, A. L. Rouws, J. W. O. Salari, H. A. Zondag, and C. C. M. Rindt, “Characterization of microencapsulated and impregnated porous host materials based on calcium chloride for thermochemical energy storage,” *Appl. Energy*, vol. 212, no. May 2017, pp. 1165–1177, 2018.

[21] A. Shkatulov, R. Joosten, H. Fischer, and H. Huinink, “Core-Shell Encapsulation of Salt Hydrates into Mesoporous Silica Shells for Thermochemical Energy Storage,” *ACS Appl. Energy Mater.*, vol. 3, no. 7, pp. 6860–6869, 2020.

[22] R. Cuypers, A. J. Jong, J. Eversdijk, H. van ‘t Spijker, H. Oversloot, B.L.J Ingenhut, R.K.H Cremers, N.E. Papen-Botterhuis, “Microencapsulation of Salts for Enhanced Thermochemical Storage Materials R.,” in *40th Annual Meeting and Exposition of the Controlled Release Society*, 2013, pp. 1–2.

[23] Y. E. Milián, A. Gutiérrez, M. Grágeda, and S. Ushak, “A review on encapsulation techniques for inorganic phase change materials and the influence on their thermophysical properties,” *Renew. Sustain. Energy Rev.*, vol. 73, no. January, pp. 983–999, 2017.

[24] D. Zhu, H. Wu, and S. Wang, “Experimental study on composite silica gel supported $CaCl_2$ sorbent for low grade heat storage,” *Int. J. Therm. Sci.*, vol. 45, no. 8, pp. 804–813, 2006.

[25] H. Oh, S. Lim, J. H. Kim, and C. Lee, “Adsorption Equilibria of Water Vapor on an Alumina/Zeolite 13X Composite and Silica Gel,” *J. Chem. Eng. Data*, vol. 62, pp. 804–811, 2017.

[26] L. G. Gordeeva, J. Mrowiec-Bialon, A. B. Jarzebski, A. I. Lachowski, J. J. Malinowski, and Y. I. Aristov, “Selective water sorbents for multiple applications, 8. Sorption properties of $CaCl_2$ - SiO_2 SOL-gel composites,” *React. Kinet. Catal. Lett.*, vol. 66, no. 1, pp. 113–120, 1999.

[27] M. Tokarev, L. Gordeeva, V. Romannikov, and I. Glaznev, “New composite sorbent $CaCl_2$ in mesopores for sorption cooling / heating,” vol. 41, pp. 470–474, 2002.

[28] J. G. Ji, R. Z. Wang, and L. X. Li, “New composite adsorbent for solar-driven fresh water production from the atmosphere,” *Desalination*, vol. 212, no. 1–3, pp. 176–182, 2007.

[29] K. Hillier, “Methylcellulose,” in *xPharm: The Comprehensive Pharmacology*, S. J. Enna and D. B. Bylund, Eds. Elsevier, 2007, pp. 1–3.

[30] M. Robles and J. Gingerich, “PCT Application of Methylcellulose on Washcoats and Precious Metal,” 2016.

[31] Z. Moslehi, A. D. Garmakhany, M. Araghi, and M. Moslehi, “Effect of methylcellulose coating on physicochemical properties, porosity, and surface diameter of pistachio hull,” *Food Sci. Nutr.*, vol. 3, no. 4, pp. 355–361, 2015.

[32] T. L. Rogers and D. Wallick, “Reviewing the use of ethylcellulose, methylcellulose and hypromellose in microencapsulation. Part 1: Materials used to formulate microcapsules,” *Drug Dev. Ind. Pharm.*, vol. 38, no. 2, pp. 129–157, 2012.

[33] K. G. Wu, X. H. Chai, and Y. Chen, “Microencapsulation of fish oil by simple coacervation of hydroxypropyl methylcellulose,” *Chinese J. Chem.*, vol. 23, no. 11, pp. 1569–1572, 2005.

[34] Y. Hua, A. Godin, and F. H. Tezel, “Water Vapor Adsorption In Silica Gel For Thermal Energy Storage Application,” *Adv. Mater. Lett.*, vol. 10, no. 2, pp. 124–127, 2019.

[35] Köll, W. van Helden, G. Engel, W. Wagner, B. Dang, J. Jänchen, H. Kerskes, T. Badenhop, T. Herzog, “An experimental investigation of a realistic-scale seasonal solar adsorption storage system for buildings,” *Sol. Energy*, vol. 155, pp. 388–397, 2017.

[36] R. van Alebeek, L. Scapino, M. A. J. M. Beving, M. Gaeini, C. C. M. Rindt, and H. A. Zondag, “Investigation of a household-scale open sorption energy storage system based on the zeolite 13X/water reacting pair,” *Appl. Therm. Eng.*, vol. 139, no. November 2017, pp. 325–333, 2018.

[37] Y. Hua, B. Ugur, and F. Handan Tezel, “Adsorbent screening for thermal energy storage application,” *Sol. Energy Mater. Sol. Cells*, vol. 196, no. December 2018, pp. 119–123, 2019.

Chapter 6 – Conclusions

6.1 Abbreviations

ESD	Energy storage density
RH	Relative humidity
SE	Specific energy
TCES	Thermochemical energy storage
Ti-Si	Titanium silicate molecular sieve

6.2 General Conclusions

Renewable thermal energy technology plays an important role in supplying the global energy demand. As such the temporal mismatch between thermal energy supply and demand needs to be resolved. Implementing thermal energy storage technologies would allow for excess renewable energy and other waste heat to be stored and used rather than wasted, resolving said mismatch.

Conventional storage methods are impractical for large-scale commercialization due to their low energy density, their inability to store energy long-term, and their use of toxic materials. Thermochemical (TCES) systems offer high energy storage densities, no need for toxic chemicals, and are suitable for long-term energy storage. This technology is promising but is still in its infancy and needs to be explored further. Suitable materials need to be developed and the effects of operating conditions need to be determined at different scales.

This thesis has focussed on material development and operating parameter optimization. A screening study was performed to determine which materials are best suited for this application. The effects of particle size, flow rate, humidity, regeneration temperature, and insulation were quantified and optimized. Finally, hygroscopic salt-based composites were synthesized and modified to realize high stability and high energy storage performances.

The energy storage density, thermal power, cyclic stability, and mechanical durability of titanium silicate molecular sieve (Ti-Si), flax shive briquettes, MCM-41, SAPO-34, and silica gel was tested using a lab-scale energy storage apparatus and a standard drop test. All materials were either received as granular materials or were pelletized so that they could be used in a fixed-bed adsorption column. All materials showed excellent mechanical durability in the drop test, except for SAPO-34 and flax shives. The SAPO-34

pellets lost 15% of their initial mass after being dropped 4 times from 1.85 m onto a metal plate and the flax shive briquette pieces lost 35% of their initial mass. This suggests that there may be practical issues during material handling or use if these densification processes are used. Therefore, alternative pelletization methods should be considered for these materials. Silica gel and SAPO-34 showed high energy densities (>150 kWh/m^3) at moderate and high relative humidity (RH) levels and MCM-41 showed a high energy density at humidity levels above 70% RH. Silica gel, SAPO-34, and MCM-41 underwent more than 20 cycles and exhibited excellent cyclic stability. Of the tested materials, silica gel, SAPO-34, and MCM-41 seemed most suitable for thermochemical energy storage applications. SAPO-34 would be particularly useful in applications where highly humid air is not available. MCM-41 would be best suited for applications where high humidity air is available, but a high temperature regeneration source is not available. Silica gel would be well suited to applications where cost is an important factor since it is the least expensive adsorbent, it is commercially available, and it demonstrated high performance. Furthermore, all materials could potentially act as host materials for hygroscopic salt impregnations.

The operating parameters of an open silica gel/water vapour adsorption energy storage system were analysed and optimized. The effects of particle size, flow rate, pressure drop, inlet relative humidity, regeneration temperature, and insulation were quantified and optimized using a one-factor-at-a-time method. As the particle size decreased, the saturation time decreased and the pressure drop increased. The energy storage density (ESD), maximum temperature lift, and thermal power were nearly proportional to the inlet relative humidity in the range of 10-90% RH. This essentially follows the trend of the silica gel isotherm. Increasing the inlet relative humidity increases the adsorption rate, but it also increases the maximum water uptake capacity. This resulted in a local maximum for saturation time at around 50% relative humidity. Increasing the regeneration temperature increases the number of free sites for adsorption to take place. This increases the silica gel working capacity and therefore its energy storage density. Increasing the regeneration temperature beyond 120°C showed no increase in performance. The air flow rate correlated linearly with the thermal power. Increasing the air flow rate in the range of 0-15 SLPM increased the energy storage density and temperature lift values but increasing the flow rate beyond 15 SLPM had minimal effects. Increases in air flow rate also reduced saturation times. Under optimal conditions, an energy storage density of 200.7 kWh/m^3 was achieved with a maximum temperature lift of 28.5°C. This is approximately double the typical values reported in literature for silica gel/water-vapour systems, thus emphasizing the importance of optimizing system operating parameters.

$MgSO_4$ is a hygroscopic salt with a high deliquescence relative humidity. Four host materials were impregnated with $MgSO_4$. All four of these materials were stable after three hydration and dehydration cycles. Of these four composites, silica gel impregnated with $MgSO_4$ had the best energy storage performance when tested with a lab-scale energy storage apparatus. Since the silica gel/$MgSO_4$ sample had the highest performance, multiple samples were synthesized with different amounts of $MgSO_4$ in order to examine the effects of salt concentration on energy storage performance and material structure. SEM characterization showed that there was a homogeneous distribution of the salt on the silica gel surface and the EDX showed that as the salt concentration increased, there was a greater deposition of $MgSO_4$ on the surface of the silica gel. It was found that as the salt content increased, the specific energy (SE) decreased; no composites had higher SE values than pure silica gel. However, the energy storage density and maximum thermal power, which are the product of the material bulk density and the SE, were at an optimum when 15 g of $MgSO_4$ was added to 30 g of silica gel.

$CaCl_2$, a hygroscopic salt that is well-suited to thermochemical energy storage applications, was stabilized via impregnation and encapsulation techniques. Three methods of stabilization were attempted: $CaCl_2$ impregnation in silica gel, encapsulation of $CaCl_2$ in methylcellulose, and simultaneous impregnation of $CaCl_2$ in silica gel and encapsulation by methylcellulose. All three composites were tested using a lab-scale energy storage apparatus to determine their stability after multiple hydration/dehydration cycles and to determine their energy storage performance. The silica gel impregnated with $CaCl_2$ had a high energy storage performance during the first hydration cycle, but its performance rapidly decreased in the subsequent two cycles. The $CaCl_2$ that was encapsulated with methylcellulose had a high energy storage performance and was stable for 3 hydration and dehydration cycles, but the material experienced some swelling and agglomeration issues. Finally, the $CaCl_2$ impregnated silica gel that was simultaneously encapsulated in methylcellulose experienced a high energy storage performance (ESD = 241 kWh/m^3 & SE = 630 Wh/kg), was stable after 3 hydration/dehydration cycles and did not exhibit practical issues. This connotes that the simultaneous impregnation and encapsulation method can result in low-cost composites with high stability and performance. LiCl-based composites were also synthesized and tested, but because of swelling, deliquescence, and particle agglomeration, the flow through the sorption column was blocked during testing, making it impossible to test these materials using the same testing apparatus.

6.3 Recommendations

Thermochemical energy storage technology is promising but not commercially ready. To improve commercial readiness material development should continue, with an emphasis on hygroscopic salts and salt-in-matrix composites with inexpensive hosts and salts. This is because these materials have exhibited high energy storage performance and stability under a range of operating conditions. It is also necessary to continue improve the stability of these materials, since many of them have shown to decrease in energy storage performance or have practical issues after multiple hydration/dehydration cycles. Encapsulation with polymeric coatings is one technique that has shown positive results, but other stabilization methods, including encapsulation with other encapsulating agents, should also be explored. Pilot and demonstration-scale systems need to be built and tested thoroughly through both sensitivity analysis and practical operations. This will give the academic community and technologists a better understanding of how these systems are expected to behave at the commercial scale and will provide important insights for material development, system design, and techno-economic assessment.

Appendix A. Study of energy density of adsorption-based thermal energy storage system under different operating conditions for SAPO-34

Ye Carrier, University of Ottawa

Curtis Strong, University of Ottawa

Dominique Lefebvre, University of Ottawa

F. Handan Tezel, University of Ottawa

Abstract

The water vapor and the silico-alumino-phosphate (SAPO-34) material has been recognized to be one of the better adsorbate-adsorbent pairs for the packed-bed adsorptive thermal energy storage (TES) systems for space heating applications. In this paper, operating conditions including the system construction materials selection, cooling methods of the system after regeneration, relative humidity (RH) of inlet air, and packed-bed regeneration temperatures have been examined for the TES system performance evaluation and process design optimization purposes.

Keywords: Thermal energy storage, adsorption, water adsorption from air, optimization of operating conditions

Accepted to be published in Journal "Adsorption"

Nomenclature

Cg_{inlet}	Inlet water vapor concentration (mol/m^3)
Cp	Heat capacity of the moist air (kJ/kg·K)
P_{atm}	Atmosphere pressure (101.325 kPa)
P_{inlet}	Total pressure measured (kPa) at column inlet hygrometer
P_{sat}	Saturated water vapor pressure (kPa) at temperature TH_{inlet}
q	Adsorption capacity (mol/kg)
R	Gas constant (8.3145 J/mol·K)
RH_{inlet}	Inlet relative humidity measured (%) at inlet hygrometer
ΔT	Temperature difference (K) between the column inlet and outlet
TH_{inlet}	Temperature measured (K) at column inlet hygrometer
V	Volume of the packed bed column (cm^3)
v_m	Mass flow rate (kg/s) of the moist air

Abbreviations

AC	Air cooling
AHT	Adsorptive heat transformation
BET	Brunauer-Emmett-Teller
IC	Isolated cooling
MFC	Mass flow controller
MOF	Metal organic framework
PC	Polycarbonate
RH	Relative humidity
SAPO	Silico-alumino-phosphate
SLPM	Standard liter per minute

SS Stainless steel

TES Thermal energy storage

1. Introduction

Due to the increasing concerns about the climate change and environmental impact of fossil fuels, researchers around the world have been turning their attention to the development of renewable energy technologies in transition to a low-carbon economy. However, the renewable energy sources (e.g. wind power and solar energy) has the major constraint of intermittency and lack of consistency. Therefore, it is essential to develop energy storage technologies to balance the misalignment between the energy supply and demand, and create a more flexible and reliable energy system [1]. There are five main categories of energy storage systems that have been widely accepted and deployed around the world: chemical, electrochemical, electrical, mechanical, and thermal energy storage [2]. Thermal energy storage (TES) systems have received a great deal of interest by offering the option to improve the output control for both traditional and renewable energy sources using low cost accessible storage materials such as water and natural adsorbents [3]. According to European Commission, the heating and cooling in buildings and industry is responsible for about 51% of the total final energy consumption in European countries. And the space heating accounts for up to 76% of end-uses energy consumption in the residential sector [4]. Due to the cold climate in Canada, space heating and domestic water heating accounts for 63% and 19% of the energy consumptions in residential sector, with natural gas being the main sources of energy used [5]. Besides improving the energy efficiency of the heating and cooling systems, technology innovation of adsorptive heat transformation (AHT) such as the adsorptive chillers/heat pumps [6-7], or adsorption-based TES systems can play a key role in the reduction of global greenhouse gas emission and the transformation to more sustainable energy future [3, 8-9].

The performance of a TES system strongly depends on the nature of the adsorbate-adsorbent pair chosen in the system [10], and the design of an effective adsorption system mainly relies on the accurate experimental data of the adsorption equilibria, kinetics, and heat of adsorption [11]. Various adsorbates such as water, ammonia, carbon dioxide, alcohol (e.g. methanol, ethanol, etc.) in pair with different types of adsorbent materials including zeolite [9, 12], activated alumina, activated carbon [13], metal organic frameworks (MOFs), silica gel and other mesoporous silicate [14-15], and other hybrid porous materials [7, 16 -18] have been studied for their TES performances [8, 10, 19–21-23]. Among all the adsorbate-

adsorption pairs, water vapor and the silico-alumino-phosphate (SAPO)34 has been considered to be one of the more attractive options considering the easy-access and environmentally friendly nature of the adsorbate, and the thermal-stability and the high adsorption capacity of the adsorbent material [24]. Although the synthesis methods, pore architecture modification, water vapor adsorption isotherms, coating methods and the application in thermal heat pump for SAPO-34 material have been well studied in the literature [21, 24–30], the performance of the adsorbent in the packed bed adsorption TES system has not been evaluated from the breakthrough experiments in response to different operation conditions. In this paper, the SAPO-34 powdered material was pelletized and filled into cylindrical packed beds constructed with different materials for breakthrough experiments using two different cooling methods in order to evaluate how the inlet relative humidity (RH) and regeneration temperature affect the system's energy densities.

2. Material and Experimental Methods

2.1 Material Properties

The original powder-form SAPO-34 molecular sieve material was purchased from ACS Material LLC. (Medford, MA, USA). It was then pelletized to small spherical pellets (with 1-2mm diameter) by Material Center at Dresden University of Technology in Dresden, Germany. The spherical SAPO-34 pellets were used in packed bed columns as adsorbent material for all the thermal energy storage experiments discussed in this paper.

The N_2 adsorption isotherms at 77K of the original powder sample and the pellets were measured using the 3 Flex Physisorption – Surface Characterisation Analyzer at Centre for Catalysis Research and Innovation (CCRI) at University of Ottawa. The original SAPO-34 powder and pellet materials showed Brunauer-Emmett-Teller (BET) surface area of 612.5 m^2/g and 589.2 m^2/g, respectively. And the t-plot pore volume of the original SAPO-34 powder and pellet materials were calculated to be 0.291 and 0.283 cm^3/g, respectively. Pelletizing process and adding small amount of inorganic binder materials to the pellets has little effect on the material's porosity properties as they only decreased the BET surface area of the material by 3.8% and the pore volume by 2.7%.

2.2 Water Vapor Isotherms

The water vapor adsorption isotherms of the SAPO-34 pellet material at 293.15K (20^{o}C) were measured using the BELSORP-max instrument (MicrotracBEL, Osaka, Japan) in the Materials Surface Characterization Laboratory of the Chemical Engineering Department at University of New Brunswick. The adsorbent was regenerated at 200^{o}C before adsorption isotherm measurements were taken. The instrument obtained the adsorption equilibrium data at different pressures by adding small amount of water vapor to the sample chamber incrementally. The adsorbed amount of water vapor (mol/kg) at different pressure (between zero to about 2.3 kPa at 293K) were determined automatically by the instrument.

2.3 Experimental Setup

A thermal energy storage experimental system using packed bed adsorption column was designed and built in our lab at University of Ottawa. Figure A-1 shows the schematic diagram of this system. Pelletized SAPO-34 materials were packed in an adsorption column (either column A or column B). The dimensions and properties of the packed bed columns are presented in Table A-1. The original SAPO-34 powder material is stable up to 900K regeneration temperature [24, 25]. The SAPO-34 pellets with inorganic mineral based binder material are stable up to 473K (200^{o}C) according to the pelletizing service supplier. Two columns designed with the same size (63 cm^{3}) were custom made for experiments with different regeneration temperatures. Small variation of the column size was cause by the use of standard parts in the column assembly. Stainless steel column was used in experiments with higher regeneration temperature (> 80^{o}C), while the polycarbonate column has been used in experiments with lower regeneration temperature (< 80^{o}C) due to the stability of the column material.

Experiments were performed at a selected range of relative humidity values and regeneration temperatures to study the effects of operating conditions on the energy density of packed bed TES system. A detailed description of the experimental setup and procedure can be found in our previous publications [15, 17]: compressed air provided by the engineering research facility passes through an oil filter to remove any impurities before connecting to the thermal energy storage experimental system in the lab. The compressed air is then split into the dry and wet streams, using mass flow controllers (MFC, Alicat MCR Mass Flow Controller, Alicat Scientific, Tucson, AZ, USA) to control the flow rate of air inside each stream. The air in the dry air stream is further dried (to less than 2% relative humidity at room temperature) by passing a drying column filled with desiccants. The wet air stream first passes through a

bubbler (which is able to humidify the air stream to about 60% RH at room temperature), with an ultrasonic fogger installed inside (which is to further humidify the air to about 96% RH at room temperature). By adjusting the flow rates of the dry and wet air streams, a moist air mixture with desired flow rate and RH can be obtained. A total flow rate of 24 standard liter per minute (SLPM) were used in all breakthrough experiments since this flow-rate was determined to show the highest energy density based on our previous research [18].

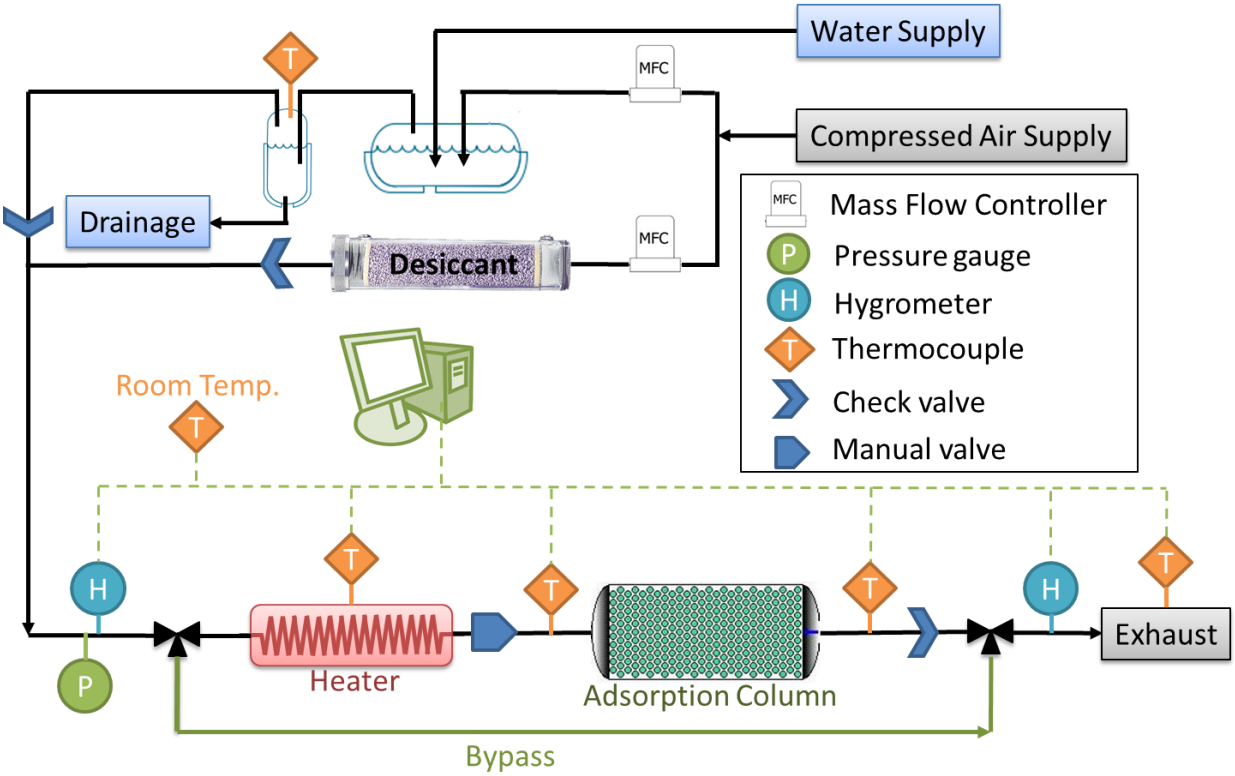

Figure A-1. Schematic diagram of the thermal energy storage experimental system used in this study.

Table A-1. The materials and dimensions of the packed bed columns used in this study.

Column	A	B
Construction Material	Stainless steel (SS)	Polycarbonate (PC)
Column Length (cm)	7.13	8.20
Column inner diameter (cm)	3.35	3.17
Column outer diameter (cm)	3.82	3.81
Column volume (cm^3)	62.84	64.92
Packed SAPO-34 adsorbent weight (g)	35.80	41.67

The column inlet and outlet relative humidity (RH) values and temperature were measured using two digital hygrometers (HX15 High Temperature Relative Humidity/Temperature Transmitter, Omega Environmental, St-Eustache, QC, Canada). A pressure gauge was also installed as close as possible to the inlet hygrometer position in the system to measure the pressure (P_{inlet}) in the system, which provided accurate information on the pressure drop between the two hydrometer's positions in the system as well. The temperature in the lab, at the inlet and the outlet of the column, at heater skin, and the gas exhaust of the TES system were monitored and recorded throughout each experiment using Transition Junction Style Thermocouple Probes (Model: TMTSS-062G-6, Omega Environmental, St-Eustache, QC, Canada). All the temperature and relative humidity data were recorded automatically every 10 seconds during the experiments using the LabVIEW program.

An electronic three-way valve is installed before the heater to direct the moist air to the by-pass pathway (to by pass the heater and the adsorption column) during the setting up period before experiments, or the packed column pathway during the adsorption process. And a check valve is installed at the outlet of the column to prevent any air back flow. Compared to the experimental setup in our previous publications, a manual valve has been added recently between the heater and the adsorption column to isolate the packed column during the isolated cooling (IC) process. The reason for this system modification and experimental results are discussed in section 3.1 of this paper.

3. Results and Discussion

Typical breakthrough curves during adsorption experiments are shown in Figure A-2. It should be noted that the RH reading from the hygrometer is proportional to the pressure at the measuring point. Due to the pressure drop caused by the tubing, valves, and heater in the TES experimental setup, the value of the column inlet RH recorded by the hygrometer installed before the packed bed column is higher than the RH value measured at atmospheric pressure (P_{atm}) at the column outlet. See Figure A-3 for the comparison of the RH values recorded by hygrometers at column inlet and outlet during a typical experiment for TES. As can be seen in this figure, they do not converge to each other at the end of the breakthrough curve, due to the pressure difference at which these relative humidities are measured. Therefore, it is more reasonable to use the concentrations of the water vapor at the inlet and outlet of the column for comparison for the breakthrough curves, as opposed to the RH values recorded by the hygrometers. The actual water vapor concentration at the inlet of the column can be calculated using Eq. A.1 based on the ideal gas law, assuming that the pressure drop in the column is very small, which has been experimentally proven to be the case:

$$Cg_{inlet} = \frac{P_{sat} \cdot RH_{inlet} \cdot \frac{P_{atm}}{P_{inlet}}}{R \cdot TH_{inlet}} \quad \text{(A.1)}$$

Where Cg_{inlet} is the column inlet water vapor concentration (mol/m^3), P_{sat} is the saturation vapor pressure of water (kPa) at temperature TH_{inlet}, TH_{inlet} is the temperature (K) at the inlet hygrometer position where the inlet relative humidity is measured, RH_{inlet} is the relative humidity, in fraction value, provided by the inlet hygrometer, P_{inlet} is the total pressure measured at the inlet hygrometer position (kPa), P_{atm} is the atmospheric pressure (101 kPa) at the outlet of the column and R is the gas constant (8.3145 J/mol·K).

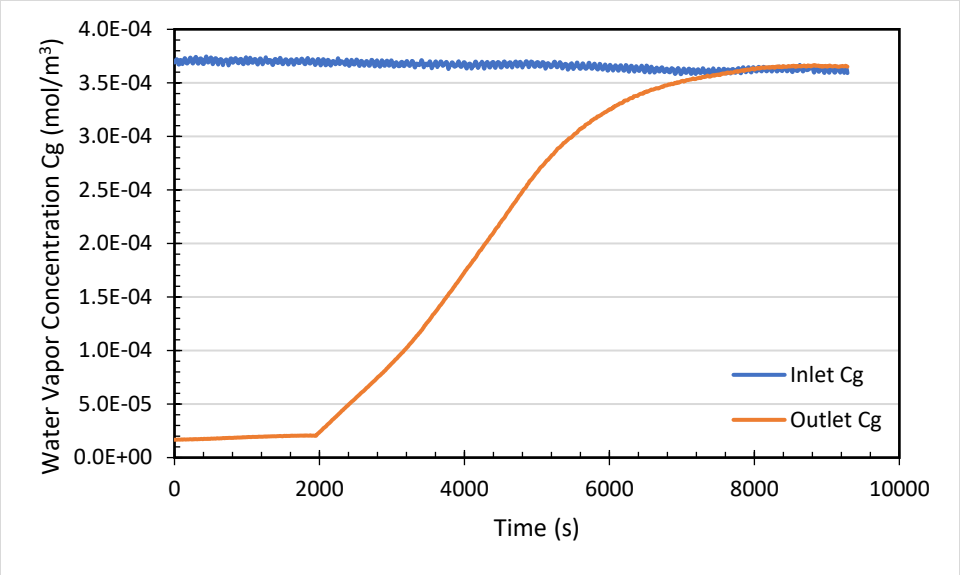

Figure A-2. Breakthrough curve observed for SAPO-34 using calculated water vapor concentration at column inlet and outlet after 80°C regeneration temperature at 50% inlet RH.

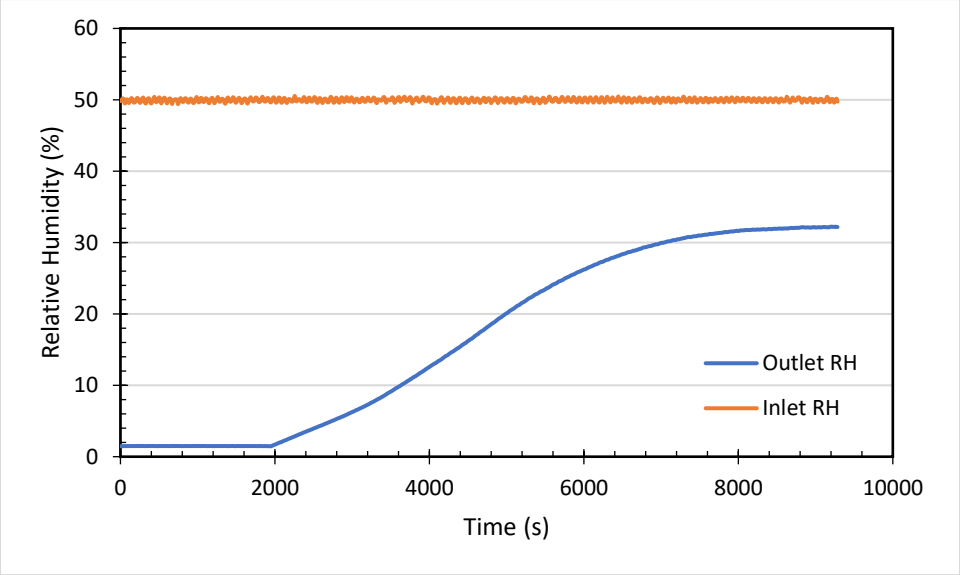

Figure A-3. Breakthrough curve using RH values recorded by column inlet and outlet hygrometer after 80°C regeneration temperature and 50% inlet RH.

The experimental energy density of the packed-bed column can be calculated from the concentration and temperature breakthrough curves for each experiment using Eq. A.2:

$$\text{Experimental Energy Density} = \frac{\int_0^t (v_m \times Cp \times \Delta T)\, dt}{V} \quad \text{(A.2)}$$

where v_m is the mass flow rate (kg/s) of the moist air passed through the column. It is calculated by adding the wet and dry air mass flow rates measured by the mass flow controllers (MFCs) at the inlet of the column. *Cp* is the heat capacity of the moist air (kJ/kg·K) inside the packed bed column; *ΔT* is the temperature difference (K) between the column inlet and outlet obtained from the temperature breakthrough data (see Figure A-4); and *V* is the volume of the packed bed column used in the experiments.

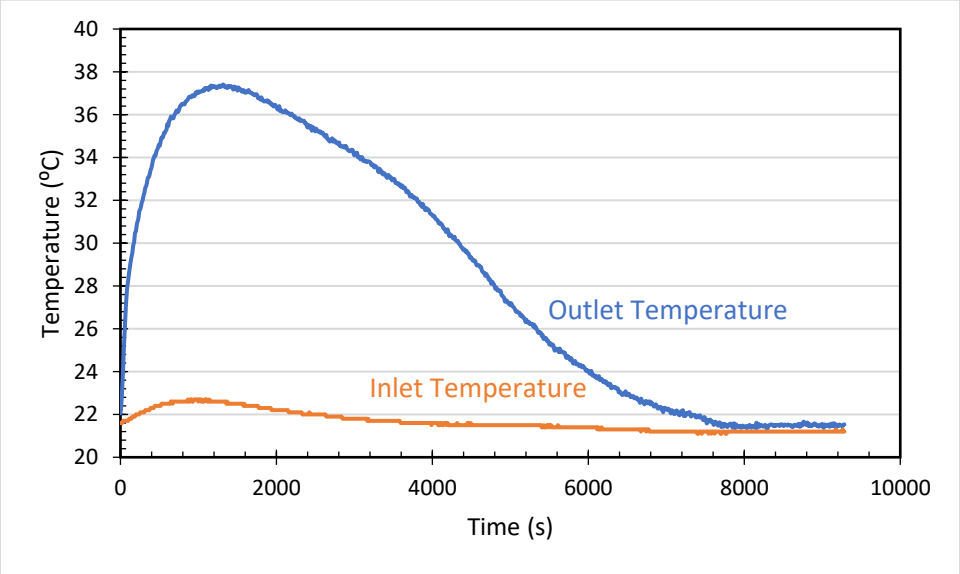

Figure A-4. Column inlet and outlet temperature breakthrough curves for SAPO-34 showing their change during the adsorption after 80°C regeneration temperature at 50% inlet RH

3.1 Effect of Cooling Method

Air cooling (AC) method has been used for most of the experiments as described in our previous publications [17, 15]: the stainless steel columns packed with SAPO-34 pellets were regenerated at constant regeneration temperature (i.e. at 80°C, 100°C, 120°C, 140°C, 160°C and 180°C column inlet temperature) with 24 SLPM (L/min at standard condition) hot dry air flow. Once the outlet relative humidity equals the inlet relative humidity (close to zero), and the outlet column temperature stays the same for half an hour or so, the column was considered to be fully regenerated at given regeneration

condition and the heater was turned off. The heated column and the SAPO-34 adsorbent inside the column were then cooled down with the room temperature dry air flow through the column.

Figure A-5 shows the effect of regeneration temperature on energy density observed for SAPO-34 in SS column with 90 % RH at the inlet for both air cooling (AC), as well as the isolated cooling (IC) after regeneration of the column. As shown in this figure, in the case of AC, the calculated energy density increases from 127 kWh/m^3 to 140 kWh/m^3 as the regeneration temperature increases from 80^{o}C to 100^{o}C. However, the energy density then decreases as the regeneration temperature further increases from 100^{o}C to 180^{o}C, which is the opposite trend of what we expected. The residual water inside the SAPO-34 material decreases as the regeneration temperature increases, which enable the adsorbents to have higher adsorption capacities after regeneration at higher temperatures. Since adsorption is an exothermic process, higher energy densities should be observed for experiments with higher regeneration temperatures.

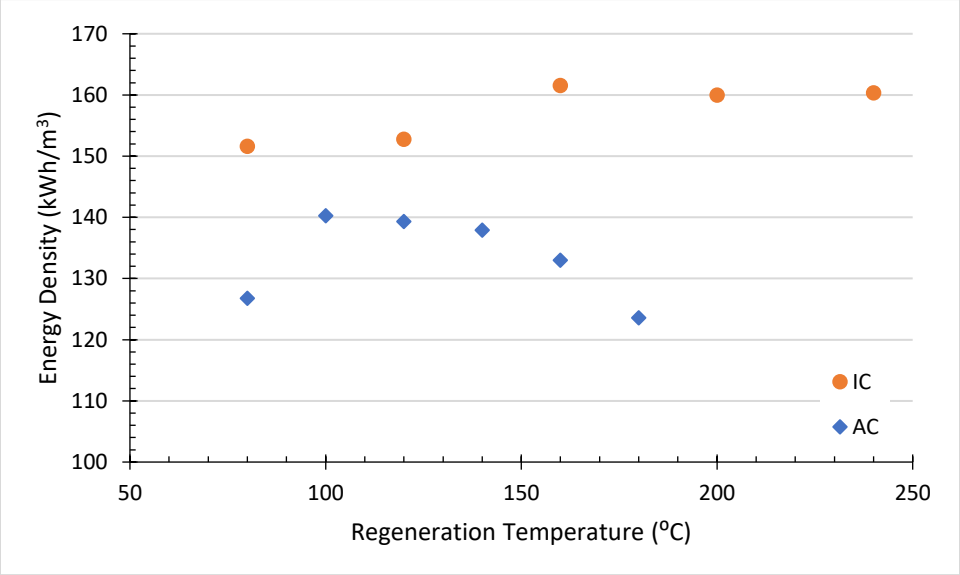

Figure A-5. Energy density of SAPO-34 material regenerated at different temperatures with 90% inlet RH operation condition using air cooling (AC) and isolated cooling (IC) method for SS column.

After re-evaluating the experimental design, as well as observing the results obtained in Figure A-5 for AC, a conclusion has been drawn that the adsorption capacity loss at higher regeneration temperatures was caused by the adsorption of the residual amount of moisture in the dry air stream passing through the

column during the air-cooling process. During the AC process, cooling air from the dry air stream continuously passed through the column after the regeneration (i.e. heater has been turned off) until the column was cooled back to room temperature and ready for the next experiment. Even though the cooling air provided by the facility has passed through a drying column before entering the packed-bed column, there was still a trace amount of moisture (about 1-2% RH at room temperature) left in the air stream. Higher regeneration temperature means longer cooling time before the starting of the subsequent adsorption experiment, which resulted in more moisture in the dry air stream being exposed and therefore being adsorbed in the "already regenerated" column. Therefore, less adsorption capacity was available in the column, which resulted in observed lower energy density values for column regenerated at higher temperatures.

To preserve the adsorption capacity and obtain the results that truly reflect the thermal energy storage ability of the material using the existing experimental setup, a manual valve was installed between the heater and the packed-bed adsorption column and the isolated cooling (IC) method was used for all the experiments going forward. For experiments using isolated cooling method, once the column was considered to be fully regenerated at given regeneration conditions (i.e. the outlet relative humidity equals the inlet relative humidity and the outlet column temperature stays the same for half an hour or so), the heater was turned off, as well as the dry air stream and the manual valve. No air or moisture passed through the column during the cooling period. The adsorption column and the SAPO-34 material inside was then "isolated" from the rest of the TES experimental system and the surrounding environment by the manual valve before the column inlet and the check valve at the column outlet. The column and SAPO-34 adsorbent inside were cooled down from regeneration temperature to room temperature by the heat loss through the column wall to the surrounding environment solely during the isolated cooling (IC) period, without any flow through the column.

Without the adsorption capacity loss during the cooling time by using the isolated cooling (IC) method, an increase in the calculated energy density of 10-20% (depending on the regeneration temperature) was observed (see Figure A-5) compared to the energy density observed from the data for the experiments using air cooling (AC) method. Experimental system energy density as high as 160 kWh/m^3 was obtained with regeneration temperature higher than 160^{o}C. Therefore, isolated cooling method is recommended for TES process design for the benefits of lower power input (i.e. dry air pumping) and higher energy output (i.e. system energy density) if the longer cooling time is not a concern.

3.2 Effect of Column Construction Material and Adding Insulation

Two columns have been custom made and used in the experiments to compare the heat loss and the energy density of the SAPO-34 adsorbent. The materials and the dimensions of the columns are listed in Table A-1. Three layers of 1/8 inch thick high-temperature ceramic fiber pipe insulation (McMaster-Carr, Elmhurst, Illinois, US) was used to wrap around the columns to examine how adding insulation affects the energy density of the TES system using SAPO-34 packed adsorption column.

Figure A-6 the effect of column material, as well as the effect of insulation on energy density. With the same regeneration temperature (80^{o}C), TES system using polycarbonate column with insulation showed the highest system energy density, while the one using stainless steel column with insulation showed the lowest energy density. Adding insulation has positive effects on the energy density, but the difference was not significant: adding insulation to polycarbonate column only increases the energy density by 8%. For a TES system for low temperature regeneration heat source (less than 100^{o}C), cheaper material such as polycarbonate is a better option than stainless steel or other metal materials for its lower cost and higher energy density obtained (lower heat loss due to lower thermal conductivity). Up to 20% higher energy density was obtained from the TES system using PC column with insulation compared to the one using SS column with insulation.

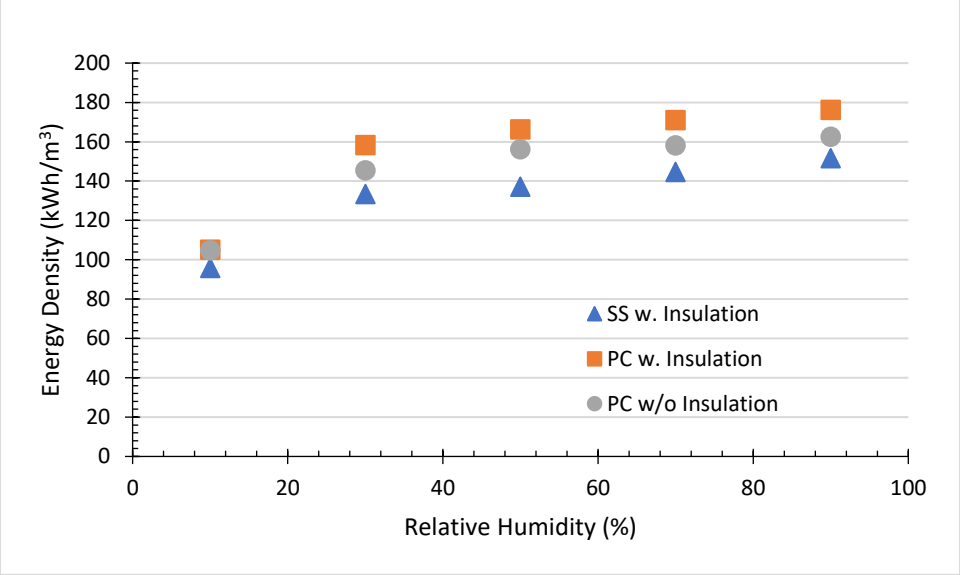

Figure A-6. Energy density comparison of columns packed with SAPO-34 pellets regenerated at 80^{o}C with different inlet RH: stainless steel column with insulation; polycarbonate column with insulation; and polycarbonate column without insulation.

3.3 Effect of Regeneration Temperature

As mentioned earlier, higher regeneration temperatures should result in higher TES system energy densities. This hypothesis has been confirmed with experimental results in this study, as can be seen in Figure A-7 and Figure A-8. Increasing regeneration temperature from 60°C to 80°C can increase the energy density by 3-8% as demonstrated in Figure A-7 using polycarbonate column with insulation.

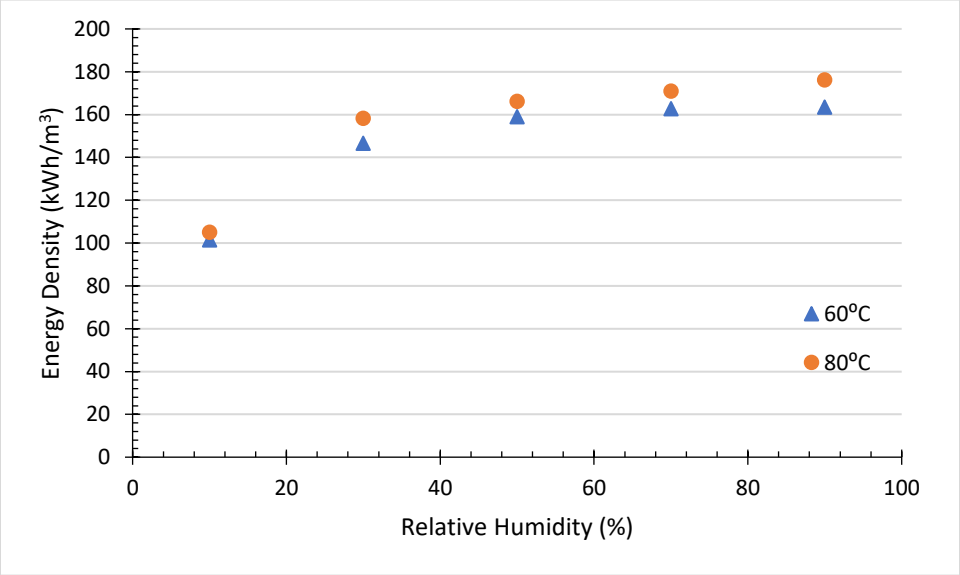

Figure A-7. Energy density comparison of polycarbonate column with insulation packed with SAPO-34 pellets for different inlet RH after regeneration temperatures of 60 and 80°C.

Similarly, as can be observed in Figure A-8, increasing regeneration temperature from 80°C to 240°C for SAPO-34 adsorbent can increase the experimental energy density by 11% with 10% inlet RH, and only 4-6% for 30-90% inlet RH range using SS columns with insulation in the TES system. Considering the +/- 2% RH accuracy of the hygrometer at room temperature, the impact of regeneration temperature on the system energy density seems negligible, and the fluctuation of the observed energy density for different regeneration temperatures could be considered to be the inaccuracy introduced by the thermocouples and hygrometers. The average energy densities at different inlet RH using different column materials at different regeneration temperature ranges were listed in Table A-2 for comparison.

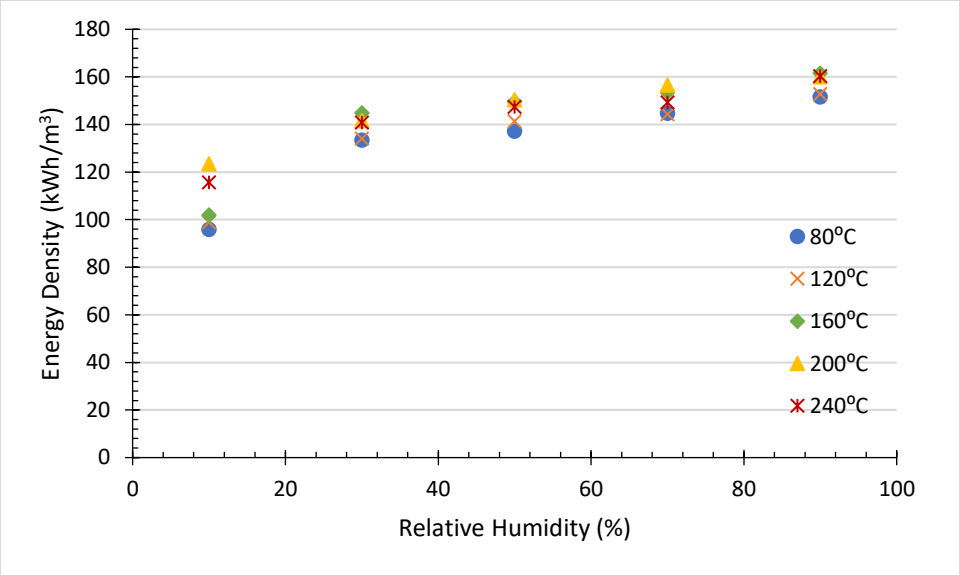

Figure A-8. Effect of inlet RH on energy density for stainless-steel column with insulation packed with SAPO-34 pellets after regeneration at different temperatures from 80 to 240°C.

Table A-2. Comparison of the average energy density at different inlet RH values using different column material at different regeneration temperature ranges

	Average energy density (kWh/m³) at				
Inlet RH (%)	10	30	50	70	90
PC column with insulation at 60-80°C regeneration temperature	103.29	152.42	162.65	166.95	169.90
SS column with insulation at 80-240°C regeneration temperature	107.14	138.96	145.17	149.68	157.26

3.4 Effect of Inlet Air Relative Humidity

As shown in Figure A-6 to Figure A-8 and Table A-2, the inlet relative humidity is another important factor that affects the energy density of the SAPO-34 material: the energy density increases with the inlet RH. When the inlet RH increases from 10% to 30%, the energy density increased by 44% and 51% after 60°C and 80°C regeneration temperatures, respectively, using polycarbonate column with insulation (see Figure A-7). However, increasing the inlet RH from 30% to 90% using the same column, the energy density only increased 11% for both 60°C and 80°C regeneration temperatures. The experiments using SS column

with insulation shows similar results: increasing the inlet RH from 10% to 30% can increase the energy density by 15-42% depending on the regeneration temperature, while increasing the inlet RH from 30% to 90% only increased the energy density by 12-14%. This phenomenon can be explained by the SAPO-34 isotherm data.

Figure A-9 shows the comparison of the water vapor adsorption isotherm after regeneration at 200^{o}C, with the amount adsorbed calculated from the breakthrough curves at different relative humidity values after regeneration at 200^{o}C. The water vapor adsorption isotherm with SAPO-34 pellets exhibits a Type IV isotherm, and 10-90% RH fall into the plateau range of the isotherm curve, as can be seen from that figure. At RH range higher than 20%, increasing the pressure of the water vapor does not increase the adsorption capacity too much.

The outlier of the adsorption capacity (q) calculated from the 10% inlet RH breakthrough experiment in Figure A-9 was due to the long experimental time for the SAPO-34 pellets to reach saturation with the low inlet RH. Low inlet RH results in higher equipment inaccuracy (with +/- 2% accuracy level, hygrometers can introduce up to 20% inaccuracy at 10% RH) being included in the calculation of cumulative adsorbed amount of water vapor for the breakthrough results.

In summary, medium relative humidity is recommended for TES systems for long-term seasonal storage applications, because adding extra input energy to generate higher RH in the inlet air stream may not be able to makeup for the small increase in the energy released.

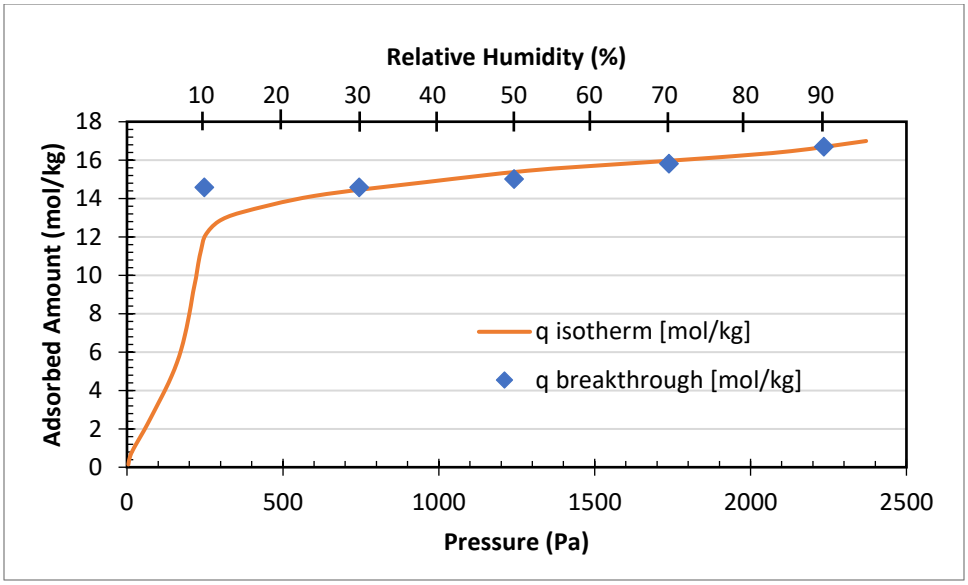

Figure A-9. Adsorption capacity of SAPO-34 pellets regenerated at 200°C calculated from water vapor adsorption isotherm at 20°C vs. calculated from breakthrough experiments with 10%, 30%, 50%, 70%, and 90% inlet RH at room temperature (about 21°C)

4. Conclusions

In this study, powdered SAPO-34 material was used. It was pelletized and was used to examine its performance of water vapor adsorption process for thermal energy storage application. System energy density as high as 176.23 kWh/m^3 can be achieved after regeneration at 80°C using polycarbonate column with 3 layers of insulation wrap with 90% inlet RH. Regeneration temperature higher than 120°C or RH higher than 30% do not seem to have strong influence on the improvement of energy density of the TES system using SAPO-34 and water vapor as the adsorbent-adsorbate pair. Considering the fact that SAPO-34 material showed higher energy density for TES application using packed-bed column in comparison to other adsorbent materials (e.g. silica gel [15], zeolite 13X and activated alumina [17]) at much lower regeneration temperature and inlet air RH, it would be a good candidate for this application. Cheaper material with lower thermal conductivity such as polycarbonate is recommended for the column construction material rather than metals (e.g. stainless steel, carbon steel, copper, aluminum, etc.). Selection of proper cooling method after material regeneration is another important factor to be considered in the TES system design: isolated cooling should be used instead of air cooling when time is not a constrain during an operation cycle (i.e. long-term / seasonal TES applications).

References

[1] J. Xu, R. Z. Wang, and Y. Li, "A review of available technologies for seasonal thermal energy storage," *Sol. Energy*, vol. 103, pp. 610–638, May 2014.

[2] M. S. Guney and Y. Tepe, "Classification and assessment of energy storage systems," *Renew. Sustain. Energy Rev.*, vol. 75, no. October 2016, pp. 1187–1197, 2017.

[3] A. Hauer, "Evaluation of adsorbent materials for heat pump and thermal energy storage applications in open systems," *Adsorption*, vol. 13, no. 3–4, pp. 399–405, 2007.

[4] European Commission, "Executive summary: Mapping and analyses of the current and future (2020-2030) heating/cooling fuel deployment (fossil/renewables)," 2016.

[5] Natural Resources Canada, "Energy Efficiency Trends in Canada - 1990 to 2013," Ottawa, ON, 2016.

[6] G. Santori and C. Di Santis, "Optimal fluids for adsorptive cooling and heating," *Sustain. Mater. Technol.*, vol. 12, no. April, pp. 52–61, 2017.

[7] Y. Aristov, "Concept of adsorbent optimal for adsorptive cooling/heating," *Appl. Therm. Eng.*, vol. 72, no. 2, pp. 166–175, 2014.

[8] S. K. Henninger, S.-J. Ernst, L. Gordeeva, P. Bendix, D. Fröhlich, A. D. Grekova, L. Bonaccorsi, Y. Aristov, J. Jaenchen, "New materials for adsorption heat transformation and storage," *Renew. Energy*, vol. 110, pp. 59–68, 2017.

[9] G. Storch, G. Reichenauer, F. Scheffler, and A. Hauer, "Hydrothermal stability of pelletized zeolite 13X for energy storage applications," *Adsorption*, vol. 14, no. 2–3, pp. 275–281, 2008.

[10] N. C. Srivastava and I. W. Eames, "A review of adsorbents and adsorbates in solid-vapour adsorption heat pump systems," *Appl. Therm. Eng.*, vol. 18, no. 9–10, pp. 707–714, 1998.

[11] S. Sircar, "Basic research needs for design of adsorptive gas separation processes," *Ind. Eng. Chem. Res.*, vol. 45, no. 16, pp. 5435–5448, 2006.

[12] D. A. Bardy, C. A. Cruickshank, F. H. Tezel, Y. H. Carrier, and B. Wong, "An experimental investigation of fixed and fluidized beds as adsorbers in compact thermal energy storage systems," *J. Energy Storage*, vol. 31, no. June, p. 101648, 2020.

[13] B. Buczek, E. Klimowska, and E. Vogt, "Preparation of active carbons for adsorption cooling system," *Adsorption*, vol. 11, no. 1 SUPPL., pp. 769–773, 2005.

[14] F. Miksik and T. Miyazaki, "Material selection and properties for adsorption heat storage: perspectivity of TMPS series mesoporous silica nano-materials," *Adsorption*, vol. 25, no. 6, pp. 1137–1145, 2019.

[15] Y. Hua, A. Godin, and F. H. Tezel, "Water Vapor Adsorption in Silica Gel For Thermal Energy Storage Application," *Adv. Mater. Lett.*, vol. 10, no. 2, pp. 124–127, Feb. 2019.

[16] D. Dicaire and F. H. Tezel, "Regeneration and efficiency characterization of hybrid adsorbent for thermal energy storage of excess and solar heat," *Renew. Energy*, vol. 36, no. 3, pp. 986–992, 2011.

[17] Y. Hua, B. Ugur, and F. Handan Tezel, "Adsorbent screening for thermal energy storage application," *Sol. Energy Mater. Sol. Cells*, vol. 196, no. December 2018, pp. 119–123, 2019.

[18] D. Lefebvre, P. Amyot, B. Ugur, and F. H. Tezel, “Adsorption Prediction and Modeling of Thermal Energy Storage Systems: A Parametric Study,” *Ind. Eng. Chem. Res.*, vol. 55, no. 16, pp. 4760–4772, Apr. 2016.

[19] P. Tatsidjodoung, N. Le Pierrès, and L. Luo, “A review of potential materials for thermal energy storage in building applications,” *Renew. Sustain. Energy Rev.*, vol. 18, pp. 327–349, 2013.

[20] Y. I. Aristov, “Challenging offers of material science for adsorption heat transformation: A review,” *Appl. Therm. Eng.*, vol. 50, no. 2, pp. 1610–1618, 2013.

[21] J. Jänchen and H. Stach, “Adsorption properties of porous materials for solar thermal energy storage and heat pump applications,” *Energy Procedia*, vol. 30, pp. 289–293, 2012.

[22] D. Dicaire and F. H. Tezel, “Use of adsorbents for thermal energy storage of solar or excess heat: improvement of energy density,” *Int. J. Energy Res.*, vol. 37, no. 9, pp. 1059–1068, Jul. 2013.

[23] D. Lefebvre and F. H. Tezel, “A review of energy storage technologies with a focus on adsorption thermal energy storage processes for heating applications,” *Renew. Sustain. Energy Rev.*, vol. 67, pp. 116–125, 2017.

[24] L. Calabrese, L. Bonaccorsi, P. Bruzzaniti, E. Proverbio, and A. Freni, “SAPO-34 based zeolite coatings for adsorption heat pumps,” *Energy*, vol. 187, p. 115981, 2019.

[25] L. Calabrese, L. Bonaccorsi, P. Bruzzaniti, A. Frazzica, A. Freni, and E. Proverbio, “Adsorption performance and thermodynamic analysis of SAPO-34 silicone composite foams for adsorption heat pump applications,” *Mater. Renew. Sustain. Energy*, vol. 7, no. 4, pp. 1–13, 2018.

[26] J. Ammann, B. Michel, and P. W. Ruch, “Characterization of transport limitations in SAPO-34 adsorbent coatings for adsorption heat pumps,” *Int. J. Heat Mass Transf.*, vol. 129, pp. 18–27, 2019.

[27] X. Zheng, R. Z. Wang, T. S. Ge, and L. M. Hu, “Performance study of SAPO-34 and FAPO-34 desiccants for desiccant coated heat exchanger systems,” *Energy*, vol. 93, pp. 88–94, 2015.

[28] H. van Heyden, G. Munz, L. Schnabel, F. Schmidt, S. Mintova, and T. Bein, “Kinetics of water adsorption in microporous aluminophosphate layers for regenerative heat exchangers,” *Appl. Therm. Eng.*, vol. 29, no. 8–9, pp. 1514–1522, 2009.

[29] A. Freni, L. Bonaccorsi, L. Calabrese, A. Caprì, A. Frazzica, and A. Sapienza, “SAPO-34 coated adsorbent heat exchanger for adsorption chillers,” *Appl. Therm. Eng.*, vol. 82, pp. 1–7, 2015.

[30] S. H. Jhung, J. S. Chang, J. S. Hwang, and S. E. Park, “Selective formation of SAPO-5 and SAPO-34 molecular sieves with microwave irradiation and hydrothermal heating,” *Microporous Mesoporous Mater.*, vol. 64, no. 1–3, pp. 33–39, 2003.